REPORT DOCUMENTATION PAGE

1. AGENCY USE ONLY (Leave Blank)	2. REPORT DATE 11/15/2005	3. REPORT TYPE AND DATES COVERED Final Report, 01 Sep 00 - 31 July 05

4. TITLE AND SUBTITLE
Designed Materials for Enhanced Oxygen Reduction Electrocatalysis in PEM Fuel Cells: Novel Materials and Next Generation Synchrotron based In situ Spectroscopy.

5. FUNDING NUMBERS

6. AUTHOR(S)

Sanjeev Mukerjee (P.I), Richard, C. Urian and V. S. Murthi

DAAD19-00-1-0516

7. PERFORMING ORGANIZATION NAME(S) AND ADDRESS(ES)

Northeastern University, Department of Chemistry and Chemical Biology
360 Huntington Avenue, Boston, MA 02115

8. PERFORMING ORGANIZATION REPORT NUMBER

Final

9. SPONSORING / MONITORING AGENCY NAME(S) AND ADDRESS(ES)

U. S. Army Research Office
P.O. Box 12211
Research Triangle Park, NC 27709-2211

10. SPONSORING / MONITORING AGENCY REPORT NUMBER

41553.1-CH

11. SUPPLEMENTARY NOTES

12 a. DISTRIBUTION / AVAILABILITY STATEMENT

12 b. DISTRIBUTION CODE

13. ABSTRACT (Maximum 200 words)

A systematic RRDE investigation has been conducted in Trifluoromethane Sulfonic Acid (TFMSA) as a function of concentration (in the range 1 to 6 M) which corresponds to a change in mole ratio of water: acid from 50:1 in 1M to 4:1 in 6M TFMSA. This change in relative amount of water in the various concentrations can also be indirectly correlated to the relative humidity in an operating PEM fuel cell. The scope of this effort was to (a) confirm the shift and lowering of water activation on supported Pt alloy electrocatalysts relative to Pt at lower concentrations (1M), (b) compare the inherent activity for ORR on supported Pt and Pt alloy nanoparticles without the effect of oxide formation via activation of water, this was enabled at higher concentrations of TFMSA (6 M), (c) Relate the activation energy values at 1 M for Pt and Pt alloy electrocatalysts for further insight into the nature of the rate determining step in the mechanism. Our results confirm that for fully hydrated systems akin to 1 M concentration the alloys shift the formation and extent of water activation on the Pt alloy surfaces; this has been correlated with in-situ XAS data (changes to Pt electronic states and short range atomic order) as well as via direct EXAFS probe of formation of oxygenated species above 0.75 V (typical potential for initiation of surface oxides on Pt). The lowering of oxide formation agrees well with the extent of enhancement of ORR activity. Activation energy determinations at 1 M concentration however revealed no difference between Pt and Pt alloys indicating thereby that the rate limiting step remains unchanged. At lower water activity (6 M) with negligible water activation (and hence surface oxides), Pt surface was found to possess a higher activity for ORR as compared to the alloys.

Final Report

Reporting Duration: September 1st 2000 to July 31st, 2005

Title:
Designed Materials for Enhanced Oxygen Reduction Electrocatalysis in PEM Fuel Cells:
Novel Materials and Next Generation Synchrotron based In situ Spectroscopy

Contract/Grant Number: DAAD 19-00-1-0516

Authors:
S. Mukerjee, R. C. Urian and V. Srinivasamurthi

Performing Organization Name and Address;
Department of Chemistry, 1 Hurtig Hall, Northeastern University
360 Huntington Avenue, Boston, MA 02115

Abstract
A systematic RRDE investigation has been conducted in Trifluoromethane Sulfonic Acid (TFMSA) as a function of concentration (in the range 1 to 6 M) which corresponds to a change in mole ratio of water: acid from 50:1 in 1M to 4:1 in 6M TFMSA. This change in relative amount of water in the various concentrations can also be indirectly correlated to the relative humidity in an operating PEM fuel cell. The scope of this effort was to (a) confirm the shift and lowering of water activation on supported Pt alloy electrocatalysts relative to Pt at lower concentrations (1M), (b) compare the inherent activity for ORR on supported Pt and Pt alloy nanoparticles without the effect of oxide formation via activation of water, this was enabled at higher concentrations of TFMSA (6 M), (c) Relate the activation energy values at 1 M for Pt and Pt alloy electrocatalysts for further insight into the nature of the rate determining step in the mechanism. Our results confirm that for fully hydrated systems akin to 1 M concentration the alloys shift the formation and extent of water activation on the Pt alloy surfaces; this has been correlated with in-situ XAS data (changes to Pt electronic states and short range atomic order) as well as via direct EXAFS probe of formation of oxygenated species above 0.75 V (typical potential for initiation of surface oxides on Pt). The lowering of oxide formation agrees well with the extent of enhancement of ORR activity. Activation energy determinations at 1 M concentration however revealed no difference between Pt and Pt alloys indicating thereby that the rate limiting step remains unchanged. At lower water activity (6 M) with negligible water activation (and hence surface oxides), Pt surface was found to possess a higher activity for ORR as compared to the alloys.

(a) List of Publications:

Papers in Peer Reviewed Journals:

1. 'Oxygen Permeation Studies on Alternative Proton Exchange Membranes Designed for Elevated Temperature Operation', L. Zhang, C. Ma and S. Mukerjee*, Electrochimica Acta., 48, 1845 (2003).

2. 'Oxygen Reduction Kinetics in Low and Medium Temperature Acid Environment: Correlation of Water Activation and Surface Properties in

Supported Pt and Pt Alloy Electrocatalysts' V. Srininvasamurthi, R. C. Urian and **S. Mukerjee**, *J. Phys. Chem. B.*, **108**, 11011 (2004).

3. 'Oxygen Reduction and Transport Characteristics at a Platinum and Alternative Proton Conducting Membrane Interface' L. Zhang, C. Ma and **S. Mukerjee**, *J. Electroanalytical Chemistry* **58**, 273 (2004).

4. 'Potential Shift for OH (ads) Formation on the Pt Skin on Pt₃CO(111) Electrodes in Acid: Theory and Experiment', J. Roques, A. Anderson, V. S. Murthi and S. Mukerjee,. *Electrochemical Soc.*, **152**, E193 (2005)

5. 'Activation Energies for Oxygen Reduction on Platinum Alloys: Theory and Experiment', A. B. Anderson, J. Roques, S. Mukerjee, A. S. Murthi, N. M. MArkovic and V. Stemenkovic, *J. Phys.Chem. B,* **109**, 1198 (2005)

6. 'Effect of Copolymer Composition on the Oxygen Transport Properties of Sulfonated Poly (arylene ether sulfone) Sulfonated (sulfide sulfone) Proton Exchange Membranes' L. Zhang and S. Mukerjee, *J. Electrochem. Soc.,* **152**, A 1208 (2005)

Papers in Proceedings Volume:

1. 'ORR Kinetics of Pt based Alloys using RDE and a Correlation with their Fuel Cell Performance' V. S. Murthi, R. C. Urian and **S. Mukerjee**, Proceedings-Electrochemical Society (2005), Volume date (2002), 2002-31 (Proton Conducting Membrane Fuel Cells III), 99-110.

2. 'Effect of Water Content on Oxygen Reduction Reaction (ORR) Kinetics on Supported Pt Catalyst: A Rotating Disk Electrode Study' R. C. Urian, V. S. Murthi, and **S. Mukerjee**, Proceedings-Electrochemical Society (2005), Volume date (2002), 2002-31 (Proton Conducting Membrane Fuel Cells III), 54-66

3 'Oxygen Reduction and Transport Characteristics at a Platinum/Sulfinated Poly-ether Sulfone Membrane Interface', L. Zhang, C. Ma and **S. Mukerjee**, Proceedings-Electrochemical Society (2005), Volume date (2002), 2002-31 (Proton Conducting Membrane Fuel Cells III), 111-126

Book chapters:

1. 'Oxygen Reduction and Structure Related Parameters for Supported Catalysts', S. **Mukerjee** and S, Srinivasan, *Handbook of Fuel Cells: Fundamentals, Technology and Applications, Vol. 2: Electrocatalysis*, Edited by W. Vielstich, H. A. Gasteiger and A. Lamm, John Wiley and Sons (2003).

2. 'In situ X-Ray Absorption Spectroscopy of Carbon Supported Pt and Pt Alloy Electrocatalysts: Correlation of Electrocatalytic Activity with Particle Size and Alloying', **S. Mukerjee**, *Advanced Nanoparticles for Fuel Cells and*

Electrocatalysis, Edited by A. Weickowski, E. Savinova, and C. G. Vayenas, Marcel Dekker, (2003).

Invited Talks (2003)

1) 'Improving Fuel Cell Efficiencies-An Electrocatalytic Challenge' S. **Mukerjee.** *Colloquium Talk*, Department of Chemical Engineering, Goddard Hall, Worcester Polytechnic, Worcester, MA, November 30th, 2000.

2) 'Fundamentals of Charge Transfer Dynamics at Two and Three Dimensional Electrochemical Interfaces', S. **Mukerjee.** *Seminar Speaker*, Department of Chemistry, Princeton University, April 9th, 2001.

3) 'Electrocatalysis of Oxygen Reduction in a Fully Hydrated Proton Exchange Membrane Interface: Problems and Prospects', S. **Mukerjee.** *Keynote speaker* at International Fuel Cells, May 15th, 2001.

4) 'Proton Exchange Membrane Fuel Cells: from Research to Reality', Colloquium speaker, S. **Mukerjee.** Department of Chemistry, Virginia Technical and State University (Virginia Tech.), 24th, July, 2001.

5) 'Electrocatalysis of PEM Fuel Cell Reactions: New Materials and Next Generation In situ Spectroscopy' *Colloquium Speaker at Stonehill College, Easton, Massachusetts.* February 20th, 2002.

6) 'Electrocatalysis of PEM based Fuel Cell Reactions: New Materials and Next Generation In situ Spectroscopy, S. **Mukerjee.** Colloquium Speaker, University of New Hampshire, Durham, NH, April, 18th, 2002.

7) 'Electrocatalysis of PEM Electrode Processes, Problems and Prospects. S. **Mukerjee.** Invited speaker at the Departmental Seminar, MIME Department, Northeastern University, May 3rd, 2002.

8) 'Electrocatalysis of Fuel Cell Reactions: Are We Stuck with Pt?' S. **Mukerjee.** *Invited Speaker at the Workshop on Biofuel Cells*, Sponsored by the Department of Chemical and Nuclear Engineering, University of New Mexico (UNM), U.S. Army Research Office (ARO), Defense Advanced Research Projects Agency (DARPA) and UNM/NSF Center for Micro-engineering Materials, Washington D.C., June 30-July 2nd, 2002.

9) 'Charge Transfer Dynamics at Two and Three Dimensional Interfaces: An In situ Spectro-electrochemical Perspective using Synchrotron X-rays'. S. **Mukerjee** (Invited Speaker), Gordon Conference on Electrochemistry, Ventura Beach, Ventura, CA; January 12-16, 2003.

10) 'Improving Charge Transfer at Electrochemical Interfaces: An Electrochemist's Perspective on the Shape of a more Portable World'? S. **Mukerjee,** *Colloquium Talk* at Northeastern University, Department of Chemistry. April 24th, 2003.

11) 'Reducing Overpotential Losses for Oxygen Reduction Reaction with Pt based Alloys: A RRDE and In situ Synchrotron XAS Investigation' S. Mukerjee, *invited speaker at the Workshop on Theory and Surface Measurement of Fuel Cell Catalysts*, Magleas Conference Center, Hosterkob, Denmark. June 16-18, 2003.

12) 'Electrocatalysis of PEM Fuel Cell Reactions: Problems and Prospects for the Future' S. Mukerjee, *Colloquium Speaker*, at the Department of Chemical and Nuclear Engineering, University of New Mexico, Albuquerque, New Mexico, September 23rd, 2003

13) 'Recent Advances in Electrocatalysis of PEM Fuel Cell Reactions: A Paradigm Shift from Current State of the Art', S. Mukerjee, *Colloquium Speaker at the Department of Chemistry, Queens University, Ontario, Canada.* October 24th, 2003.

14. 'Recent Advances in Materials for Electrochemical Energy Storage and Conversion' S. Mukerjee, *Pre-workshop tutorial, Nanostructured Materials 2003, Miami Beach, FL, November 9-10, 2003*

15) 'Recent Advances in Materials for PEM Fuel Cells', S. Mukerjee, *Colloquia speaker at the Department of Chemistry, Indian Institute of Technology, Kanpur, India, November 17th, 2003*

16) 'Hydrogen Energy: Dream or Reality', S. Mukerjee, *Colloquia speaker at the Department of Chemistry, Indian Institute of Technology, New Delhi, India, November 26th, 2003*

17) 'Materials Science of Electrochemical Energy Conversion', S. Mukerjee, *Colloquia Speaker, Tata Energy Research Institute, New Delhi, India, November 28th, 2003.*

18) 'Improving Charge Transfer at Electrochemical Interfaces: An Electrochemist's Perspective on the Shape of a more Portable World?, S. Mukerjee, *Presented at the Colloquia at the Department of Chemistry, University of Puerto Rico, Rio Piedras, San Juan, March 3rd, 2004*

19) 'Materials Development Challenges for Electrochemical Energy Conversion and Storage', S. Mukerjee, *Presentation at Tiax, July 15th 2004, Acorn Park, Boston*

20) 'Non Noble Metal Chalcogenides as Promising Candidates for Oxygen Reduction Reaction Catalysts in Fuel Cell Applications', J. M. Ziegelbauer, Y. Garsany and S. Mukerjee, *Presented in the Session on Application of Nanomaterials in High Performance Batteries and Fuel Cells, National Meeting of the Electrochemical Society, Honolulu, Hawaii, October 3-8, 2004*

21) 'Issue of Interfacial Water Activity in the Electrocatalysis of CO and Methanol Oxidation: Combination of Electrochemistry and *in situ* Synchrotron based XAS Data, V. S. Murthi, S. Mukerjee, *Presented at the Fourth International Symposium on Polymer Electrolyte Fuel Cells' National Meeting of the Electrochemical Society, Honolulu, Hawaii, October 3-8, 2004*

22) 'Determination of Specific Site Adsorption on Pt and Pt Alloy Electrocatalysts using *In situ* X-Ray Absorption Spectroscopy' M. Teliska, V. S. Murthi, S. Mukerjee, D.

Ramaker, *Presented at the Fourth International Symposium on Polymer Electrolyte Fuel Cells' National Meeting of the Electrochemical Society, Honolulu, Hawaii, October 3-8, 2004*

23) 'Interfacial Water Activity and Electrocatalysis: Combination of Electrochemistry and Synchrotron based *In situ* XAS', V. S. Murthi, K. Ramamoorthi and **S. Mukerjee**, *Presented at the Materials Research Society Meeting in Boston, November 29-Dec 3, 2004.*

24) 'Materials Development Challenges for Electrochemical Energy Conversion and Storage: Overview of Research at Northeastern University' **S. Mukerjee**, *Presented at a Colloquium in BASF Central Research, Ludwigshafen, Germany, December 17th, 2004.*

25) 'Electrocatalysis of Polymer Electrolyte Fuel Cell Reactions: Problems and Prospects for the Future', *Presented at the Second International Conference of Electrochemical Power Systems (ICEPS-2), Hyderabad, India, December 19, 2004.*

26) 'High Performance Electrodes with Very Low Pt Loading Prepared by Dual Ion Beam Deposition in PEM Fuel Cells', M. S. Saha, **S. Mukerjee**, A. F. Gulla and R. J. Allen, Presentation in the Symposium on Fuel Cells from Materials to Systems, Annual Meeting of the Electrochemical Society, Quebec City, Quebec, Canada, May 15-21, 2005.

27) 'X-ray Absorption Spectroscopy Investigations of Transition Metal Based Chalcogenide Electrocatalysts for Oxygen Reduction Reaction Applications', Y. Garsany, J. Ziegelbauer, S. Mukerjee, A. Gulla, and R. Allen, Presentation in the Symposium on Fuel Cells from Materials to Systems, Annual Meeting of the Electrochemical Society, Quebec City, Quebec, Canada, May 15-21, 2005.

(b) Scientific Personnel:
Vivek Srinivasamurthi: Graduate Student
Richard C. Urian: Graduate Student

(c) Report of Inventions:
Provisional Patent Filed: Novel Three Dimensional Polymer Composite Reaction Layers for Improved Electrochemical Interface. Full Application filed on August 2005.

(d) Scientific Progress and Accomplishments:
(See attached Report)

(e) Technology Transfer:
Our research effort is in full and active collaboration with United Technology - Fuel Cells with Dr. Jeremy Meyers as the lead investigator from UTC-fuel cells. Other team members in this effort are Dr. John Bett and Y.Ping.

f) Thesis:

(1) Richard C. Urian (Joined September 1999, Graduated June 2003)

Thesis Title: *Platinum & Platinum Alloys for Proton Exchange Membrane Fuel Cells: a Look at Adsorbate Interactions at the Catalyst Surface'*

2) Vivek Srinivasamurthi (September 1999, Graduated January 2005)
   Thesis topic: *'Electrocatalysis at PEM Interface: Effect of Elevated Temperatures and Lower Relative Humidity'*

Final Report

Designed Materials for Enhanced Oxygen Reduction Electrocatalysis in PEM Fuel Cells: Novel Materials and Next Generation Synchrotron based In situ Spectroscopy

Table of Contents

I.   Introduction:

I.1.   *Electrocatalysis of Oxygen Reduction Reaction: Statement of the Problem and Overall Objectives of this Effort.*

The principle causes of the poor kinetics of the four-electron oxygen reduction reaction can be attributed mainly to the low exchange current density of the oxygen reduction reaction[1, 2]. The high cathodic overpotential loss of ~ 220 mV, even at open circuit potentials with the current state of the art low Pt loading electrocatalysts is attributed to a mixed potential that is set up at the oxygen electrode. The mixed potential is due to a combination of slow O_2-reduction kinetics and competing anodic process such as Pt-oxide formation and/or impurity oxidation[3]. Further, the low exchange current density of the O_2-reduction reaction results in a semi-exponential Tafel like behavior, indicating that the reaction is activation controlled over three orders of magnitude in current density. It has been determined that the exchange current density of O_2-reduction is 5-6 orders of magnitude lower than that of H_2-reduction reaction.[3][4]

Since the activation overpotential stretches over three orders of magnitude in current density the problem of significant improvement in O_2-reduction activity is primarily electrocatalytic. The current state of the art performance reflects a wealth of previous efforts at improving the electrocatalyst utilization at the electrode-electrolyte interface, making low Pt loading of ~ 0.15 mg/cm^2 a reality. Further breakthrough in performance therefore requires changing to an alternative electrocatalyst system. A review of the solid state electrochemistry of materials available for interface with proton exchange membrane fuel cells clearly shows that the Pt based alloy electrocatalysts offer the best prospect for achieving the highest possible performance levels with long term stability. Alternative choice of electrocatalysts such as organic macrocycles (porphyrins and phthalocyanines for *e.g.*) despite their promise of a more facile four electron transfer are plagued by serious concerns of poor long-term stability. More recently, the Chevrel type complexes with the general composition $Mo_{6-x}M_xX_8$ (X = Se, Te, SeO, S; and M= Os Re and Rh *etc.*) have shown promise as an alternative ORR electrocatalyst, with an added benefit of lack of susceptibility to methanol oxidation. Its stability characteristics in the current state of the art compositions however have similar problems of activity loss.[5]

Significant improvement of ORR electrocatalysis on Pt based alloy systems therefore requires a two fold effort. Firstly, inhibiting the formation of adsorbed oxygenated species (primarily Pt-OH) beyond 0.8 V, a known surface poison and secondly, change the electronic and short range atomic order around Pt to induce alternative lower energy pathways for improved ORR kinetics.

A review of literature on the current state of the art points towards four important trends that help guide the strategy to meet the challenge for higher ORR activities: (*i*) Pt based alloy nano-clusters offer the best prospects for achieving the highest activities with the desired long term stability. (*ii*) Achieving higher ORR activities will require modifications in the Pt electronic and short-range atomic order, which is achievable either by alloying or by changing the electrocatalyst support matrix or both. (*iii*) Recognizing the correlation of the electrocatalytic activity and the characteristics unique to nano-clusters, these include particle size distribution, surface morphology and segregation etc. (*iv*) Need for new membrane-electrode assemblies containing polymer composite reaction layer design incorporating the nano-clusters in a matrix containing both electronic and ion conducting pathways. It is upon these trends, and our view that the optimum design has not yet been achieved in the present day PEMFC systems, that the present proposal is grounded.

The overall goals and objectives of this proposed research effort are listed below in terms of the overall statement of work.

Task 1.   Development of binary and ternary Pt alloy metal clusters encapsulated in various proton conducting ionomers using micelle synthesis techniques for enhanced electrocatalysis of cathodic oxygen reduction. This will involve judicious choice of alloying elements to form alloy clusters possessing 50 to 100 mV lower overpotential for ORR.

Task 2.   Development of a polymer composite reaction layer *sans* carbon containing both ionic and electronic conduction pathway. The objective is to (a) increase the three dimensional charge transfer efficiency by orders of magnitude and (b) provide for a more universal interface between electrocatalyst and membrane.

Task.3.   To establish clear structure-property relationships by using *in situ* synchrotron based x-ray absorption (XAS) and far infrared (FIR) technique under actual fuel cell operating conditions. These techniques offer the unique ability to study the metal cluster substrate from the perspective of changes to its electronic and short-range atomic order (using XAS) as well as the metal cluster-adsorbate and polymer-metal interactions (using FIR). This part of the objective is going to be conducted at Brookhaven National Laboratory by Northeastern University team using beam time obtained through prior successful general user proposals.

Task 4.   Electrochemical Characterization, both dynamic and steady state half and single cell polarization conducted on a wide variety of membrane electrode assemblies incorporating concepts described in tasks 1-2 using state of the art fuel cell test facility with 5cm^2 and 50 cm^2 single cells.

I.2   Summary of the First, Second, Third and Fourth Interim Report (Reporting period, September 1st, 2000 to January 31st, 2003.

I.2.1   Summary of Achievements Reported in the First Interim Report.

This interim report examined the progress in the first five months of the three year effort aimed at enhancing electrocatalytic activity for oxygen reduction reaction (ORR) in low to medium temperature PEM based fuel cells. Since the unique environment of PEM affords stability of Pt based electrocatalysts, our effort focused on trying to modify Pt electronic and short range atomic order so as to effect higher ORR activity. In this report we showed the following progress: (A) Fabrication of a four channel PEM fuel cell test stand for steady state polarization measurements, (B) Preparation of three electrocatalysts, namely Pt/C, PtNi/C and PtCo/C using an exclusive colloidal sol technique developed in-house. (C) A combination of XRD, TEM and EXAFS measurements show excellent crystallinity, narrow particle size range (30-40Å) and predominant phase of Pt$_3$M for the alloy electrocatalyst. (D) Steady state polarization for ORR shows up to eight-fold activity enhancement for PtCo/C compared to the Pt/C control. (E) Cyclic voltammograms show clear evidence of shifts in the onset of Pt-OH formation in the alloys relative to Pt/C.

Future efforts are planned for (I) preparation of electrocatalyst by micellar routes, (b) in situ XAS measurements to determine the existence of skin effect and shift in the onset of Pt-OH formation in the alloys and (c) Performance of the first set of experiments using in situ Far IR spectroscopy.

1.2.2   Summary of Achievements in the 'Second Interim Report.

1.   Alloying of Pt with first row transition elements to form binary or ternary alloy results in a clear enhancement of oxygen reduction activity. This enhancement is manifested in better Tafel kinetic parameters such as exchange current density or current density

at 900 mV. In addition, there is lowering of ORR overpotential by approximately 45 mV's.

2. These enhancements can be related to a lowering of oxide coverage on the Pt alloy surface thus changing the per-exponential factor in the Arrhenius activation analogy for oxygen reduction, though the reaction order with respect to molecular oxygen remains unchanged, which shows that the initial adsorption geometry of the molecular oxygen remains the same on the Pt alloys as compared to Pt/C. This therefore indicates that the enhanced kinetics were related to the change in the electronic and/or short range atomic order of Pt brought about as a result of alloying.

3. Cyclic voltammetry as well as analysis of the XANES and EXAFS spectra taken in sealed electrochemical cells as a function of potential shows evidence of a shift in the onset potential of water activation reaction. This electrochemical and direct spectrochemical evidence is of great significance, since a positive shift in the onset of Pt-OH formation could account for the lowering of the overpotential losses observed for Pt alloys for ORR.

4. The stability of these alloys has been examined in terms of the corrosion characteristics of the more oxidizable alloying element. This was performed using XANES analysis at the alloying element K edge under in situ electrochemical control, with the electrode polarized at high positive potentials close to the open circuit (0.9 v vs. RHE). These studies carried out at room temperature with sealed spectro-electrochemical cells have shown that alloying elements such as Co are remarkably stable even after being subjected to nine hours of polarization at 0.9 V vs. RHE.

5. These measurements support our hypothesis, which considers the outer surface of these metal alloy nanoclusters to be entirely Pt with the inner core comprising of the alloy. Future efforts are on to definitely prove this Pt skin effect to be true.

6. In the last reporting period we made significant progress in getting our far infrared set up established at the National Synchrotron Light Source in Brookhaven National Laboratory. We are just starting in situ FIR measurements, which are scheduled for later this quarter (Spring 2003).

7. Our current efforts are focused on new ways of preparing Pt alloy nanoclusters and encapsulating them in ion conducting monomer surfactants. This is with a view of perturbing the Pt surface properties while ensuring efficient charge transfer.

1.2.3   Summary of Achievements in the third Interim Report:

1. Preparation of ternary alloys such as PtCoCr which show levels of enhancement similar to PtCo/C. These conclusions are based on RDE results in 1M TFMSA, which allows for comparison of the inherent ORR electrocatalytic activity. Steady state single cell data from PEM fuel cells at 85°C, showed comparable performance with the current bench mark Pt alloy (PtCo/C).

2. The first set of electrocatalysts (Pt and PtCo/C) prepared using micellar methods are reported. This methodology allows for very strict control of the electrocatalyst alloy composition and the nano-particle alloy composition. It also enables the encapsulation of these alloys with select ionomeric surfactants, which has consequences in the control of surface properties. The Pt and PtCo/C prepared by micellar methods clearly showed enhanced activity for ORR in comparison to those prepared by conventional solloidal sol methods followed by carbothermic reduction and alloying.

2. A rotating disk setup was enabled to measure the inherent activity for ORR. For this a protocol was established which allowed for these measurements to be conducted on supported electrocatalysts in TFMSA electrolyte. The advantage of TFMSA

electrolyte was the ability to control the water at the electrocatalyst-electrolyte interface by changing the concentration of TFMSA. This will enable the measurement of true ORR activities as a function of activity of water. Results of these studies will be reported in the final report.

1.2.4 Summary of Achievements in the Fourth Interim Report:

From the results discussed above it is evident that the oxygen reduction reaction on an electrocatalyst surface depends on the nature of Pt surface (alloyed or unalloyed) as determined by the surface electronic properties which affects water activation in a fully hydrated state. The consequence of alloying Pt with transition metals such as Co and Fe is a significant lowering of water activation beyond 0.8 V vs. RHE, in contrast to Pt/C. The lower affinity towards water activation in fully hydrated environment (1 M TFMSA) for Pt alloys in contrast to Pt is manifested in the observed Tafel slope which is 120 mV/decade (2RT/F) for the alloys in contrast to the expected value of 60 mV/decade, observed on both pc-Pt and Pt/C. Such a lowering of affinity towards oxygenated species on Pt alloys in 1 M $HClO_4$ is also reported using *in-situ* XAS data. XANES data combined with theoretical calculations is capable of providing direct spectroscopic evidence of OH adsorption on the electrocatalyst surface. This trend in OH inhibition (Pt < Pt-Ni<Pt-Co <Pt-Fe < Pt-Cr) can be directly correlated with the previously reported kinetic reactivities for a fuel cell with these alloys and follows a similar trend for ORR in 1M TFMSA as shown above. Both the *in-situ* XANES and EXAFS data analysis comparing Pt L_3 edge spectra at 0.84 V vs. RHE for alloys clearly indicate a lack of oxide coverage. Comparison of Pt L_3 edge EXAFS data clearly provides as an alternative to probe the surface of electrocatalysts to identify the different morphologies. A lowering of oxide formation, a surface poison for molecular oxygen adsorption on Pt alloys in the fully hydrated analog (1 M TFMSA) is also correlated to a concomitant increase in ORR activity as shown by RDE data. However, a lowering of water activity resulting from a shift in concentration to 6 M shows that while there is an increase in ORR activity for Pt/C due to lowering of surface oxide formation, a corresponding effect with Pt alloys does not occur. This further supports our earlier contention of ORR activity being dependant on surface coverage by oxides. Further, a more important conclusion from the lack of increased activity for Pt alloys in 6 M concentration of TFMSA is that the process of alloying with transition metals does not render the surface of the catalyst to be inherently more active for oxygen reduction, in contrast to the increased activity observed for the alloys in 1 M concentration. This is related to a wealth of prior literature as discussed in earlier sections where the rate limiting step for oxygen reduction reaction in a fully hydrated state (1 M concentration) is the initial dissociative adsorption of molecular oxygen. Significant changes to the electronic states of Pt as a consequence of alloying could affect the affinity for molecular oxygen adsorption. This is a strong possibility supported by our data in 6 M TMFSA; its confirmation is a subject of theoretical simulations, which are currently being pursued.

II.   Progress Report

Results and Discussion

II.1   Fundamental Studies of Water Activation on Pt and Pt Alloys: An RRDE Investigation with Different Concentrations of TFMSA

In terms of electrocatalysis, O_2-reduction on Pt crystallites occurs by a parallel mechanism with direct four-electron reduction as the dominant step.[12] However due to large number of possible steps within this ambit a detailed mechanism still defies formulation. From a mechanistic perspective there are two views regarding the first reaction step. The first view, based on an early proposition by Damjanovic et al.[13] suggested a simultaneous proton and charge transfer step involving: $O_2 \Leftrightarrow O_2$ (ads), followed by rate determining charge transfer step: O_2 (ads) $+ H^+ + e^- \rightarrow$ product(s). This mechanism was supported by results on bulk planar Pt electrodes based on pH and pressure dependencies. Langmuirian kinetics was used to explain the Tafel slope of 120 mV/decade below 0.8 V. While the 60 mV/decade Tafel slope beyond 0.8 V was explained assuming oxygen adsorption under Temkin conditions in the presence of surface Pt-OH poison. One of the key features of this mechanism is the association of the low Tafel slope of 60 mV/decade to the surface Pt-OH, a surface poison to the O_2 adsorption. A second view, proposed by Yeager and co-workers,[14-16] suggests that the most likely mechanism of the four-electron oxygen reduction on Pt involves dissociative chemisorption of O_2 molecule on a Pt surface. This probably occurs with simultaneous charge transfer. Based on the experimental evidence in support of this proposition two routes were suggested,[14,15,17] the primary difference between them being that route I involves a single Pt atom whereas in route II adjacent sites on two different Pt atoms are involved. In this context it is important to point out that three different models for adsorbed oxygen on metal sites have been proposed. (a) A molecular edge wise adsorption without rupture of the O=O bond (Griffiths model). Here the bond is formed mainly between π-orbital of O_2 and empty d_z^2 orbital on the metal surface with a π-backbonding to form partially filled d_{xy} and d_{yz} orbital of the metal and a π^* anti-bonding orbital of O_2. (b) End on adsorption through a single bond (Pauling model), in a σ-type bond in which σ orbitals of O_2 donate electron density to an acceptor d_z^2 orbital on the metal. (c) A bridge model, here we have two bonds with two sites as proposed by Yeager.[18]

Previous reports have shown that the formation of Pt-OH beyond 0.8 V is derived not from the interaction of O_2 with Pt, but rather from reaction of H_2O with Pt causing inhibition of the O_2-reduction[19-21] resulting in a low Tafel slope of 60mV/dec. In electrolytes containing phosphate or bisulfate anions a low Tafel slope was not observed on a Pt (111) due to the surface poisoning of these anions which shift the Pt-OH formation to a more positive potential[20,22]. However, for the other low index planes Pt (100) and Pt (110) a change of slope was observed since the anion adsorption on these planes are minimal.[23] Significant improvement of ORR electrocatalysis could therefore be afforded by, firstly inhibiting the formation of adsorbed oxygenated species (primarily Pt-OH) beyond 0.8 V, a known surface poison and, secondly, changing the electronic and short range atomic order around Pt to induce alternative lower energy pathways for improved ORR kinetics.

Many Pt based transition metal alloys have been suggested for use as a cathode catalyst,[1,24,25] they have shown varying degrees of enhancement as compared to Pt in a completely hydrated PEM fuel cell. Changes in short range atomic order, particle size, Pt d-band vacancy, Pt skin effects and Pt-OH inhibition have been advanced as some of the reasons

attributed for the enhanced performance by these alloys.[26-29] For further details see reviews by Adzic[12] and Mukerjee[30].

Inhibiting or shifting the onset potential (approximately 800 mV vs. RHE for Pt) of Pt-OH formation, providing free sites for molecular oxygen adsorption, is generally expected to lower the overpotential losses. A number of prior reports have provided indirect evidence to the possibility of inhibiting the formation of anodic activation of water for Pt-OH formation.[2,3,31,32] Shifting the onset potential of OH formation on Pt is dependent on the ability of the alloying elements to (a) modify the Pt electronic and short range atomic order for inhibiting activation of H_2O and (b) ability of the alloying element to attract and hold H_2O_{ads} more strongly than the surrounding surface Pt atoms.

The effect of different electrolytes for ORR has been extensively investigated.[16,17] As a part of these investigations, trifluoromethane sulfonic acid (TFMSA) was studied initially as an effort to identify an alternate electrolyte medium for a phosphoric acid fuel cell (PAFC). This was motivated by problems of strong phosphate anion adsorption on Pt,[33] as well as poor proton conductivity and oxygen solubility, typically encountered in concentrated phosphoric acid. Trifluoromethane sulfonic acid (TFMSA) and other analogous sulfonic acids significantly alleviated all these aforementioned problems thereby enabling increased ORR activity. Notable among these prior investigations are those by Enayetullah and co workers[34] who have studied oxygen reduction (ORR) electrocatalysis on a polycrystalline (pc) Pt microelectrode in various concentrations of TFMSA . Significant enhancement of ORR activity was reported as a consequence of the use of TFMSA rather than another acid. In this investigation, higher Tafel slope ~ 2RT/F or 120mV/decade was reported in high concentrations of TFMSA (greater than 6 M) which was attributed to the lower activity of water. They concluded that the high ORR activity in concentrated TFMSA was a consequence of an oxide free Pt surface under conditions of low water activity. Similar results were also shown with Trifluoroacetic acid with potassium salt of trifluoroacetate as electrolyte with varying mole ratio of water.[31]

The parallel pathway for the ORR leading to simultaneous formation of peroxide (two electron reduction) at the electrocatalyst interface has been reported previously.[35-37] Prior results by Arvia et.al.,[35,36] in 0.1 M and 1 M TFMSA on faceted Pt single crystals showed dependence on crystal structure for both four electron oxygen reduction as well as two electron peroxide formation. This prior report, based on a rotating ring-disk method, showed that higher amounts of peroxide were formed on a Pt (100) as compared to Pt (111) and polycrystalline Pt. Prior reports[38-40] have shown increasing peroxide yield at higher overpotentials. A Tafel slope of 165mV/decade on the (100) crystal plane of Pt in the high overpotential region was explained on the basis of a stronger peroxide adsorption. Recent results by Ross and co-workers,[37] have compared peroxide formation of supported Pt alloys relative to Pt/C in 0.1 M $HClO_4$ using a thin film RRDE method. Comparison of Pt-Co/C, Pt-Ni/C (25 a/o) with Pt/C, showed no differences in the peroxide yield.[37] A 50 atomic percent Pt-Ni/C however showed a higher peroxide yield as compared to Pt-Co (same alloying ratio) and Pt/C,[37] thereby offering a tentative possibility of perturbing the parallel pathway for ORR.

One of the main obstacles to getting an insight into the reaction pathway for oxygen reduction is that a lot of variables remain undetermined. Even with the vast knowledge of measured parameters, some rate constants cannot be determined with ring–disk measurements. Inhibition of O_2 reduction at under potential deposited (UPD) silver adatoms on Pt was used by Adzic and co-workers to show that the adsorption of O_2 on Pt occurred through a bridge configuration.[41] A more general scheme proposed by Anastasijevic et al.[42] from the analysis of data from ring–disk experiments included most of the possible intermediates and were able to explain both the "series" and "parallel" pathways for ORR.

Investigation of peroxide formation at the electrocatalyst-ionomer interface in a PEM fuel cell context is especially important from the perspective of attempts to develop alternative

proton conducting polymer membranes capable of elevated temperature operation (120 to 140°C). The current state of the art perfluorinated systems, such as Nafion®, are restricted to operating temperatures below 100°C. Elevated temperature operation offers better ability to tolerate CO from the reformer feed and better thermal and water management enabling easier system integration. However most of these alternative polymer membranes possess non fluorinated back-bones and pendant chains which are susceptible to attack by free radicals. Among the possible mechanisms postulated are: (a) Oxygen diffusing through the membrane to the anode and forming HOO• radicals at the surface of the catalyst leading to an attack of the tertiary H at the α carbon of the polymer.[43] (b) Oxygen reduction at the cathode proceeding through a peroxide intermediate H_2O_2, either reacting directly or via trace metal ions in the membrane to form HOO• and HO• radicals, causing membrane degradation during the cathode reaction.[43] Hence the determination of the peroxide yield is important from the perspective of the different electrocatalysts (Pt and Pt alloys) and water activity at the interface.

The objective of this investigation is to examine (a) the inherent activity for oxygen reduction on select Pt alloy electrocatalysts relative to Pt and (b) the peroxide yield at the electrocatalyst-ionomer interface. Both parts of this investigation are related to effect of variation of water activity at the interface, which is achieved by varying the concentration of TFMSA,[44] an electrolyte with low susceptibility for anion adsorption[45,46] and excellent transport properties for protons and dissolved oxygen.[14,15,17,18,47] By varying the activity of water at the interface, it is therefore possible to control the extent of anodic water activation and hence formation of oxide species on the electrocatalyst surface. These have been reported previously by Conway et. al.[48] and Enayetullah et. al.[49] This is used in this investigation to understand the inherent activity of select Pt alloys (PtCo/C and PtFe/C) for oxygen reduction. By curtailing the influence of surface oxides on oxygen reduction, effects of the perturbation of the electronic and short range atomic order (Pt-Pt bond distance and coordination number) of Pt as a result of alloying can be determined. Formation of peroxides at the interface is also dependent on presence of water; hence controlling the water activity at the interface is expected to provide important insight on the role of the electrocatalyst surface properties (electronic and short range character) and its relation to the extent of two electron peroxide formation.

Experimental

Electrocatalyst -
Two different carbon supported binary Pt alloys, PtFe/C and PtCo/C with a nominal composition of 3:1 (Pt:M) atomic ratio were investigated with Pt/C used as a control. All electrocatalysts were prepared in-house and had a metal loading of 20% on carbon support (Vulcan XC-72, Cabot, USA). The preparation methodology used[50-53] was the well known colloidal 'sol' and carbothermic reduction methods. Briefly, the preparation method involved initial preparation of a Pt/C sample using a sulfato-complex approach described in more detail elsewhere.[30,53,54] The incorporation of the second alloying element was accomplished by first dispersing the supported electrocatalyst in an aqueous medium and raising the pH to 8 by the addition of ammonium hydroxide. Next, the appropriate salt solution of the alloying element was added and the pH reduced to around 5, followed by drying and carbothermic reduction in an inert atmosphere at 900°C. In these methods, an oxide of the second alloying element is incorporated on the supported Pt/C electrocatalyst. When this is subjected to carbothermic reduction under inert conditions at 900°C, the crystallites undergo reduction and alloying on the carbon support, thus providing for supported alloy nanoparticles.

All electrochemical measurements were made at room temperature using a rotating ring-disk electrode setup from Pine Instruments connected to an Autolab (Ecochemie Inc.,

model-PGSTAT 30) potentiostat equipped with a bipotentiostat interface. All potentials were measured with respect to a sealed hydrogen reference electrode (RHE)[55,56] made from the same concentration of the electrolyte used in the experiment. In order to avoid potential artifacts caused as a result of different electrolyte concentrations in the reference relative to experiment, the electrolyte in the reference electrode had the same concentration as used in the experiment. Hence, any potential shift (Nernst shift) in the reference electrode due to the concentration of electrolyte is corrected for and all the CV's recorded at the working electrode are a true reflection of the effect of water activation.

Electrolyte -

Trifluoromethane sulfonic acid (CF_3SO_3H / TFMSA) was obtained from 3M Inc., and underwent a purification step as described elsewhere.[34,47,57] TFMSA was triply distilled under vacuum below 60°C and the monohydrate (9.5M) was then prepared from the purified acid. The pure monohydrate was then re-crystallized to form a white crystalline solid which was stored in a Teflon bottle for future use. The re-crystallization step was carried out two more times for further purification prior to the preparation of the 6 M and 1 M solutions used for this investigation. The solutions were first purged with N_2 and the electrode was cycled continuously until a clean reproducible Pt cyclic voltammetric profile was obtained. The solutions were then purged with O_2 for ORR measurements. Measurements were also made on a 6 mm diameter polycrystalline (pc) Pt disk (Pine Instruments) as a control experiment. The diffusion coefficient of oxygen and its solubility in these solutions were determined by a Chronoamperometric method using a Pt microelectrode as reported elsewhere.[58,59]

Electrode preparation -

Suspensions of 1 $mg_{catalyst}$ per mL in iso-propanol were obtained by ultrasonication for 30 min. 20 μL of 5wt. % Nafion® was added to the suspension prior to mixing to act as a binder. Since the amount of catalyst to Nafion® loading was very small relative to normal fuel cell electrodes (wt. ratio of Pt/C to Nafion® ::50:1, mg/cm^2) and comparable to previously reported rotating disk electrode experiments,[60,61] diffusion effects due to the Nafion® layer were neglected. A glassy carbon disk electrode (0.283 cm^2 Pine Instruments) was used as the substrate for the supported catalysts and was polished to a mirror finish using 0.05μm alumina suspension (Buehler) before loading the catalyst. A 20 μL aliquot of the suspension (corresponding to 4μg of metal) was then loaded onto the glassy carbon to give a constant metal loading of ~14μg/cm² (geometric) and was allowed to dry before introducing it into the electrolyte. The gold ring electrode was activated prior to any experiment by cycling between 0 – 1.6 V (50mV/sec) in 1M CF_3SO_3H until steady state voltammetry was reached.

After preparation, the electrodes were immersed in oxygen-free electrolyte solutions at room temperature and cycled several times between 0 and 1.2 V at 50 mV/sec and then cycled further at 10 mV/sec, the cyclic voltammograms were then recorded. For oxygen reduction studies the electrode was immersed in oxygen saturated (Med-Tech Gases Inc.) electrolyte and cycled initially between 0.2 and 1.2 V at 1000 rotations per minute. For ORR experiments the electrode was scanned between 1.2 and 0.3 V at 25mV/sec for 10 cycles at each rotation and the last 3 scans at each rotation rate were used for data analysis. The rotation rates were 400, 625, 900, 1225, and 1600 rpm, the upper limit was 1600 rpm due to viscosity issues in high concentrations of TFMSA. Kinetic measurements of the ORR in terms of the Tafel parameters and kinetic currents were made, similar to a wealth of prior published approaches for the analysis of the RDE data.[62,63] Use of the ring disk electrode in conjunction with the rotating disk experiments followed well known methodologies described elsewhere.[61,64,65] Here, the peroxide yield as a result of 2 electron reduction was determined in parallel to the overall ORR activity. Kinetic measurements were also performed at different

temperatures (30, 40, 50, and 60°C) to evaluate the activation energy for ORR based on an Arrhenius type of plot.

Physico-chemical characterization

X-ray diffraction was conducted using the high resolution X-18A beam line at the National Synchrotron Light Source (NSLS) at Brookhaven National Laboratory. Previously reported characterization of the 3:1 PtM/C composition[25] showed the existence of a fcc metallic phase with an average particle size of ca. 4 nm. Line broadening analysis of the primary XRD peak <111> was conducted using the Scherrer treatment of the data. The data was first fitted to an indexing program, which allowed accurate measurement of the line widths at half maximum. These widths were then used to obtain the particle size. Corrections for beam deviations in the instrument were considered negligible due to the high collimation of the synchrotron beam.

XANES (X-ray absorption near edge structure) data from *in-situ* X-ray absorption spectroscopy (XAS) was measured. The objective was to verify the nominal atomic ratios as well as nature of alloying, especially in the cases where the difference in the line shifts of the XRD patterns between Pt and Pt alloy electrocatalysts was very small. Further, the Pt d-band vacancy/atom was also determined from the relative areas under the Pt L_3 and L_2 edges for all the Pt and Pt alloy compositions. The methodology for analysis of the XANES spectrum followed those of Wong et.al.[66] The procedure for determining the Pt d-band vacancy concentration was initially developed by Mansour and co-workers[67,68] and its methodology applied to the study of electrocatalysis by Mukerjee *et. al.*[2,3]
A special *in-situ* spectro-electrochemical cell (described in detail elsewhere[69]) was used, which allowed XAS measurements in transmission mode with the working electrode in a fully flooded state. XAS measurements were conducted at beam line X-11 A at the National Synchrotron Light Source (NSLS) in Brookhaven National Laboratory. Data was collected at both the Pt L (L_3 and L_2) and the alloying element K edges in the transmission mode using an incident, transmission and reference ion chambers. A Pt foil at the reference detector provided accurate calibration and alignment of the edge positions. Details of the beam line optics and monochromator are given elsewhere.[25] The electrochemical control of the interface was enabled by a digital potentiostat/galvanostat (PGSTSAT 30, Autolab, Echochemie, Brinkmann Instruments). The electrolyte of choice for *in-situ* XAS measurements was 1 M $HClO_4$. Prior to acquiring the *in-situ* XAS spectra, electrodes were cycled at least 25 times, between 0.0 and 1.2 V. Since the purpose of the XANES experiment was primarily to determine the atomic ratio of Pt and the alloying element as well as the d-band vacancy of Pt/atom, the *in-situ* spectra was taken at 0.54 V vs. RHE. Data collected at this potential were devoid of interference due to adsorbed species, being in the double layer region and close to the potential of zero charge. XAS data was also collected as a function of potential in the range of 0.0 to 1.2 V vs. RHE for all the binary alloys in 1 M $HClO_4$. EXAFS analysis on the Pt L_3, Fe and Co K edges followed methodologies developed by Koningsberger *et al.*[70,71] the details of which are given elsewhere.[2,3,25,72] Phase and amplitude parameters from standard materials and theoretically calculated values from FEFF6 program using fcc crystal lattice parameters based on appropriate atomic ratios for the PtM alloys were used to fit those from the sample data. The standards used to calculate Pt-Pt and Pt-O interactions were liquid N_2 data for a pure Pt foil and $Na_2Pt(OH)_6$ respectively. A Gaussian pair distribution function (PDF) was used to fit the Pt-Pt and Pt-M (M=Co or Fe). Harmonic thermal vibrations and inter atomic PDF's can cause an underestimation of the coordination numbers. A cumulative expansion algorithm which also included the third and fourth terms from an asymmetrical PDF was used as fitting parameters and resulted in a 12 to 19% increase in the coordination numbers relative to the Gaussian PDF. Since, the observed deviations were random and the average bond distances of Pt-Pt and Pt-M increased by 0.02 ± 0.0002 Å, the effect of asymmetry in the samples was

16

considered negligible. Hence, the results reported hereafter are obtained from a Gaussian PDF. The effect of electrolyte environment on the electrocatalyst nanoclusters is not considered here and is the subject of a separate investigation. The use of $HClO_4$ in our *in-situ* XAS experiments was based on its negligible anion adsorption[22,73] with 1 M concentration, a situation akin to the case with trifluoromethane sulfonic acid.[44,57,74,75]

Results and Discussion

Characterization of the nanocluster size, crystallinity and atomic parameters: XRD and in-situ XAS measurements –

The XRD analysis of the electrocatalysts showed a very high degree of crystallinity. Fits of the XRD data to an indexing routine showed that all the patterns (Pt and Pt alloys) corresponded to an fcc lattice. Lattice parameters obtained are given in Table 1. In addition, the Pt-Pt bond distances based on an fcc lattice were calculated based on X-ray line broadening analysis using the Scherrer equation (Table 1). Evidently, alloying of Pt with Fe and Co results in a lowering of the lattice parameters and hence the Pt-Pt bond distances. From a comparison of the XRD pattern with a standard JCPDS database the binary Pt alloys were found to form an intermetallic crystalline structure with a primary Pt_3M type superlattice phase with an fcc structure and potential for a secondary PtM type lattice with a tetragonal structure. The extent of contribution from the secondary phase was estimated by the intensity of the diffraction lines due to the PtM phase (such as (001) and (220) diffraction lines in the PtM/C powder pattern). Contribution from these secondary phases was found to be negligible. The particle size obtained using the Pt (111) diffraction line broadening showed that the alloy catalysts have a particle size somewhat larger than for Pt/C. Table 1 shows that the particle size increases due to alloying [Pt/C < PtCo/C < PtFe/C].

The ratio of Pt:M (alloying elements, Co and Fe) in the electrocatalyst (Table 2) were determined from the edge jumps at the Pt L_3, Co and Fe K edges using the methodologies described elsewhere.[25] It is noteworthy that all the atomic ratios determined by XANES were in excellent agreement with nominal compositions projected from our preparation methodology. The XANES spectra used were measured *in-situ* at 0.54 V vs. RHE. As mentioned earlier in the experimental section, the choice of this potential was based on the fact that it is in the middle of the double layer region where the potential interferences from anionic adsorption as well as the usual redox processes associated in the hydrogen and oxygen regions of the voltammograms.

The Pt *d*-band vacancies were derived from analysis of the Pt L_3 and L_2 white lines of XANES. The L_2 and L_3 excitations are due to the transition of $2p_{1/2}$ and $2p_{3/2}$ electrons to the empty Fermi level. Dipole selection rules restrict the orbital angular quantum number transitions to ±1. Hence a transition of $2p_{3/2}$ to a $5d$-orbital is favored. An increase in the L_3 and L_2 whiteline peak is related to changes in *d*-band vacancy and reflects the extent of *d*-band occupancy. A detailed description of this methodology is provided in ref. 2 and references therein. The Pt *d*-band occupancies evaluated from the Pt L_3 and L_2 edge curves are given in Table 2 along with the Pt-M atomic ratio. Comparison at 0.54 V vs. RHE shows an increase in *d*-band vacancies per atom on alloying, this follows the trend Pt/C < PtFe/C < PtCo/C. This increase in *d*-band character of Pt follows closely with the electron affinity of the alloying metal. XANES also offers the ability to monitor the extent of alloying and the nature of the active surface.

Two sets of Pt alloy catalysts, (i) acid washed (1 M $HClO_4$ for 48 hours, room temperature) and (ii) unwashed PtM/C alloy catalyst, were held at 0.9 V vs. RHE and the XANES spectrum was recorded at the Pt L_3 and the M (Co or Fe) K edge for six to ten hours. The acid wash step followed by washing with deionized water ensures the removal of any non alloyed M metal from the surface of the carbon support prior to electrode fabrication. The XANES analysis at the metal M [Co or Fe] K edge as described elsewhere [54] showed clear

evidence of changes in the surface oxidation environment around the alloying elements Fe and Co, when the electrode was polarized at 0.9 V for the unwashed samples. Such a variation in the Fe and Co K edge XANES were however absent for extended durations of up to 9 hours with electrode polarized at 0.9 V for the washed electrocatalysts. No changes were detected at the Pt L_3 edge for Pt alloy catalysts polarized (washed and unwashed) with the electrode polarized at 0.9 V for up to 9 hours. These results are presented in a separate manuscript.[54] These results using XANES and the stability observations are consistent with the outer layer being pure Pt and the alloying metal further deep in the cluster has been suggested previously.[76] Theoretical calculations of the surface segregation energies of different transition metal alloys by Norskov et al.[77] using a Greens's Function Linear-Muffin-Tin-Orbital (GF-LMTO) calculations combined with a Density Functional theory (DFT) and Coherent Potential Approximation (CPA) showed a strong antisegregation effect in the case of a PtCo and PtFe alloy where the Co and Fe were considered as solutes in a Pt host. Positive segregation energies of 0.37 eV and 0.46 eV for Fe and Co respectively in a Pt host showed that the Fe and Co atoms prefer to remain in the interior of the alloy. The calculated segregation energies were based on a close packed surface, a system similar to the supported PtM alloys used in our study.

EXAFS Analysis –

The first step in the analysis of EXAFS is to extract the normalized EXAFS data from the raw XAS spectrum. After Pre-edge subtraction (-200eV to -50eV relative to Pt L_3 edge) and post edge background removal (+50eV to 1500eV above the Pt L_3 edge), the EXAFS spectra for supported Pt and Pt alloys were of good quality and underwent further Fourier filtering using windows shown in Table 2. A representative phase corrected forward Fourier transform of the k^3weighted EXAFS (*r*-space) at the Pt L_3 edge for Pt/C and PtCo/C at two potentials 0.54V and 0.84V (indicative of a clean region, 0.54V; and an oxide covered region, 0.84V respectively) are shown in Figures 1a and 1b. Comprehensive EXAFS analysis is typically done following the inverse Fourier transform of the *r*-space to analyze *k*-space amplitudes and to isolate the primary coordination shells of interest. Iterative least square fitting using one shell (Pt-Pt) or two shells (Pt-Pt + Pt-O, Pt-Pt + Pt-M) was then carried out on a simplistic model to get unique fits. Thus at 0.54V, a single shell (Pt-Pt) fit for Pt/C and a two shell model (Pt-Pt + Pt-M) fit for Pt-M alloys indicate no Pt-O interactions at this potential. However, at 0.84V a single shell model could not fit the data for a Pt/C but a two shell model (Pt-Pt + Pt-O) derived from a standard sample ($Na_2Pt(OH)_6$ at liq. N_2) could fit the data at this potential. In contrast to this, Pt alloys show no differences due to potential change since the same two shell model (Pt-Pt + Pt-M) at 0.54V was able to fit the data at 0.84V. Further, the effect of alloying on the Pt-Pt bond distances (Table 2) obtained from the EXAFS analysis of the Pt L_3 edge data show a contraction as a result of alloying and follows the same trend as determined by XRD [PtCo/C<PtFe/C<Pt/C]. These Pt-Pt bond distances and the coordination numbers (N) obtained for the alloys, Pt-Pt and Pt-M (Table 2) are in good agreement with expected coordination numbers using a cubo octahedron model described by Benfield.[78] Since the cubo-octahedron model of Benfield correlates overall coordination numbers to particle sizes, there was a good correlation of the data obtained from EXAFS with those obtained from the line broadening analysis of XRD. This is indicative of the fact that the electrocatalyst used in this study had an extremely high (close to 100%) degree of crystallinity. This was based on the fact that XRD which only reflects information from diffracting domains (hence systems with long range order) and EXAFS which only probes short range atomic order (Nearest shell interactions) were in good agreement. The change in *d*-band vacancies (Table 2) for the Pt and Pt alloys during potential transition from 0.54 V (double layer region) to 0.84 V vs. RHE (oxide covered layer) agrees with the EXAFS

analysis for Pt/C, there is an expected increase due to chemisorbed OH species on the surface at 0.84 V relative to 0.54 V, however such a change is absent for the alloys (Table 2).

Cyclic Voltammetry -

Figure 2a shows the steady-state cyclic voltammograms (CV) of a Vulcan XC-72R carbon supported Pt and PtCo in oxygen free 1 M trifluoromethane sulfonic acid (CF_3SO_3H) at 50 mV/sec with a metal loading of $14\mu g_{metal}/cm^2$. The carbon supported Pt particles posses some degree of low coordinated crystal planes and hence the hydrogen adsorption/desorption features between 0.4 V and 0 V vs. RHE are different from the CV expected of a bulk pc-Pt electrode. A Comparison of the voltammetry of Pt and PtCo in Fig.2a also shows the difference in the onset of oxide formation on Pt (accepted as Pt-OH) at around 0.7 V vs. RHE. PtCo/C exhibits a significantly lower extent of oxide formation. Fig.2b shows the voltammogram on Pt/C in 1 M and 6 M CF_3SO_3H at 50 mV/sec. It is interesting to note the differences in the cyclic voltammogram in 6 M CF_3SO_3H relative to the one obtained in a 1 M solution. In 6 M, the onset of the anodic oxide formation does not start until well beyond 0.9 V and is also less pronounced in the potential window below 1.2 V relative to a Pt/C in 1 M CF_3SO_3H. The onset of the anodic oxide film is directly related to the amount of free water available in the acid electrolyte hence the shift in the onset of the oxide formation in 6 M CF_3SO_3H at a potential beyond 0.9 V compared to that of 1 M CF_3SO_3H can be rationalized based on the lower activity of water in high concentrations of the acid. As mentioned in the experimental section, since the reference electrodes were made from the same concentration of electrolyte as used in the experiments [hereafter referred to as RHE1 and RHE6 for hydrogen electrodes made from 1 M and 6 M electrolytes respectively], measured potentials at the working electrode are corrected for any Nernst shifts due to change in concentration of the electrolyte and all the voltammograms recorded are a direct reflection of the effect of water activation. In 6 M CF_3SO_3H solution the number of free water molecules available would be less as a result of protonation of most of the free water molecules by CF_3SO_3H molecules. The number of water molecules associated with a molecule of CF_3SO_3H in a 6 molar solution is only ~4(mole ratio) as compared to 1 M CF_3SO_3H (~50). Consequently, the activity of water is low in a 6 M solution and hence the shift in the formation of an anodic oxide, on the electrode and also the cathodic reduction currents of the oxide layer at about 0.8 V. The hydrogen adsorption desorption features are poorly resolved in a 6 M CF_3SO_3H compared to a 1 M CF_3SO_3H probably due to more pronounced mass transport effect in the electrolyte as also shown by others. The issue of any poisoning of the Pt surface due to impurities in the electrolyte or due to any kind of anion adsorption effects would be detrimental for ORR in high concentrations of the acid and would lead to a reduced activity of the Pt. However, the improved ORR activity on Pt/C in a 6M TFMSA as would be shown in the next section suggests that the impurity effects from the acid can be neglected. A simple comparison of Fig.2a and Fig.2b suggests that the onset of an anodic oxide layer on Pt arising due to the oxidation of water molecules can be shifted by either alloying the Pt with metals that increase the *5d* band vacancies or by lowering the activity of water.

Oxygen Reduction Kinetics –

Fig. 3 shows the mass transport corrected Tafel plots obtained for a 6 mm diameter polycrystalline pc-Pt disk electrode on which oxygen reduction kinetics studies were conducted as a control experiment in 1 M and 6 M CF_3SO_3H. The Tafel plots are obtained after the measured currents are corrected for diffusion to give the kinetic currents. Assuming a first order reaction [57,79] for oxygen reduction, the kinetic current in the mixed activation-diffusion region is calculated from the equation

$$i_k = i_{lim} * i/(i_{lim} - i) \qquad [1]$$

where i_k is the kinetic current density, i is the measured current density during the oxygen reduction polarization and i_{lim} is the diffusion limited current density, also known as the Levich current density. In the absence of a Nafion layer on the electrode, the limiting current density i_{lim} on the rotating disk electrode obeys the Levich equation

$$i_{lim} = B \omega^{1/2} \qquad [2]$$

where, ω is the rotation rate and B is the Levich constant which is given as

$$B = 0.62 n_e F D^{2/3} v^{-1/6} C_o \qquad [3]$$

Where, n_e is the number of electrons transferred per oxygen molecule during reduction, D is the diffusion coefficient of O_2 in the electrolyte, C_o is the O_2 concentration in the solution and v is the kinematic viscosity. In the case of a Nafion film coated electrode, i_{lim} is dependant on the limiting current on the bare electrode and the diffusion through the Nafion film, assuming a steady state concentration of oxygen at the electrolyte-film interface, this is expressed as

$$1/i_{lim} = 1/i_d + 1/i_f \qquad [4]$$

where i_d is the diffusion limited current on the bare electrode and i_f is the limiting current controlled by the transport of the reactant through the film and is given by the equation

$$i_f = n_e F D_f C_f / \delta_f \qquad [5]$$

In this equation D_f, C_f and δ_f are the diffusion coefficient of O_2, concentration of O_2 and thickness of the Nafion film respectively. The effect of the film diffusion is significant only in the case of an electrode covered by a Nafion film[22] and can be neglected in the present study since the amount of Nafion (20µL in 5 mL of solution) in the prepared catalyst suspension is sufficiently small and hence not expected to be a factor in the limiting current density on the rotating electrode where only 20µL of catalyst ink is loaded resulting in 14µg/cm^2 of catalyst and 0.08µL of Nafion. The oxygen reduction reaction current can be written as dependant on the kinetic current and the diffusion limited current as shown in equation 6.

$$1/i = 1/i_{lim} + 1/i_k = 1/B \omega^{1/2} + 1/i_k \qquad [6]$$

In 1 M CF_3SO_3H, two Tafel slopes of 60 mV/dec at low current density and 120 mV/dec at high current density are observed (Fig.3) on a pc-Pt plug. The transition from 60mV/dec to 120mV/dec is closely related to the adsorbed OH species on Pt at potentials beyond 0.8 V vs. RHE. A Tafel slope of -2RT/F i.e., 120mV/dec in the high overpotential region (h.o.r) is indicative of a surface that is clean hence devoid of any species that can affect the adsorption of O_2 from the solution to the active surface for reduction. However, in 6 M CF_3SO_3H, a single Tafel slope of 120mV/dec was obtained in the entire potential range which is indicative of a clean active surface for oxygen reduction due to the lowering of water activation and hence lowering the poisoning effects of OH_{ads}.

Fig. 4 shows the current density vs. potential curves at different rotation rates (625, 900, 1225 rpm) for a carbon (Vulcan XC-72R) supported Pt in 1 M and 6 M CF_3SO_3H at room temperature. The oxygen reduction is under a mixed kinetic and diffusion control in the potential range 0.9 V and 0.6 V followed by a purely diffusion limited region. The lower diffusion limiting currents in 6 M CF_3SO_3H as compared to 1 M CF_3SO_3H can be explained on the basis of differences in diffusion coefficient and solubility of oxygen in these solutions. The diffusion coefficient and solubility of oxygen in these electrolytes were measured using a micro electrode technique as described elsewhere[80] and are given in Table 3 along with the values found in literature for CF_3SO_3H. In a rotating disk electrode experiment the permeability of oxygen to the electrode surface at a given rotation rate is dependant on $D^{2/3} v^{-1/6} C_o$ term in the Levich constant (B in equation 3) and differences in the diffusion coefficient, concentration of oxygen and kinematic viscosity between 1 M and 6 M TFMSA are directly reflected in the diffusion limiting currents obtained in these electrolyte concentrations. Although the concentration of oxygen in 6 M CF_3SO_3H is significantly higher than that of 1 M electrolyte (Table 3), the diffusion coefficient shows quite an opposite trend and the product of

D and C are very similar for 1 M and 6 M TFMSA. However, incorporating the kinematic viscosity (shown in Table 3) into the Levich Equation, the diffusion limited currents follows the same trend as the overall permeability of oxygen ($D^{2/3}v^{-1/6}C_o$) to the electrode surface in these electrolytes to a good approximation.

It can be seen from Fig. 4 that the rate of increase in cathodic currents due to ORR in 6 M CF_3SO_3H is faster than that in 1 M CF_3SO_3H even though the limiting current density is lower as mentioned above due to oxygen permeability in these electrolytes. In the mixed potential range between 0.9 V and 0.6 V, at a given current density, Pt/C in 6 M CF_3SO_3H exhibits ~40mV lower overpotential than Pt/C in 1 M CF_3SO_3H. This can be correlated to the number of Pt sites that are covered by surface adsorbed -OH species which are greatly reduced in 6 M acid concentration. The inset in Fig.4 shows the mass transport corrected Tafel slopes obtained for the Pt/C in 1 M and 6 M CF_3SO_3H. It can be seen that a Pt/C exhibits the same Tafel behavior as a bulk polycrystalline pc-Pt in both 1 M and 6 M TFMSA. A single slope of 120mV/dec in 6 M TFMSA is indicative of a clean active surface of Pt for the reduction of oxygen and a lowering in the overpotential by about 40mV is a direct consequence of inhibition of OH_{ads} on the surface due to the lower activity of water in 6 M CF_3SO_3H.

The current density vs. potential curves for oxygen reduction on PtCo/C and PtFe/C in 1 M and 6 M CF_3SO_3H measured at various rotation speeds are shown in Figures 5 and 6 respectively. The kinetic data for all the electrocatalysts are compared and summarized in Table 4. Compared to the Pt/C in 1 M TFMSA, the 1 M data for PtCo/C and PtFe/C show significantly improved kinetic currents for ORR. The kinetic currents follow the trend Pt/C < PtFe/C< PtCo/C (Table 4). All the kinetic currents are based on a metal geometric loading of 14μg/cm². The kinetic currents for PtFe/C and PtCo/C alloys would show a much higher improvement when compared on the basis of electrochemically active surface areas (Table 4) of Pt. However, in 6 M CF_3SO_3H the Pt-M/C (M=Fe and Co) alloys do not show the same trend in their kinetic currents compared to Pt/C. The activity of Pt/C is higher than the Pt-M/C alloys for ORR in 6 M TFMSA in contrast to that observed in 1 M concentration. This implies that although a change in Pt d- band vacancies in Pt-M alloys improves their oxygen reduction kinetics in a fully hydrated environment (1 M concentration) by lowering the anodic oxidation of water, it fails to explain the improved kinetics for a Pt/C in 6 M TFMSA. Hence a strategy to enable lower water activation without significantly affecting the d- band vacancy appears to be the best option. In summary, Figures 7 and 8 shows the comparison of the supported Pt with PtFe/C and PtCo/C in 1 M and 6 M CF_3SO_3H at a rotation rate of 1225rpm respectively. In 1 M CF_3SO_3H (Fig. 7), the supported PtM alloys show improved oxygen reduction kinetics than Pt/C above 0.8 V. This enhanced ORR kinetics is an indication of the shift in the formation of an oxide layer on Pt, facilitated by alloying with transition metals which increase the d band character of Pt. This is also reflected in a single Tafel slope of 120 mV/dec observed in the PtM alloy catalysts (inset in figure 7) whereas Pt/C shows two slopes of 60 and 120 mV/dec (inset in figure 4). However, comparing the three electrocatalysts in 6 M CF_3SO_3H (Fig. 8) shows a complete reversal of oxygen reduction kinetics following the trend PtFe/C < PtCo/C < Pt/C. Although the results discussed so far indicate that alloying Pt with transition metals and altering its d band character does not improve its activity for oxygen reduction kinetics at low water content, the alloy electrocatalysts have more implications on the stability of catalysts in terms of its effect on their oxygen reduction reaction pathways which is an important factor to consider towards the stability of the polymer electrolyte-electrode interface

The activation energies for oxygen reduction reaction for the various electrocatalysts were evaluated at a fixed electrode potential based on a modified Arrhenius equation as shown below

$$\left(\frac{\partial \log(i_k)}{\partial(1/T)} \right)_E = \frac{Ea^*}{2.3R} \qquad [7]$$

The procedure for calculating the activation energies at different electrode potentials followed the steps described in detail elsewhere.[61,65]

The activation energies determined in 1 M CF_3SO_3H using a linear regression analysis for the three different electrocatalysts are shown in Table 5. The data shows that within the limits of error, there is very little difference between the activation energies of Pt and PtCo alloy electrocatalysts. PtFe/C does show a smaller value which follows similar trend with change in electrode potentials as Pt/C and PtCo/C. The reason for this consistently lower value is not well understood. Such a similarity in activation energy between Pt/C and PtCo/C alloy electrocatalysts are in close agreement with previously published report by Paulus et al.[65] where three different electrocatalysts Pt/C, PtCo/C and PtNi/C were examined in 0.1 M $HClO_4$ using a similar RRDE technique. The activation energies reported at three different overpotentials (0.3, 0.35 and 0.4 V) with respect to the theoretical reversible potential for oxygen reduction of 1.23V were in very close agreement to those found in our work. However, in their report, no trend with respect to overpotential was discerned. Our results show a trend with respect to overpotential (electrode potential varied between 0.9 V and 0.7 V) vs. RHE. The implication of this trend is complicated and will be discussed in a later publication.[81] However, the close values of activation energies between Pt and Pt alloys in 1 M TFMSA clearly indicates that the differences in oxide layer formation on Pt alloys as compared to Pt is primarily linked to the pre exponential term in the Arrhenius rate expression. This can be explained on the basis of a conventional rate expression as shown in equation 8 which involves using transition states and their surface coverage as determined by Markovic et al.[65,82] assuming that the first electron transfer for oxygen reduction as the rate determining step.

$$i = nFkC_o(1-\Theta_{ads}) \exp(-\beta FE/RT) \exp(-\gamma r\Theta_{ads}/RT) \qquad [8]$$

where E is the applied potential, i is the observed current density, n is the number of electrons, k is the rate constant, C_o is the concentration of oxygen, Θ_{ads} is the surface coverage of adsorbed intermediates, β and γ are the symmetry factors. Here, the term $r\Theta_{ads}$ was related to the apparent Gibbs energy of adsorption associated with surface coverage of an oxide layer. The close values of the activation energies observed for all the three electrocatalyst also suggests that the transition state in the activation energy profile therefore remains unchanged. Anderson et al.[83-85] have previously shown that the activation energy for ORR decreased with increase in overpotential which is consistent with the observed activation energies in this work for all the three electrocatalysts. The Ab Initio calculations[85] for a series of four 1 electron oxygen reduction reaction based on electronic equilibrium of the transition state complex with the electrode potential predicted that the activation energies for all the four steps decreased with increase in overpotential with the H_2O_2 (intermediate) reduction having the highest activation energy followed by the first electron reduction of oxygen. The reduction of an ·OOH and ·OH intermediates were calculated to have the lowest activation energies. The decrease in activation energies with increasing overpotential found experimentally in this study is in close agreement with the activation energies found theoretically and follows the same trend as predicted by the theory.

Oxygen reduction pathway on Pt/C and Pt alloys –

The reaction pathway for oxygen reduction reaction for the formation of relative amounts of H_2O_2 and H_2O can be determined quantitatively with an RRDE experiment by holding the potential of the ring at a constant potential of 1.2 V where the H_2O_2 formed on the disk during oxygen reduction is readily oxidized. Fig. 9 a shows the currents (I_R) obtained on a

22

gold ring electrode during oxygen reduction on Pt/C in 1 M and 6 M CF$_3$SO$_3$H at 1225rpm. The ring currents are negligible in the potential region above 0.6 V in 1 M CF$_3$SO$_3$H indicating that the reduction of oxygen proceeds almost completely by a four electron transfer above this potential which is relevant for the operating potential of fuel cell cathodes. However, the ring currents in 6 M CF$_3$SO$_3$H although relatively very small compared to four electron ORR, shows ~4 fold enhancement compared to 1 M CF$_3$SO$_3$H. This is very significant with regard to choice of polymer electrolyte membranes in fuel cells where H$_2$O$_2$ is a potential source of degradation of membranes with prolonged exposure. Especially for non-fluorinated membranes currently being considered as potential replacement for Nafion type polymer electrolytes in a quest for elevated (up to 130°C) temperature operation. Most of these membranes are based on engineered polymers with high thermo-chemical stability[86], typically with high degree of aromatic character, where the monomer consists of a variety of fused phenyl rings linked together with a number of bridging aromatic backbones and consisting of sulfonic acid substituted aromatic rings. Of the two degradation mechanisms postulated for non-fluorinated membranes during the long-term fuel cell operations, (1) Oxygen diffusing through the membrane to the anode where the HOO$^\bullet$ radicals formed at the surface of the catalyst attacks the tertiary hydrogen at the α-carbon of the polymer[87,88]; (2) Oxygen reduction at the cathode proceeding through a peroxide intermediate (H$_2$O$_2$), which reacts with trace metal ions in the membrane to form HOO$^\bullet$ and HO$^\bullet$ radicals, which in turn results in membrane degradation at cathode during oxygen reduction reaction,[43] the latter is directly linked to cathode electrode electrocatalysis.

Table 6 shows the relative amounts of H$_2$O$_2$ (%H$_2$O$_2$ formed compared to ORR) formed on the electrocatalyts in 1 M and 6 M CF$_3$SO$_3$H based on the equation

$$\chi_{H_2O_2} = \frac{2I_R / N}{I_D + I_R / N} \qquad [9]$$

$$* N = 0.2$$

where, N is the collection efficiency of the ring, χ is the mole fraction of peroxide formed, I_D and I_R are the disk and ring currents, taking into account the total disk currents for the oxygen reduction as the sum of reduction currents of O$_2$ to H$_2$O and H$_2$O$_2$ and the collection efficiency N for the ring electrode.[61] At the typical operating potentials of a fuel cell 0.7 V, H$_2$O$_2$ formation at steady state is ~ 0.11% in 1 M CF$_3$SO$_3$H and ~0.42% in 6 M CF$_3$SO$_3$H on a 20%Pt/C electrode. However, the amounts of peroxides formed on supported Pt alloys (PtCo/C and PtFe/C) are very different. The amount of peroxides formed on a PtCo/C in 1 M and 6 M CF$_3$SO$_3$H show almost the same trend as the Pt/C, however the ring current detected in 6 M TFMSA is significantly lower than that of Pt/C (Fig. 9b). Also the ORR kinetic currents on PtCo/C did not show any dramatic enhancement between 1 M and 6 M CF$_3$SO$_3$H whereas the Pt/C showed a significant increase in the kinetic currents due to oxygen reduction in 6 M CF$_3$SO$_3$H . This suggests that the oxygen reduction may have a small but negligible peroxide formation step on Pt/C. This tends to agree with a simultaneous mechanism as suggested by Damjanovic et al.[13] where some small part of the oxygen reduction reaction goes through peroxide intermediate. However, the peroxide formation on a PtFe/C showed a contrasting behavior. The considerable decrease in the ORR kinetic currents for PtFe/C (Fig. 6) in 6 M CF$_3$SO$_3$H compared to that in 1 M CF$_3$SO$_3$H would be expected to generate lower peroxide currents at the ring if it were to follow the previous trend. In contrast to PtCo/C, PtFe/C shows a large increase in peroxide yield at 6M concentration. This shows that choice of alloy element has a significant effect on parallel pathway for ORR where activity of water is low. Further, peroxide currents exhibit a greater increase with decrease in potentials for PtFe/C in 6 M concentration as compared to Pt/C and PtCo/C (Table 7). Since we started with a PtFe/C with predominantly a Pt skin,[2,77] and the increase in the peroxide current on a PtFe/C in 6 M CF$_3$SO$_3$H suggests possibility of Fe atoms on the electrocatalyst surface, further

surface studies in high concentrations of TFMSA are needed to get a better understanding of the electrocatalytic activity of these Pt M/C (M = transition metal) alloys.

Conclusions

From the results discussed above it is evident that the oxygen reduction reaction on an electrocatalyst surface depends on the nature of Pt surface (alloyed or unalloyed) as determined by the surface electronic properties which affects water activation in a fully hydrated state. Alloying Pt with transition metals such as Co and Fe followed by a washing step in 1 M $HClO_4$ (24 to 48 hours) enables an alloy inner core with an outer layer rendered predominantly Pt. The consequence of such alloy nanoparticle formation is a significant lowering of water activation beyond 0.8 V vs. RHE, in contrast to Pt/C.

The lower affinity towards water activation in fully hydrated environment (1 M TFMSA) for Pt alloys in contrast to Pt is manifested in the observed Tafel slope which is 120 mV/decade (2RT/F) for the alloys in contrast to the expected value of 60 mV/decade, observed on both pc-Pt and Pt/C. Such a lowering of affinity towards water activation on Pt alloys in 1 M concentration is also reported using cyclic voltammograms as well as *in-situ* XAS data. Both the *in-situ* XANES and EXAFS data analysis comparing Pt L_3 edge spectra at 0.54 V and 0.84 V vs. RHE for alloys clearly indicate lack of any oxide coverage. This is in contrast to Pt/C, where, as expected an increase in white line intensity (directly related to Pt *d*-band vacancy) is observed at 0.84 V relative to 0.54 V due to formation of Pt oxides. Comparison of Pt L_3 edge EXAFS data confirms this and provides an alternative probe of this phenomenon.

Such a lowering of affinity of oxide formation, a surface poison for molecular oxygen adsorption on Pt alloys in the fully hydrated analog (1 M TFMSA) is correlated to a concomitant increase in ORR activity as shown by RDE data. However, a lowering of water activity resulting from a shift in concentration to 6 M shows that while there is an increase in ORR activity for Pt/C due to lowering of surface oxide formation, a corresponding effect with Pt alloys does not occur. This further supports our earlier contention of ORR activity being dependant on surface coverage by oxides. Further, a more important conclusion from the lack of increased activity for Pt alloys in 6 M concentration of TFMSA is that the process of alloying with transition metals does not render the surface of the catalyst to be inherently more active for oxygen reduction, in contrast to the increased activity observed for the alloys in 1 M concentration. This is related to a wealth of prior literature as discussed in our results and discussion section where the rate limiting step for oxygen reduction reaction in a fully hydrated state (1 M concentration) is the initial dissociative adsorption of molecular oxygen. Significant changes to the electronic states of Pt as a consequence of alloying could affect the affinity for molecular oxygen adsorption. This is a strong possibility supported by our data in 6 M TMFSA; its confirmation is a subject of theoretical simulations, which are currently being conducted by us.

Measured activation energies at 1 M concentration shows very close values between Pt/C and PtCo/C with PtFe/C somewhat lower. These activation energies also exhibited a common trend wherein a lowering was observed with increase in overpotential. The relatively similar values of activation energy for Pt and Pt alloys seem to indicate that the differences in ORR activity arises primarily from contributions to the pre-exponential term in the Arrhenius expression, of which the prime contributor is the surface coverage of oxides. The similar trend of changes in activation energy values with electrode potential requires more theoretical insight which will be the subject of a separate manuscript.

The issue of relative yield of peroxides on the Pt and Pt alloy surface in 1 M and 6 M TFMSA shows interesting variations. Peroxide yield albeit small (less than one percent of 4 electron oxygen reduction) was observed below 0.6V vs. RHE in both 1 and 6 M TFMSA, exhibiting an exponential rise with overpotential. However, comparison of Pt and Pt alloys at 1 M concentration in the potential region below 0.6 V shows that peroxide yield is similar on

all the electrocatalysts. Transition to 6 M concentration however causes a much bigger enhancement in peroxide yield for PtFe/C followed by Pt/C and was least for PtCo/C. This sensitivity of peroxide yield with choice of electrocatalyst has the potential of major impact on interfacial stability, especially for non fluorinated membranes operating at elevated temperature under less than 100% relative humidity conditions.

Overall the observation of lower inherent activity for molecular oxygen reduction in Pt alloy electrocatalysts when the issue of water activation is removed as an influence (such as higher concentration acid environment without concomitant poisoning with anionic species etc) has the potential for a major impact in our choice of alloying elements. Much more work needs to be done for enabling better tuning of the Pt electronic states (which are responsible for controlling the affinity for water activation and adsorption of molecular oxygen) by processes such as alloying (in this case) and others such as introduction of metal polymer interactions.

References and Notes

(1)   Mukerjee, S.; Srinivasan, S. *J. Electroanal. Chem.* **1993**, *357*, 201.

(2)   Mukerjee, S.; Srinivasan, S.; Soriaga, M. P. *J. Electrochem. Soc.* **1995**, *142*, 1409.

(3)   Mukerjee, S.; Srinivasan, S.; Soriaga, M. P.; McBreen, J. *J. Phys. Chem.* **1995**, *99*, 4577.

(4)   Tamizhmani, G.; Capuano, G. A. *J. Electrochem. Soc.* **1994**, *141*, 968.

(5)   Friedrich, K. A.; Beck, T.; Garche, J.; Stimming, U. *Abstracts of Papers, 223rd ACS National Meeting, Orlando, FL, United States, April 7-11, 2002* **2002**, COLL.

(6)   Kalhammer, F. R.; Prokopius, P. R.; Roan, V. R.; Voecks, G. E. *in 'Status and Prospects of Fuel Cells as Automotive Engines', Air Resources Board, California Environmental Agency*, Eds., July 1998.

(7)   Srinivasan, S. *J. Electrochem. Soc.* **1989**, *136*, 41C.

(8)   Appleby, A. J.; Foulkes, F. R. *Fuel Cell Handbook, van Nostrand Reinhold*, , Eds.New York, 1989.

(9)   Wroblowa, H.; Rao, M. L. B.; Damjanovic, A.; Bockris, J. O. M. *J. Electroanal. Chem. Interfacial Electrochem.* **1967**, *15*, 139.

(10)   Bockris, J. O. M.; Srinivasan, S. Fuel Cells: Their Electrochemistry; McGraw Hill,: New York, 1969, p469.

(11)   Mukerjee, S. In-Situ X-Ray Absorption of Carbon Supported Pt and Pt Alloy Electrocatalysts: Correlation of Electrocatalytic Activity with particle Size and Alloying. In *Catalysis and Electrocatalysis at Nanoparticle surfaces* Wieckowski, A., Savinova, E. R., Vayenas, C. G., Eds.; Marcel Dekker, Inc., 2003.

(12)   Adzic, R. R. *in Electrocatalysis, (J. Lipkowski and P. N. Ross, Eds.)*, Eds.Wiley-VCH, Inc., p197,, 1998.

(13)   Damjanovic, A.; Brusic, V.; Bockris, J. O. M. *J. Phys. Chem.* **1967**, *71*, 2741.

(14)   Yeager, E.; Razaq, M.; Gervasio, D.; Razaq, A.; Tryk, D. *Proceedings - Electrochemical Society* **1992**, *92-11*, 440.

(15)   Yeager, E.; Razaq, M.; Gervasio, D.; Razaq, A.; Tryk, D. *J. Serb. Chem. Soc.* **1992**, *57*, 819.

(16)   Clouser, S. J.; Huang, J. C.; Yeager, E. *J. Appl. Electrochem.* **1993**, *23*, 597.

(17)   Yeager, E. "Electrocatalysts for oxygen electrodes: final report," Dep. Chem., Case West. Reserve Univ., Cleveland, OH, USA. FIELD URL:, 1990.

(18)   Yeager, E. *Electrochim. Acta* **1984**, *29*, 1527.

(19)   Tarasevich, M. R.; Vilinskaya, V. S. *Electrokhimiya* **1973**, *9*, 96.

(20)   Adzic, R. R. *in Structural Effects in Electrocatalysis and Oxygen Electrochemistry, Proc. Vol. 92-11. (D. D. Scherson, D. Tryk, M. Daroux, and X. Xing eds)*, The Electrochemical Society, Pennington, NJ (1992), p 419 Eds.

(21)   Uribe, F. A.; Springer, T. E.; Wilson, M. S.; Zawodzinski, T. A., Jr.; Gottesfeld, S. *Proceedings - Electrochemical Society* **1996**, *95-26*, 50.

(22)   Markovic, N. M.; Gasteiger, H. A.; Ross, P. N., Jr. *J. Phys. Chem.* **1995**, *99*, 3411.

(23)   Faguy, P. W.; Marinkovic, N. S.; Adzic, R. R. *Langmuir* **1996**, *12*, 243.

(24)   Mukerjee, S.; McBreen, J. *Proceedings - Electrochemical Society* **1996**, *96-8*, 421.

(25)   McBreen, J.; Mukerjee, S. *J. Electrochem. Soc.* **1995**, *142*, 3399.

(26)   Jalan, V.; Taylor, E. J. *J. Electrochem. Soc.* **1983**, *130*, 2299.

(27)   Paffett, M. T.; Beery, J. G.; Gottesfeld, S. *J. Electrochem. Soc.* **1988**, *135*, 1431.

(28)   K. Kinoshita. *J. Electrochem. Soc.* **1990**, *137*, 845.

(29)   Beard, B. C.; Ross, P. N. *J. Electrochem. Soc.* **1990**, *130*, 3368.

(30)   Mukerjee, S. *J. Appl. Electrochem.* **1990**, *20*, 537.

(31)   Conway, B. E.; Novak, D. M. *J. Electrochem. Soc.* **1981**, *128*, 956.

(32)   Mukerjee, S.; McBreen, J.; Srinivasan, S. *Proc. - Electrochem. Soc.* **1996**, *95-26*, 38.

(33)   Habib, M. A.; Bockris, J. O. *J. Electrochem. Soc.* **1983**, *130*, 2510.

(34)   Enayetullah, M. A.; DeVilbiss, T. D.; Bockris, J. O. M. *J. Electrochem. Soc.* **1989**, *136*, 3369.

(35)   Zinola, C. F.; Triaca, W. E.; Arvia, A. J. *J. Appl. Electrochem.* **1995**, *25*, 740.

(36)   Zinola, C. F.; Luna, A. M. C.; Triaca, W. E.; Arvia, A. J. *J. Appl. Electrochem.* **1994**, *24*, 119.

(37)   Paulus, U. A.; Wokaun, A.; Scherer, G. G.; Schmidt, T. J.; Stamenkovic, V.; Markovic, N. M.; Ross, P. N. *Electrochim. Acta* **2002**, *47*, 3787.

(38)   Zinola, C. F.; Luna, A. M. C.; Triaca, W. E.; Arvia, A. J. Electroreduction of molecular oxygen on preferentially oriented platinum electrodes in acid solution. In *J. Appl. Electrochem.*, 1994; Vol. 24; pp 119.

(39)   Zinola, C. F.; Triaca, W. E.; Arvia, A. J. Kinetics and mechanism of the oxygen electroreduction reaction on faceted platinum electrodes in trifluoromethanesulfonic acid solutions. In *J. Appl. Electrochem.*, 1995; Vol. 25; pp 740.

(40)   Paulus, U. A.; Wokaun, A.; Scherer, G. G.; Schmidt, T. J.; Stamenkovic, V.; Markovic, N. M.; Ross, P. N. Oxygen reduction on high surface area Pt-based alloy catalysts in comparison to well defined smooth bulk alloy electrodes. In *Electrochimica Acta*, 2002; Vol. 47; pp 3787.

(41)   Adzic, R. R. *in Electrocatalysis, Proc. Symp. (W. E. O'Grady, P. N. Ross and F. G. Will eds)*, The Electrochemical Society, Pennington, NJ (1992), p 419 Eds.

(42)   Anastasijevic, N. A.; Vesovic, V.; Adzic, R. R. *J. Electroanal. Chem. Interfacial Electrochem.* **1987**, *229*, 305.

(43)   Guo, Q.; Pintauro, P. N.; Tang, H.; O'Connor, S. *J. Membrane Sci.* **1999**, *154*, 175.

(44)   Kotz, R.; Clouser, S.; Sarangapani, S.; Yeager, E. *J. Electrochem. Soc.* **1984**, *131*, 1097.

(45)   Habib, M. A.; Bockris, J. O. *Compr. Treatise Electrochem.* **1980**, *1*, 135.

(46)   Hyde, P. J.; Maggiore, C. J.; Redondo, A.; Srinivasan, S.; Gottesfeld, S. *J. Electroanal. Chem. Interfacial Electrochem.* **1985**, *186*, 267.

(47)   Enayetullah, M. A. Ph.D. Thesis. Ph.D. Thesis, Case Western Reserve University, 1986.

(48)   Conway, B. E.; Novak, D. M. Hysteresis in Formation and Reduction of Submonolayer Quantities of Surface Oxide at Pt in an Almost Anhydrous Solvent. In *J. Electrochem. Soc.*, 1981; Vol. 128; pp 956.

(49)   Enayetullah, M. A.; DeVilbiss, T. D.; Bockris, J. O. M. Activation parameters for oxygen reduction kinetics in trifluoromethanesulfonic acid systems. In *Journal of the Electrochemical Society*, 1989; Vol. 136; pp 3369.

(50)   Jalan, V. M.; Bushnell, C. L. Highly-dispersed catalytic platinum. In *U.S.*; (United Technologies Corp., USA). Us, 1979; pp 4 pp.

(51)   Jalan, V. M. Cathode alloy electrocatalysts. In *Eur. Pat. Appl.*; (Giner, Inc., USA). Ep, 1985; pp 10 pp.

(52)   Landsman, D. A.; Luczak, F. J. Precious metal-chromium alloy catalyst for fuel cell electrodes. In *Belg.*; (United Technologies Corp., USA). Be, 1981; pp 16 pp.

(53)   Stonehart, P.; Watanabe, M.; Yamamoto, N.; Nakamura, T.; Hara, N.; Tsurumi, K. Platinum alloy electrode catalyst. In *Jpn. Kokai Tokkyo Koho*; (Stonehart Associates Inc., USA). Jp, 1992; pp 5 pp.

(54)   Urian, R. C.; Murthi, V. S.; Mukerjee, S. *in preparation*.

(55)   Gong, S.; Lu, J.; Yan, H. *J. Electroanal. Chem.* **1997**, *436*, 291.

(56)   Will, F. G. *J. Electrochem. Soc.* **1986**, *133*, 454.

(57)   Ross, P. N.; Andricacos, P. C. *J. Electroanal. Chem. Interfacial Electrochem.* **1983**, *154*, 205.

(58)   Parthasarathy, A.; Brumlik, C. J.; Martin, C. R. *Polym. Mater. Sci. Eng.* **1993**, *68*, 117.

(59)   Holdcroft, S.; Abdou, M. S.; Beattie, P.; Basura, V. *New Mater. Fuel Cell Mod. Battery Syst. II, Proc. Int. Symp., 2nd* **1997**, 861.

(60)   Lee, H. S.; Yang, X.-o.; McBreen, J.; Xiang, C. Boron compounds as anion binding agents for nonaqueous battery electrolytes. In *U.S.*; (Brookhaven Science Associates, USA). Us, 2000; pp 11 pp.

(61)   Paulus, U. A.; Schmidt, T. J.; Gasteiger, H. A.; Behm, R. J. *J. Electroanal. Chem.* **2001**, *495*, 134.

(62)   Gojkovic, S. L.; Zecevic, S. K.; Savinell, R. F. *J. Electrochem. Soc.* **1998**, *145*, 3713.

(63)   Zecevic, S. K.; Wainright, J. S.; Litt, M. H.; Gojkovic, S. L.; Savinell, R. F. *J. Electrochem. Soc.* **1997**, *144*, 2973.

(64)   Schmidt, T. J.; Paulus, U. A.; Gasteiger, H. A.; Alonso-Vante, N.; Behm, R. J. *J. Electrochem. Soc.* **2000**, *147*, 2620.

(65)   Paulus, U. A.; Wokaun, A.; Scherer, G. G.; Schmidt, T. J.; Stamenkovic, V.; Radmilovic, V.; Markovic, N. M.; Ross, P. N. *J. Phys. Chem. B* **2002**, *106*, 4181.

(66)   Wong, J.; Lytle, F. W.; Messmer, R. P.; Maylotte, D. H. *Phys. Rev. B: Condensed Matter and Materials Physics* **1984**, *30*, 5596.

(67)   Mansour, A. N.; Cook, J. W., Jr.; Sayers, D. E.; Emrich, R. J.; Katzer, J. R. *J. Catalysis* **1984**, *89*, 462.

(68)   Mansour, A. N.; Cook, J. W., Jr.; Sayers, D. E. *J. Phys. Chem.* **1984**, *88*, 2330.

(69)   McBreen, J. *Phys. Electrochem.* **1995**, 339.

(70)   Van Zon., J. B. A. D.; Koningsberger, D. C.; Van't Blik., H. F. J.; Sayers, D. E. *J. Chem. Phys.* **1985**, *82*, 5742.

(71)   Duivenvoorden, F. B. M.; Koningsberger, D. C.; Uh, Y. S.; Gates, B. C. *J. Am. Chem. Soc.* **1986**, *108*, 6254.

(72)   Mukerjee, S.; Urian, R. C. *Electrochim. Acta* **2002**, *47*, 3219.

(73)   Uribe, F. A.; Springer, T. E.; Gottesfeld, S. *J. Electrochem. Soc.* **1992**, *139*, 765.

(74)   Gonzalez, E. R.; Srinivasaan, S. *Electrochim. Acta* **1982**, *27*, 1425.

(75)   Zelenay, P.; Habib, M. A.; Bockris, J. O. M. *J. Electrochem. Soc.* **1984**, *131*, 2464.

(76)   Mukerjee, S.; Srinivasan, S.; Soriaga, M. P. Role of structural and electronic properties of Pt and Pt alloys on electrocatalysis of oxygen reduction. An in situ XANES and EXAFS investigation. In *J. Electrochem. Soc.*, 1995; Vol. 142; pp 1409.

(77)   Ruban, A. V.; Skriver, H. L.; Norskov, J. K. *Phys. Rev. B: Condensed Matter and Materials Physics* **1999**, *59*, 15990.

(78)   Benfield, R. E. *J. Chem Soc., Faraday Trans.* **1992**, *88*, 1107.

(79)   Ross, P. N.; Cairns, E. J.; Striebel, K.; McLarnon, F.; Andricacos, P. C. *Electrochim. Acta* **1987**, *32*, 355.

(80)   Zhang, L.; Ma, C.; Mukerjee, S. *Electrochim. Acta* **2003**, *48*, 1845.

(81)   Anderson, A. B.; Roques, J.; Mukerjee, S.; Murthi, V. S.; Markovic, N. M.; Stamenkovic, V. *in preparation*.

(82)   Markovic, N. M.; Gasteiger, H. A.; Grgur, B. N.; Ross, P. N. *J. Electroanal. Chem.* **1999**, *467*, 157.

(83)   Anderson, A. B.; Albu, T. V. *Electrochem. Comm.* **1999**, *1*, 203.

(84)   Anderson, A. B.; Albu, T. V. *J. Am. Chem. Soc.* **1999**, *121*, 11855.

(85)   Anderson, A. B.; Albu, T. V. *J. Electrochem. Soc.* **2000**, *147*, 4229.

(86)   Kopitzke, R. W.; Linkous, C. A.; Nelson, G. L. *Polymer Degradation Stability* **2000**, *67*, 335.

(87)   Buchi, F. N.; Gupta, B.; Haas; Scherer, G. G. *Electrochim. Acta* **1995**, *40*, 345.

(88)   Scherer, G. G. *Ber. Bunsen-Ges. Phys.Chem.* **1990**, *94*, 1008.

(89)   Hsueh, K. L.; Gonzalez, E. R.; Srinivasan, S. *Electrochim. Acta* **1983**, *28*, 691.

(90)   Parthasarathy, A.; Srinivasan, S.; Appleby, A. J. *J. Electrochem. Soc.* **1992**, *139*, 2530.

(91)   Paulus, U. A.; Wokaun, A.; Scherer, G. G.; Schmidt, T. J.; Stamenkovic, V.; Radmilovic, V.; Markovic, N. M.; Ross, P. N. *Journal of Physical Chemistry B* **2002**, *106*, 4181.
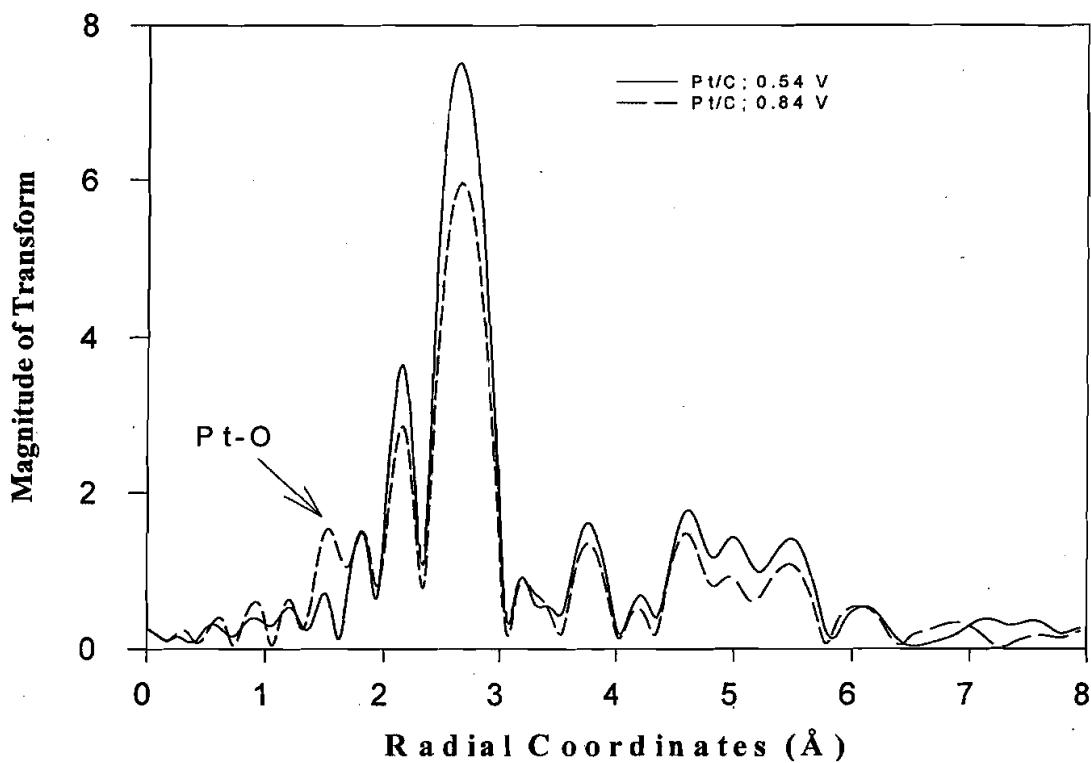
Figure 1a. Comparison of k^3 weighted Fourier transform at the Pt L$_3$ edge (r space) measured *in-situ* at 0.54 V and 0.84V vs. RHE for 20%Pt/C (Fourier filtering windows in Table 2).
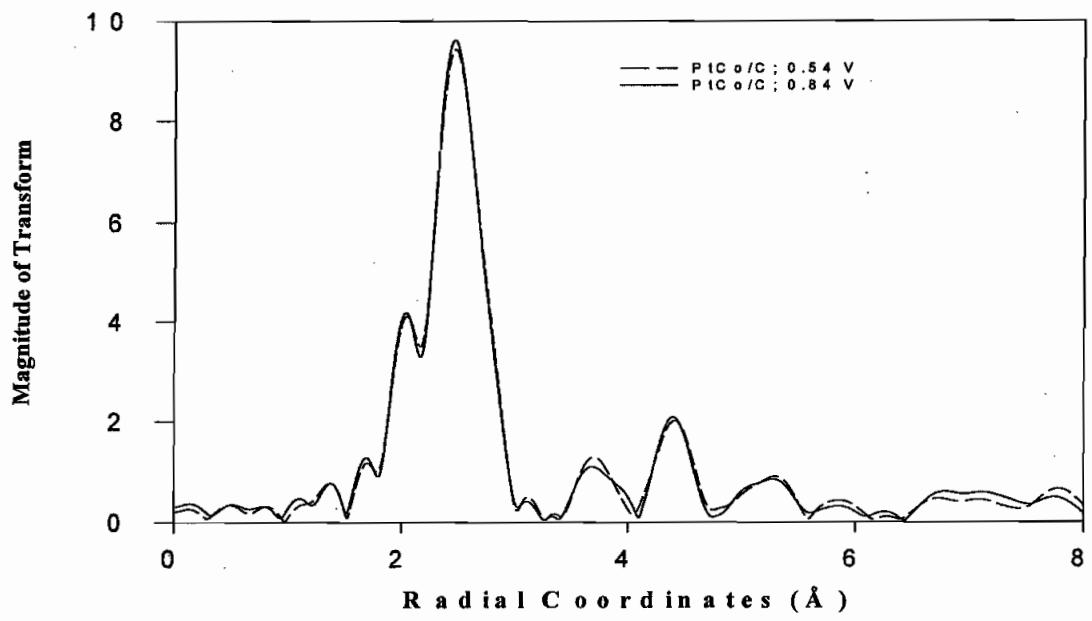
Figure 1b. Comparison of k^3 weighted Fourier transform at the Pt L_3 edge (r space) measured *in-situ* at 0.54 V and 0.84V vs. RHE for PtCo/C (Pt:Co::3:1) (Fourier filtering windows in Table 2).
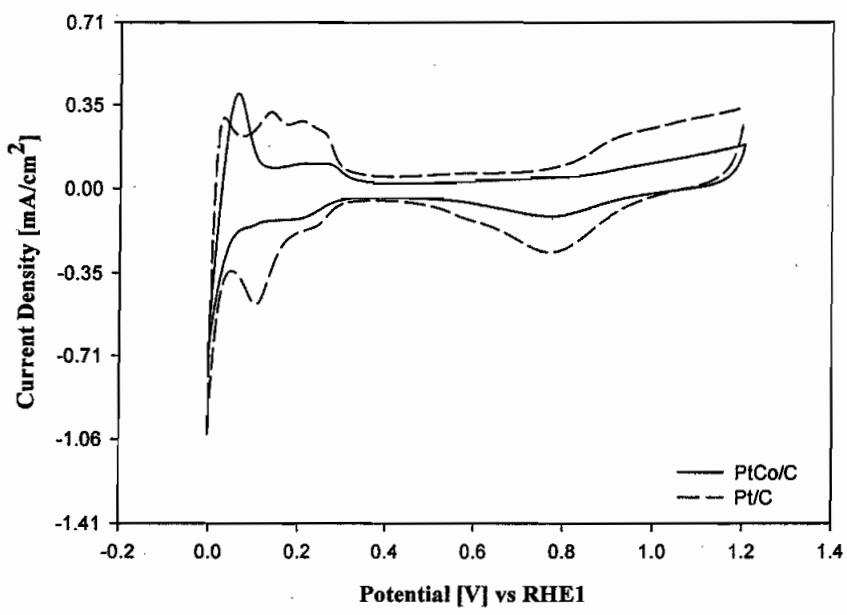
Figure 2a. Cyclic voltammograms in oxygen free 1 M CF$_3$SO$_3$H at room temperature for a 20%Pt/C (--) and a PtCo/C(–) on a glassy carbon (GC) disk electrode at 50 mV/sec. Current densities based on geometric electrode area.
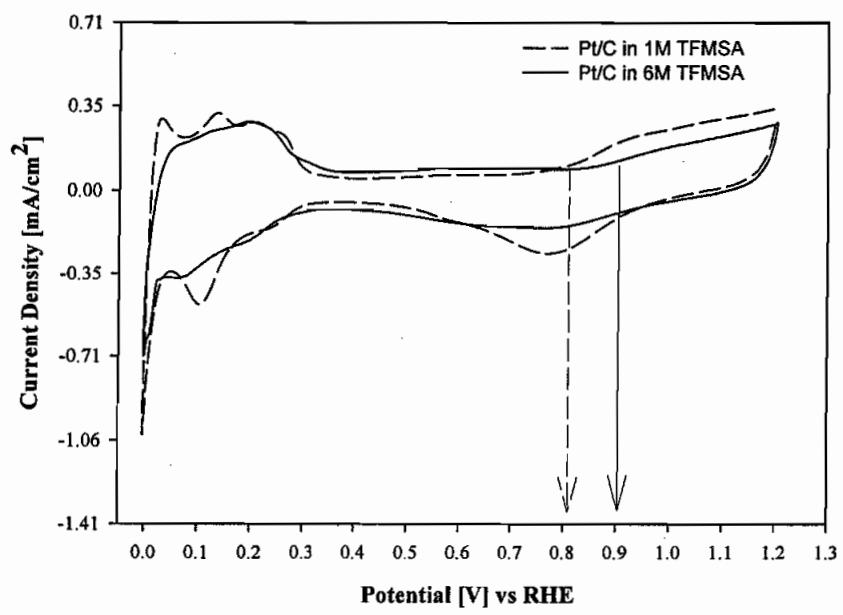
Figure 2b. Cyclic voltammograms for a 20%Pt/C in oxygen free 1 M (--) and 6 M (–) CF₃SO₃H at room temperature at 50 mV/sec vs. RHE1 and RHE6 reference electrodes respectively. Current densities based on geometric electrode area.
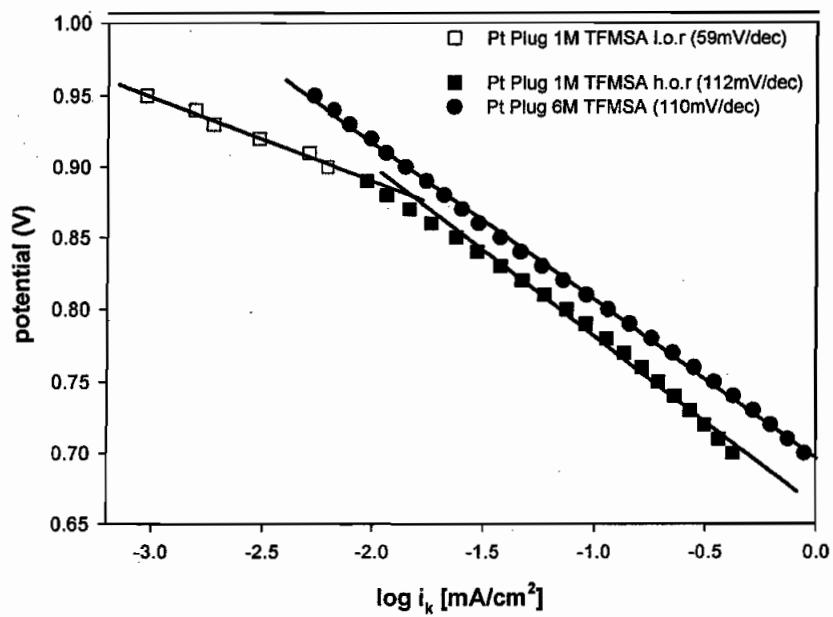
Figure 3. Tafel plots for ORR at room temperature on a polycrystalline (pc) Pt bulk electrode at 1225 rpm based on cathodic sweep from 1.2 V to 0.3V at 25mV/sec in 1 M and 6 M CF_3SO_3H.
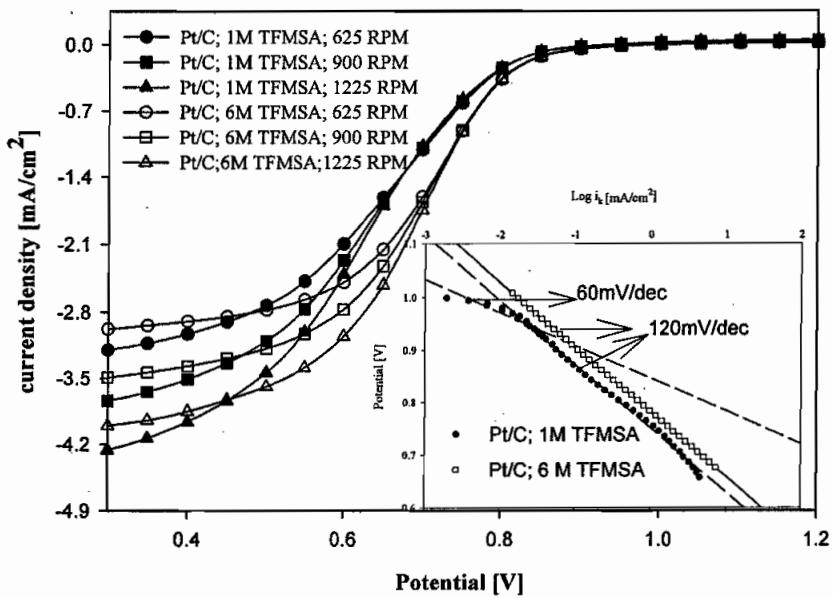
Figure 4. Disk currents obtained on the 20% Pt/C during ORR in the cathodic sweep at room temperature in 1 M and 6 M CF$_3$SO$_3$H at various rotation rates (625, 900 and 1225 rpm). Inset shows the Tafel plots for ORR at room temperature at 1225 rpm based on cathodic sweep from 1.2 V to 0.3V at 25mV/sec in 1 M and 6 M CF$_3$SO$_3$H.
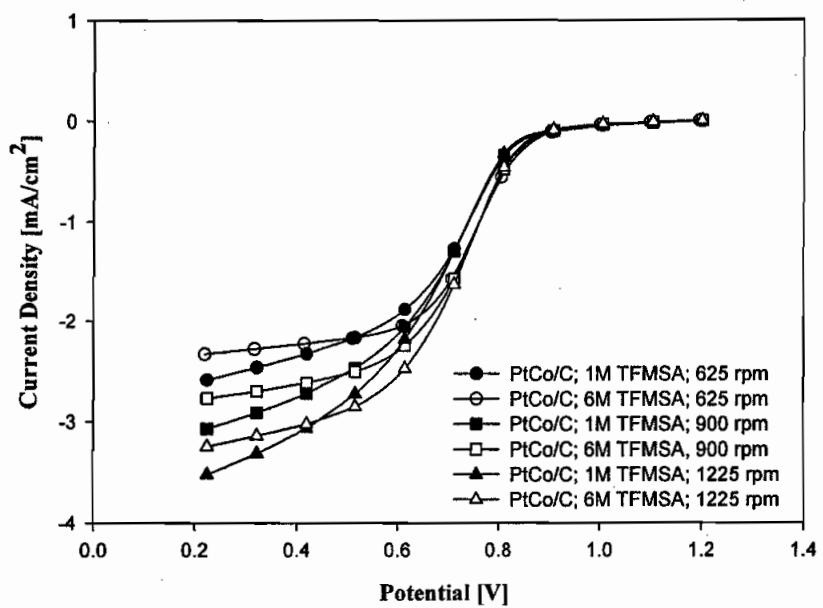
Figure 5. Disk currents obtained on the PtCo/C during ORR in the cathodic sweep at room temperature in 1 M and 6 M CF₃SO₃H at various rotation rates (625, 900 and 1225 rpm) measured at room temperature.
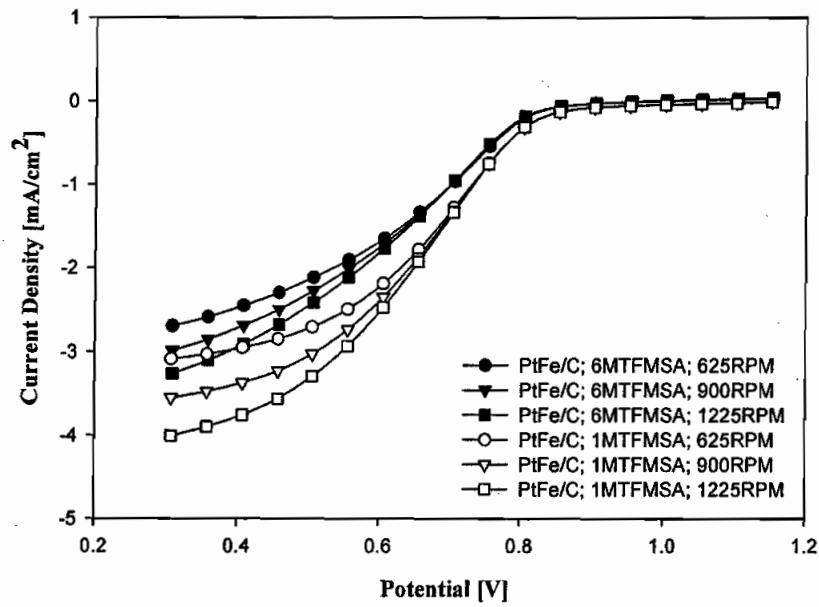
**Figure 6.** Disk currents obtained on the PtFe/C during ORR in the cathodic sweep at room temperature in 1 M and 6 M CF_3SO_3H at various rotation rates (625, 900 and 1225 rpm) measured at room temperature.
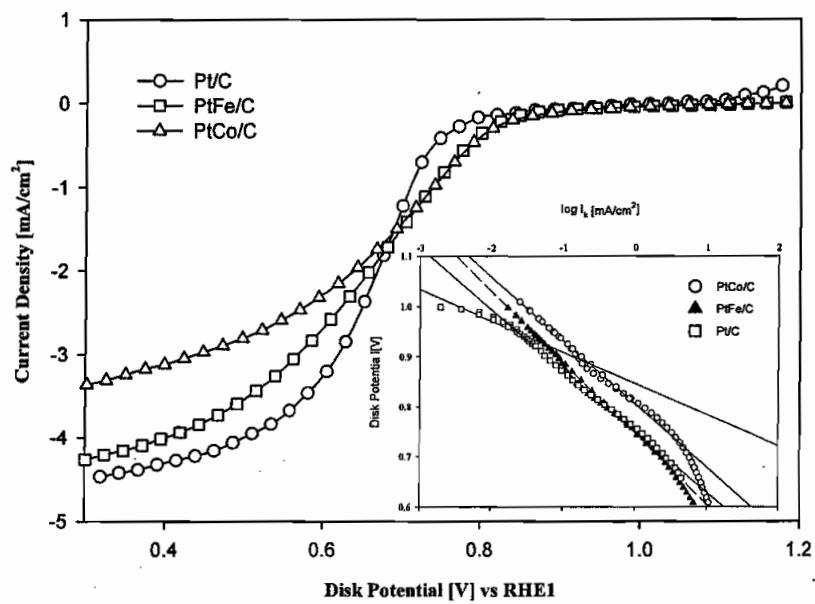
Figure 7. Disk currents obtained on Pt/C, PtCo/C and PtFe/C during ORR in the cathodic sweep at room temperature in 1 M CF₃SO₃H at 1225 rpm at 25 mV/sec at room temperature. Inset. Tafel plots for Pt/C (□), PtCo/C (○) and PtFe/C(▲); rotation rate, 1225rpm.
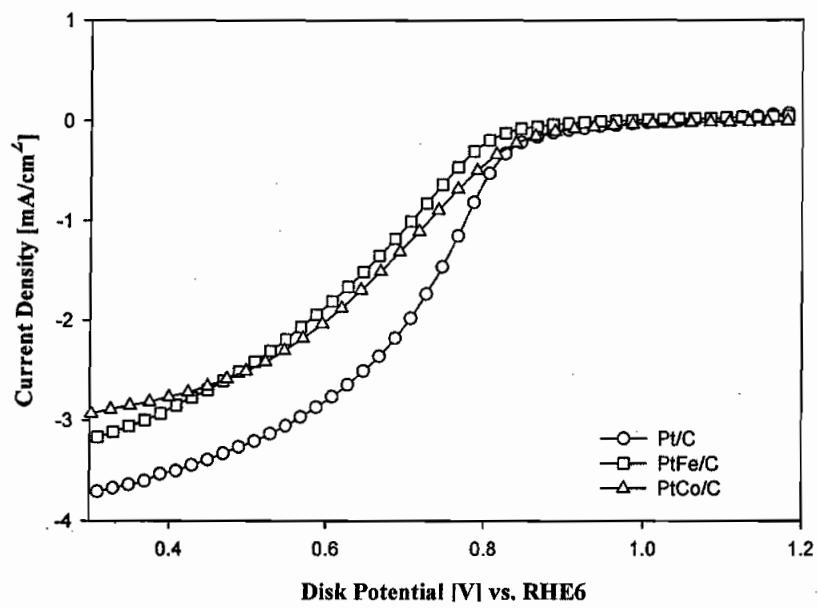
Figure 8. Disk currents obtained on Pt/C, PtCo/C and PtFe/C during ORR in the cathodic sweep at room temperature in 6 M CF₃SO₃H at 1225 rpm at 25 mV/sec at room temperature.

38
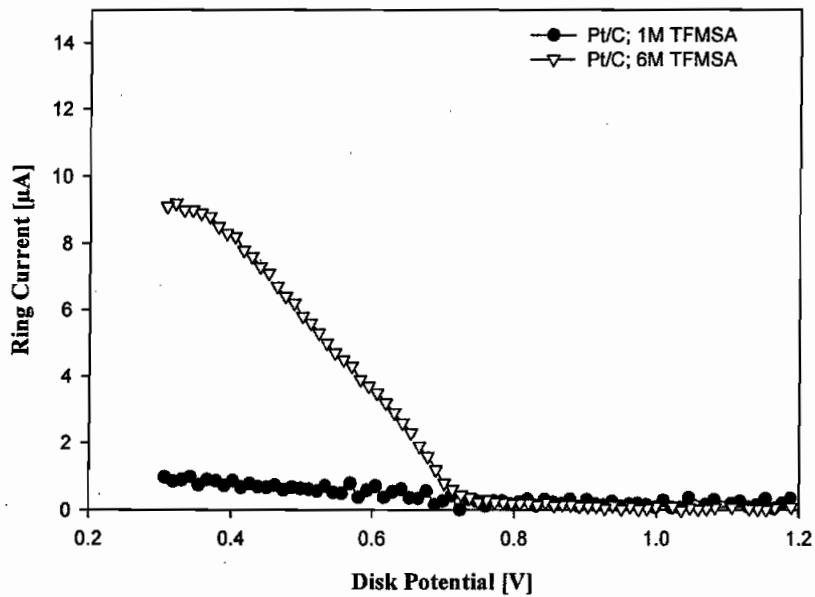
Figure 9a. Ring currents obtained on Pt/C during ORR in the cathodic sweep at room temperature in 1 M and 6 M CF$_3$SO$_3$H at 1225 rpm at room temperature.
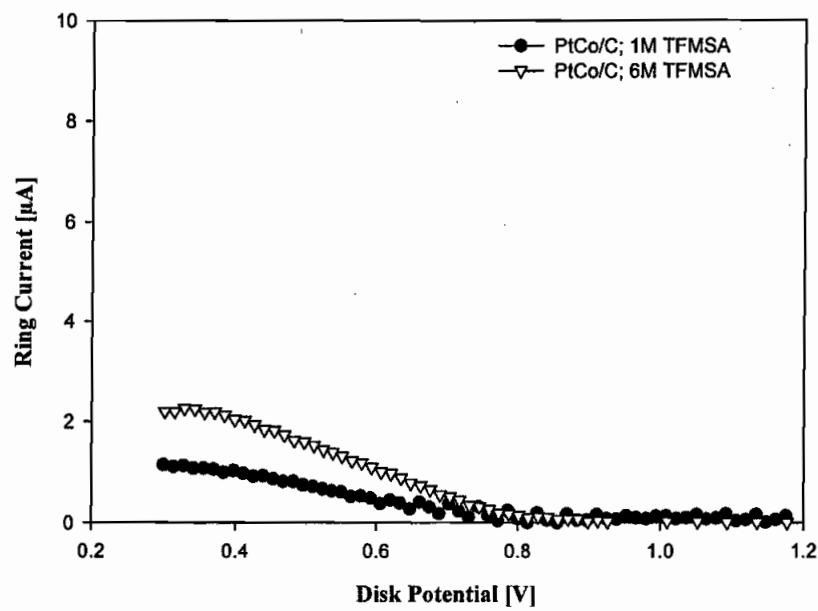
Figure 9b. Ring currents obtained on PtCo/C during ORR in the cathodic sweep at room temperature in 1 M and 6 M CF_3SO_3H at 1225 rpm in room temperature.
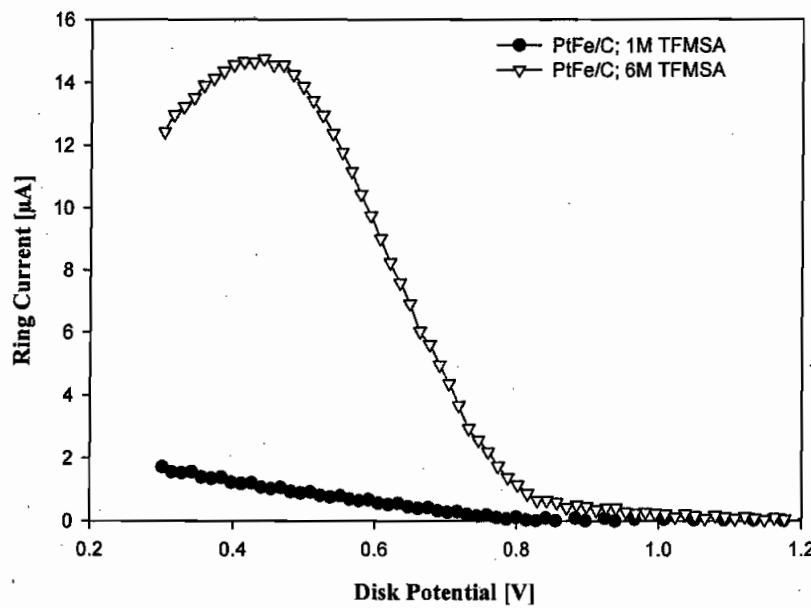
Figure 9c. Ring currents obtained on PtFe/C during ORR in the cathodic sweep at room temperature in 1 M and 6 M CF_3SO_3H at 1225 rpm in room temperature.

Table 1. Structural Characteristics of the Pt and Pt Alloy electrocatalyst using powder XRD data at 1.54 Å

Electrocatalyst	Lattice parameter	Pt-Pt Bond Distance (Å)	Average Particle Size (Å)
Pt/C	3.927	2.777	25
PtFe/C	3.866	2.733	39
PtCo/C	3.854	2.725	36

Table 2: Results of XANES (at Pt L and K edge of allying metal) and EXAFS analysis (at the Pt L$_3$ edge) for supported Pt and Pt alloy electrocatalysts. All data were measured *in-situ* at 0.54 V and 0.84 V vs. RHE.

Electrocatalyst	Atomic Ratio(a/o) XANES	Electrode Potential (0.54V vs. RHE)			Electrode Potential (0.84V vs. RHE)		
		$(h_j)_{t,s}$ Pt d-band vacancy	Pt-Pt (Å)	Pt-Pt (N)	$(h_j)_{t,s}$ Pt d-band vacancy	Pt-Pt (Å)	Pt-Pt (N)
Pt/C	-	0.329	2.77	8.7	0.370	2.77	6.8
PtFe/C	69/31	0.368	2.70	6.7	0.370	2.71	6.5
PtCo/C	72/28	0.401	2.68	6.9	0.390	2.68	7.6

The windows for the Fourier transform parameters used for EXAFS analysis of Pt L$_3$ edge at 0.54V are given as follows:
Pt/C: $k^n = 3$; Δk (Å^{-1}) = 3.49-14.23; Δr (Å) = 1.4-3.05. PtCo/C: $k^n = 3$; Δk (Å^{-1}) = 3.22-14.61; Δr (Å) = 1.5-3.5. PtFe/C: $k^n = 3$; Δk (Å^{-1}) = 3.45-17.14; Δr (Å) = 1.5-3.4.

Table 3: Mass transport parameters (diffusion coefficient and concentration) of oxygen in different electrolyte determined using Microelectrode Technique.

electrolyte	$C \times 10^6$ (mol/cm^3)	$D \times 10^6$ (cm^2/sec)	$DC \times 10^{12}$ $(mol. /cm$ $sec)$	$D^{2/3}C \times 10^{10}$ $(cm^2/sec)^{2/3} \times$ (mol/cm^3)	$v^a \times 10^2$ (cm^2/sec)
1 M CF$_3$SO$_3$H (25°C)	0.63	9.67	6.09	2.86	0.917
6 M CF$_3$SO$_3$H (25°C)	6.88	0.29	2.00	3.01	2.12
CF$_3$SO$_3$H[b] (25°C)	1.6	9.5	15.2	7.17	-
Nafion® 117 (30°C)	10.65	0.75	7.96	-	-
Nafion® 117[c] (30°C)	9.34	0.995	9.3	-	-
H$_2$SO$_4$[b] (25°C)	1.1	14	15.4	6.4	-
HClO$_4$[d]	1.18	19	22.42	8.4	0.893[e]

[a] Kinematic viscosity (viscosity/density)
[b] From Ref. [89] Concentration of acid given as pH = 0
[c] From Ref. [90]
[d,e] From Ref. [91] in low concentrated electrolytes

Table 4: Electrode kinetic parameters for the different electrocatalysts in 1 M and 6 M CF_3SO_3H (TFMSA) at room temperature from RRDE experiments at 1225 RPM.

Catalyst	conc. of TFMSA	I_k 0.9 V (mA/cm^2)	I_k 0.8 V (mA/cm^2)	- logI$_0$ (mA/cm^2)	Tafel slope (mV/dec)	Active Surface Area [a] [charge H$_{upd}$ region from CV in 1 M TFMSA] (cm^2)
pc-Pt plug	1 M	0.006	0.074	7.64/4.77	59/113	0.504
	6 M	0.014	0.114	4.85	110	
20%Pt/C	1 M	0.057	0.426	6.19/3.95	60/119	2.103
	6 M	0.122	0.607	3.65	123	
20%PtCo/C	1 M	0.106	0.413	3.39	140	1.177
	6 M	0.101	0.458	3.35	142	
20%PtFe/C	1 M	0.085	0.389	3.30	146	1.662
	6 M	0.033	0.245	4.40	113	

[a] based on 210μC/cm^2 for atomic hydrogen oxidation on a smooth Pt surface.

Table 5: Activation energies for oxygen reduction for the different electrocatalysts in 1 M CF$_3$SO$_3$H as a function of electrode potential.

Electrocatalyst	E$_a$* (0.85V) (kJ/mol)	E$_a$* (0.80V) (kJ/mol)	E$_a$* (0.75V) (kJ/mol)	E$_a$* (0.70V) (kJ/mol)
Pt/C	27.84 ± 2.04	26.87 ± 2.0	22.13 ± 1.7	19.12 ± 1.8
PtCo/C	27.86 ± 0.23	25.18 ± 0.78	22.33 ± 0.33	19.02 ± 0.78
PtFe/C	19.3	19.4	18.66	17.55

Table 6: Comparison of mole fraction of peroxide formed for the Pt and Pt alloy catalysts at 0.7 and 0.6 V from RRDE experiments at 1225 rpm, room temperature.

Catalyst	%H_2O_2, 1 M TFMSA [@0.7 V]	%H_2O_2, 6 M TFMSA [@0.7 V]
Pt/C	0.114	0.416
PtFe/C	0.147	2.387
PtCo/C	0.151	0.301

Table 7: Ring currents obtained at 0.7 V and 0.6 V during oxygen reduction reaction on Pt/C and PtM/C (M=Fe and Co) catalysts during cathodic sweep between 1.2 V – 0.3 V at Room Temperature.

Catalyst	conc. of TFMSA	$I_r[\mu A]$ 0.7 V	$I_r[\mu A]$ 0.6 V
Pt/C	1 M	0.27	0.49
	6 M	0.90	3.60
PtFe/C	1 M	0.33	0.67
	6 M	4.43	9.37
PtCo/C	1 M	0.30	0.53
	6 M	0.54	1.01

(II.2.) Tailored Nano-synthesis of Electrocatalysts using Micellar Method: Fundamental Investigation of the Skin Effect.

Abstract

Synthesis of carbon supported PtM/C catalysts (M = Co, Cr or Fe) using new preparation technique, reverse micelle method, is reported. The catalysts were characterized by different surface techniques, X-ray diffraction (XRD), scanning electron microscope (SEM), transmission electron microscope (TEM), and energy dispersive X-ray microanalysis (EDX). Surface characterization showed that Pt/M nanoparticles on catalysts were synthesized using reverse micelle method. Pt/M nanoparticles were observed to be uniform spherical objects. The performance of the PtM/C catalysts was tested by RDE technique. A trend of catalytic activity for oxygen reduction reaction (ORR) was obtained: PtCo/C(T, 500°C) ~ PtCo/C(S) > PtCr/C(S) > PtFe/C(S) ~ Pt/C > PtFe/C(T, 500°C) ~ PtCr/C(T, 500°C), showing that PtCo/C type catalysts had a higher catalytic activity for ORR.

Salient aspect of this part of the report is delineated below:

Recently, Sun reported synthesis of monodisperse iron-platinum (FePt) nanoparticles by reduction of platinum acetylacetonate and decomposition of iron pentacarbonyl in the presence of oleic acid and oleyl amine stabilizers[19,20]. Zhang obtained platinum-cobalt nanoparticles using a water-in-oil reverse microemulsion of water-Triton X-100-propan-2-ol-cyclohexane[21]. A well-dispersed Pt-Ru/C nanoparticles were synthesized using the surfacetants tetraalkylamonium bromide by Schmidt and Paulus[22,23]. The above-mentioned preparation methods of nanoparticles are called water-in-oil microemulsion media or reverse micelle (RM) method. In a reverse micelle the polar groups of the surfactants are concentrated in the interior and the lipophilic groups extend towards and into the nonpolar solvent. Reverse micelles consist of nanometer sized water droplets that are dispersed in an oil medium and stabilized by surfactants. These reverse micelle systems are heterogeneous on a molecular scale, nevertheless they are thermodynamically stable. Reverse micelle systems are suitable reaction media for the synthesis of nanoparticles, because tiny droplets of water are encapsulated into reverse micelles. Water pools of these reverse micelles act as micro-reactors for performing simple reactions of synthesis, and the size of micro-crystals of the product is determined by the size of these pools. The size of the water pools is known to be controlled by the molar water/surfactant ratio in the system. Varying the water/surfactant ratio can form different size micelles thus leading to careful control over the particle size. A co-surfactant is used to help decrease the fraction of the micelle head group that is neutralized and thereby increase the stability of the micelle. Without the addition of the co-surfactant, the amount of free water available to carry on the reactions is greatly reduced, as most of the water is locked in the head group of the surfactant[24]. Reverse micelle method is used to make perfect particle control over particle size and uniform be practicable. On the other hand, it does not require extremely high temperature and pressure conditions as well as any special equipment. Reverse micelle method is widely used in production of metallic nanoparticles, semiconductor materials and nanometer-scale magnetic particle[25-29]. Bonnemann has proved reverse micelle method is a good way to prepare nanometer-scale catalysts[25].

In this paper, we prepared the PtM (M = Co, Cr or Fe) nanoparticles using reverse micelle method, then deposited PtM nanoparticles on carbon (Ketjen Black) to obtain PtM/C catalysts. Two reaction procedures, simultaneous reduction and sequential reduction in reverse micelle methods, were used to observe if catalytic activity of oxygen reduction reaction were varied. Catalysts were characterized using XRD, TEM and SEM/DEX. Rotating disk electrode (RDE) was used to observe catalytic activity of oxygen reduction reaction.

Experimental Section

Synthesis of PtM Nanoparticle. All syntheses of carbon-supported PtM catalysts were carried out in argon atmosphere using a Schlenk technique. Sodium dioctyl sulfosuccinate

(AOT) was purchased from Fisher Scientific. Other all chemicals were obtained from Aldrich. Reverse micelle solutions consisted of an oil phase cyclohexane, surfactant AOT and co-surfactant 1-Butanol. An aqueous phase containing the reactants, H_2PtCl_6 and $CoCl_2$ ($Cr(NO_3)_3$ or $FeCl_3$) were used to form the reverse micelle. Another aqueous phase containing reducing agent $NaBH_4$ was also used to form another reverse micelle. The PtM nanoparticles were prepared by simultaneous reduction or sequential reduction procedure. Components of reverse micelle systems for the experiment are indicated in Table 1 and Table 2.

Simultaneous reaction procedure was a two-emulsion technique (Table 1). 9g AOT, 9g 1-Butanol, 27g cyclohexane, 4 ml 0.5M H_2PtCl_6 and 2.0 ml 1M $CoCl_2$ ($Cr(NO_3)_3$ or $FeCl_3$) solution were added in a 300 ml 3-neck flask reactor under Ar atmospheric condition stirring at room temperature for 30 minutes to form reverse micelle (I). The color of the solution is orange, reflecting the mixed color of the $PtCl_6^{2-}$ and Co^{2+} (Cr^{3+} or Fe^{3+}) ions. 9g AOT, 9g 1-Butanol, 27g cyclohexane and 10ml 2 M $NaBH_4$ were added in a flask (this solution is a colorless) under Ar atmospheric condition to form reverse micelle (II). The reverse micelle (II) was then transferred into reverse micelle (I). PtM nanoparticles were formed when H_2PtCl_6-$CoCl_2$ ($Cr(NO_3)_3$ or $FeCl_3$) solution and reducing solution $NaBH_4$ contacted each other. The color of the solution changed to dark from orange due to the suspended reduced metal nanoparticles. The reaction was allowed to mix for 2 h under Ar. Pure Pt nanoparticles were made by the same procedure without $CoCl_2$ ($Cr(NO_3)_3$ or $FeCl_3$) solution.

Sequential reaction procedure was a four-emulsion technique (Table 2). 5g AOT, 5g 1-Butanol, 15g cyclohexane, and 2.0 ml 1M $CoCl_2$ ($Cr(NO_3)_3$ or $FeCl_3$) solution in a 300 ml 3-neck flask under Ar atmospheric condition stirring at room temperature for 30 minutes to form reverse micelle (I). The color of the solutions is pink, violet or light orange, reflecting the colour of Co^{2+}, Cr^{3+} or Fe^{3+} ions, respectively. 5g AOT, 5g 1-Butanol, 15g cyclohexane and 3ml 2 M $NaBH_4$ in a flask (this solution is a colorless) under Ar atmospheric condition to form reverse micelle (II). The reverse micelle (II) was then transferred into reverse micelle (I). M nanoparticles were formed when $CoCl_2$ ($Cr(NO_3)_3$ or $FeCl_3$) solution and reducing solution $NaBH_4$ contacted each other. The color of the solution changed to gray from pink, violet or light orange due to the suspended reduced M nanoparticles. The reaction was allowed to mix for 30 minutes under Ar. 5g AOT, 5g (6.5 ml)1-Butanol, 15g (20ml) cyclohexane, and 0.5M H_2PtCl_6 (4.0 ml) solution are added a flask under Ar atmospheric condition stirring at room temperature for 30 minutes to form reverse micelle (III). The reverse micelle (III) was added into above 3-neck flask reactor under Ar atmospheric condition stirring at room temperature for 30 minutes. 5g AOT, 5g 1-Butanol, 15g cyclohexane and 6ml 2 M $NaBH_4$ in a flask (this solution is a colorless) under Ar atmospheric condition stirring at room temperature for 30 minutes to form reverse micelle (IV). The reverse micelle (IV) was transferred into the above reactor. Pt-coated M nanoparticles were formed when H_2PtCl_4 solution and reducing solution $NaBH_4$ contacted each other in the presence of the oil phase containing M nanoparticles. The color of the solution changed to dark from gray due to the suspended reduced Pt-coated M nanoparticles. The reaction was allowed to mix for 1.5 h under Ar.

Preparation of Carbon-Supported PtM Catalysts. The appropriate amount of carbon (Ketjen Black), dispersed in cyclohexane under ultrasonic wave agitation for 30 minutes, was added to the above micelle solution containing PtM nanoparticles under constant stirring over 8 h (or overnight). 50 ml Ethanol is then added to this mixture to break this reverse micelle, continue to stir 30 minutes; and get carbon supported precipitated. The precipitate was filtered using a sub-micron pore size filter (0.22 μm Millipore filter). After washing with 1:1 water and ethanol, cyclohexane and acetone, the product was dried at 120-140 °C under vacuum over 8 h (or overnight). Pure Pt/C was prepared by the same procedure but with only Pt nanoparticles. The content of the Pt metal was approximately 40 wt% in catalysts. Carbon-supported PtM/C catalysts were loaded into a silica tube, and heated in hydrogen gas at a ramp rate of 5 °C min^{-1} to the desired temperature (200 or 500°C) and held at this temperature for 1

hour, then pass argon for 1 hour and cool to room temperature. These catalysts are denoted as PtM/C(T,200°C), PtM/C(T,500°C), PtM/C(S,200°C), PtM/C(S,500°C), respectively. Table 3 shows all catalysts prepared by reverse micelle method.

Surface Characterisation. Powder X-ray diffraction (XRD) patterns of the catalysts were collected using a Philips X-ray diffractometer. The catalyst samples were held on an Al sample holder. An incident beam of X-rays of wavelength 1.5418 Å (CuK_α) filtered by a nickel filter was used. The samples were scanned from $10° < 2\theta < 90°$. The recorded patterns were matched against existing powder patterns using the JCPDS files. The average size of sample crystallite may be estimated by the Debye-Scherrer equation[30].

The morphologies of carbon and metal particles were obtained using a field emission scanning electron microscope (FE SEM, Hitachi S-4800 SEM) and transmission electron microscope (JEOL 2000fx). The composition analysis of catalysts was carried out using energy dispersive X-ray microanalysis (EDX). A small amount of Pt/C or PtM/C electrocatalyst sample was added to a glass ampoule containing 2-propanol and placed in an ultrasonic bath for approximately 10 minutes. A drop of the suspension was pipetted on a carbon coated copper grid (3 mm, 200 mesh) and the solvent was allowed to evaporate from the grid. The grid was then placed into the microscope. The elemental distribution of EDX spectrum was carried out using a computer program. The size of metal particles was measured by Photoshop 7.0 image software.

Rotating Disk Electrode (RDE). Rotating disk electrode experiments were carried out at room temperature using a Pine Instrument Analytical Rotator and Voltalab-10 system. The GC RDE (Pine Instrument) was polished with a 0.05 μm alumina suspension on a polishing cloth and then cleaned in distilled water for use as a support for the catalyst layer. The geometric surface area of the glassy carbon rotating disk electrode (GC RDE) is 0.196 cm^2 (diameter 5 mm). Perchloric acid (70%, analytical grade) was diluted with the distilled water to prepare 1 M $HClO_4$. A catalyst containing 5.448 mg Pt was added to 20 mL IPA and 80μl of 5 wt% Nafion and the mixture ultrasonically dispersed to get a catalyst ink. 15 μl of catalyst ink was pipetted onto the GC RDE surface to get a Pt loading of ~ 21 μg Pt/cm^2 and allowed to dry before starting RDE experiments.

The glass cell was cleaned by soaking in a 1:1 mixture of concentrated HNO_3 and H_2SO_4, followed by thorough rinsing with high-purity water. The counter electrode was a Pt wire and the reference electrode was a sealed reversible hydrogen electrode (RHE) made from the same concentration of the electrolyte used in the experiment. All potentials were referred to the RHE. Cyclic voltammograms for the catalyst layers were recorded in 1 M $HClO_4$ at room temperature. The potential was scanned between 0 and 1.2 V at a scan rate of 50 mV s^{-1}. Before recording, the potential was repeatedly scanned in the same range to remove residual impurities. Current-potential relations were measured in O_2 saturated 1 M $HClO_4$ at room temperature at various rotation speeds. The scan rate of the potential was fixed at 25 mV s^{-1}. The potential was finally stepped to 0.2 V and then swept in the positive direction from 0.2 to 1.2 V to obtain a current-potential relationship. The potential was also swept in the negative direction in the same range after stepping to 1.2 V.

Results and Discussions

Synthesis of Metal Nanoparticle: Sodium borohydride ($NaBH_4$) in aqueous solution has widely been exploited for the reductive production of transition metal powder. With the restriction that the surfactant, cosurfactant and oil phase should not react with the $NaBH_4$, all metal salts in aqueous phase can be reduced with $NaBH_4$ to metal powder (containing ca. 2-5% borides)[25]. For example, the reduction of H_2PtCl_6, or $CoCl_2$ with $NaBH_4$, Equation (1) and Equation (2) are given if borides were ignored:

$$H_2PtCl_6 + NaBH_4 + 4H_2O \rightarrow Pt\downarrow + NaB(OH)_4 + 6HCl + 2H_2\uparrow \quad (1)$$
$$2CoCl_2 + NaBH_4 + 4H_2O \rightarrow 2Co\downarrow + NaB(OH)_4 + 4HCl + 2H_2\uparrow \quad (2)$$
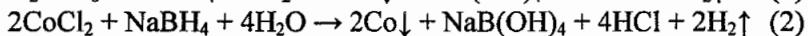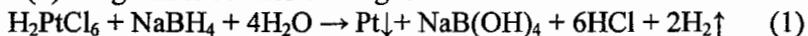
The nanometer-sized water pools of the reverse micelles and their narrow size distributions provide a stabilized environment for the production of platinum and metal (M) nanoparticles of fairly uniform size.

Surface Characterisation of Catalyst: XRD. Figure 1 shows the representative XRD powder patterns for Pt/C, PtCo/C(T, 500 °C), PtCr/C(T, 500 °C) and PtFe/C(T, 500 °C) type catalysts. Figure 2 shown powder-pattern lines for the three types of cubic lattices[31]. The faced-centered and body-centered cubic lattices show reflections from only certain planes whereas a simple cubic lattice gives observed reflections from all the planes[31]. The position and intensity of reference peaks from JCPDS files for Pt and carbon are shown in Table 4. The XRD data for all Pt/C and PtM/C catalysts are summarized in Table 5. Pt/C and the as-synthesized PtM/C (not shown in Figure 1) have chemically disordered fcc structure. The peak at $2\theta = 25°$ is corresponding to diffraction of Ketjen Black EC-300J Carbon[32]. The five major diffraction peaks of platinum for Pt/C catalyst are at $2\theta = 39.7°$ (111), 46.2° (200), 67.4° (220), 81.2° (311) and 87.3° (222)[33]. According to these peaks of platinum and lattice planes (111), (200), (220), (311) and (222), the type of lattice for Pt was face-centered cubic lattice (fcc lattice). So, the Pt-Pt distance, d_1, is $\dfrac{a}{\sqrt{2}}$ (a is Lattice parameter).

The main diffraction peaks shown in Table 5 for the as-synthesized PtM/C catalysts were shifted to higher angle compared with the diffraction peaks of Pt/C catalyst, suggesting that the unit cell dimension of platinum has been decreased by substitution of the smaller Co, Fe or Cr atom into the Pt lattice. This shift also suggests that the interatomic distance of Pt was decreased due to the substitution of a smaller atom, such as a transition metal, Co, Fe or Cr, other than platinum[17,34]. The XRD pattern of Pt/C and the as-synthesized PtM/C type catalysts could be fitted to a faced-centered cubic (fcc) phase[31]. The positions of main peaks of the as-synthesized PtM/C type catalysts indicate Pt_3Co, Pt_3Fe and Pt_3Cr alloy formation compared with those of Pt[35-37]. After heat treatment, XRD powder pattern for PtCo/C(T, 500 °C) and PtCr/C(T, 500 °C) type catalysts still show fcc structure.

XRD powder pattern for PtFe/C(T, 500 °C) and PtFe/C(S, 500 °C) type catalysts show that, according to the positions of these peaks for PtFe/C(T, 500 °C) and PtFe/C(S, 500 °C) type catalysts, the PtFe/C type catalysts heated at 550 °C match those of simple cubic lattice, or primitive tetragonal. According to Bragg law, $2d_{hkl}\sin\theta = \lambda$, and d-spacing formula $\dfrac{1}{d_{hkl}^2} = \dfrac{h^2}{a^2} + \dfrac{k^2}{b^2} + \dfrac{l^2}{c^2}$, Equation (3) will be obtained.

$$\frac{(2\sin\theta)^2}{\lambda^2} = \frac{h^2}{a^2} + \frac{k^2}{b^2} + \frac{l^2}{c^2} \qquad (3)$$

where $h, k\, l$ are lattice plane parameters; d_{hkl} is perpendicular distance between planes; a, b, c are lattice constants; λ is the X-ray wavelength (1.5406 Å) for CuK_α; θ is the Bragg angle; For tetragonal structure, $a = b$. Using (111), (200) planes and their 2θ, we can obtain a, b, c for PtFe/C(T, 500 °C) and PtFe/C(S, 500 °C) catalysts. Due to a, b, c being similar (shown in Table 5), the structures of PtFe/C(T, 500 °C) and PtFe/C(S, 500 °C) catalysts can be attributed to simple cubic lattice, or primitive tetragonal. Sun and Elkins[20,38] reported FePt nanoparticles prepared using chemical reduction method. XRD patterns shown in references[20,38] for the as-synthesized FePt particles and FePt annealed at 600 °C were similar with mine. They claimed that thermal annealing converts the internal particles structure from a chemically disordered face-centered cubic (fcc) phase to the chemically ordered face-centered tetragonal (fct) phase for FePt nanoparticles. We do not agree with their explanation. According to the positions of peaks in references[20,38], FePt annealed at 600 °C should be attributed primitive tetragonal. In addition, tetragonal system does not have face-centered tetragonal (fct) lattice type, only

52

primitive (P) and body centered (I) lattice types according to "The seven crystal systems and 14 Three-Dimensional Bravais Lattice Types"[39,40]. So, the shortest Pt-Pt distance for PtFe/C(T, 500 °C) and PtFe/C(S, 500 °C) catalysts, d_1, is c (c is Lattice parameter).

The peaks at $2\theta = 47.6°$ for cobalt, $2\theta = 44.7°$ for iron, and $2\theta = 44.4°$ for chromium were not found, suggesting that there was no evidence to indicate the presence of any crystalline metal M phase. There were also no peaks corresponding to any metal M oxide phases. This was probably because the metal M loading was low, and also any second metal M species present was highly dispersed or was amorphous and so could not be detected.

The average crystallite size for the Pt/C and PtM/C catalysts was determined from the peak width Pt(111) because it has the highest intensity value, and was calculated using the Debye-Scherrer equation [30]:

$$T = C \lambda / B \cos\theta \qquad (4)$$

where T is the diameter of the average particle size in Å; λ is the X-ray wavelength (1.5406 Å) for CuK_α; θ is the Bragg angle; C is a factor (typically from 0.9 to 1.0) depending on crystallite shape; B is the full width at half maximum, FWHM. For our experiment, C = 0.9; λ = 1.5406(Å). This equation shows an inverse relationship between crystallite size and peak profile width: the wider the peak, the smaller the crystallites.

The fourth column in Table 5 shows the crystalline size of PtM/C type catalysts. The size is increased as the temperature of heat treatment raised for all PtM/C catalysts. The crystallite sizes of the as-synthesized PtCo/C and PtFe/C catalysts was small, around 5 or 6 nm after reverse micelle and heat treatment at 200 °C. However, the crystallite sizes of the PtCo/C and PtFe/C catalysts became large (over 10 nm) after heat treatment at 500 °C, suggesting there is sintering at high temperature for the PtCo/C and PtFe/C catalysts type catalysts. The crystallite size of PtCr/C catalysts is larger than that of PtCo/C or PtFe/C catalysts after reverse micelle method although the preparation conditions for there three catalysts is same. Aqueous phase in reverse micelle is $Cr(NO_3)_3$ for PtCr/C catalyst, but $CoCl_2$ and $FeCl_3$ for PtCo/C and PtFe/C catalysts, respectively. So, we suggest that larger crystallite size of PtCr/C catalysts results from the use of $Cr(NO_3)_3$.

Assuming a spherical shape for the particles, the specific area S (m^2g^{-1}) for the crystallites was calculated using the following equation (5)[41]:

$$S = 6 \times 10^3 \rho^{-1} d^{-1} \qquad (5)$$

where d is the diameter of the particle (nm) obtained from the XRD and ρ is the platinum density (21.4 g cm^{-3}). The metal surface was listed in the fifth column of Table 5.

Electron Microscope and Energy Dispersive X-ray Microanalysis (EDX). Figure 3 shows scanning electron microscope (SEM) of Ketjen Black EC-300J Carbon, and representative as-synthesized PtM/C catalyst, PtCo/C(S). The aim of SEM is to observe supporter, carbon in catalysts. From these images, the spheres correspond to individual particles of Ketjen Black EC-300J carbon. The morphology is composed of integrated of these particles of size around 50 nm. Comparing the image of Ketjen Black EC-300J Carbon with that of as-synthesized PtCo/C(S) catalyst, it is obvious that carbon in as-synthesized PtCo/C(S) catalyst is the same as Ketjen Black EC-300J Carbon, suggesting that the structure and size of carbon are not changed and carbon is less aggregated during preparation processes of PtM/C catalysts. It means that reverse micelle process is mild process. The metal particles on carbon could not be seen due to the extremely small size and the technique limitation of SEM.

The size and shape of the metal particles of catalysts can be characterized using TEM technique. Representative TEM image and histogram of particle size distribution of the as-synthesized PtM/C prepared using reverse micelle method are shown in Figure 4 (a). Every metal nanoparticle is a spherical object. Figure 4 (b) shows TEM image and histogram of particle size distribution of PtCo/C catalyst, from UTC fuel cells, prepared using impregnation

53

method. Styles of metal particles in Figure 4 (b) are different each other. From Figure 4, the metal particles of the as-synthesized PtM/C prepared using reverse micelle method are more uniform and have a narrower particle size distribution than that of PtCo/C prepared using impregnation method, although there is some low degree of metal particle agglomeration to be observed on Ketjen Black EC-300J Carbon in Figure 4 (a). The low degree of metal particle agglomeration results from preparation process, which the metal nanoparticles were firstly synthesized during reverse micelle method, then deposited on Ketjen Black EC-300J Carbon. The metal particles of PtCo/C prepared using impregnation method appear to be well dispersed on Ketjen Black EC-300J Carbon. This is because the metal particles of the PtCo/C prepared using impregnation method were obtained by reducing metal salts and deposited on Ketjen Black EC-300J Carbon immediately. How the metal nanoparticles prepared using reverse micelle method homogeneously deposit on carbon is being studied. For example, Supporter, carbon, will be added in reverse micelle solution before (or while) reducing solution $NaBH_4$ is applied. TEM results suggests that reverse micelle method can control metal particle size and uniform is practicable.

To confirm the composition of the metal particles, energy dispersive X-ray microanalysis (EDX) spectra were collected during TEM and SEM experiment. EDX analysis of catalysts was performed by reducing the size of the beam and focusing on different areas of the catalysts. Two representative EDX spectra are shown in Figure 5. The catalysts were held on copper and Al sample holder for the EDX experiment, so the Cu peak at 8.047 eV and Al peak at 1.5 eV were also observed. On focusing the beam on areas of Ketjen Black EC-300J Carbon of the as-synthesized PtCo/C catalysts, no evidence for Platinum and Co metals were found on the carbon support (Figure 5 (a)). Focusing on random metal particle areas of the as-synthesized PtCo/C catalysts, EDX (Figure 5(b)) shows that the presence of both the Pt and Co metal was observed. The composition of all as-synthesized PtM/C catalysts was also measured by EDX. The results are listed in Table 3. The compositions given in Table 3 will not represent an accurate analysis of the catalysts due to the local nature of the sampling process; however, it shows that both the Pt and M were present on PtM/C catalysts.

Electrochemical Characterization of Catalysts: Cyclic Voltammetry. Figure 6 shows typical steady-state cyclic voltammograms of Pt/C and two of PtM/C catalysts prepared using reverse micelle method, PtCo/C(T) and PtCo/C(S) in Ar saturated 1 M $HClO_4$ at 50 mV/s with a Pt loading of ~ 21 μg Pt/cm^2. Scanning from 0 V to 1.2 V versus RHE is called the anodic scan; scanning from 1.2 V to 0 V versus RHE is called the cathodic scan. The hydrogen adsorption/desorption features on Pt/C and PtM/C catalysts between 0.4 and 0 V vs RHE are different with that of a bulk Pt electrode due to the fact that the carbon-supported Pt particles possess some degree of low coordinated crystal planes[42]. The comparison of cyclic voltammograms of Pt/C and PtCo/C(T) and PtCo/C(S) type catalysts in Figure 6 shows that the double layer thickness of the PtCo/C(T) or PtCo/C(S) type catalysts is lower than that of Pt/C catalyst due to Co addition, although all catalysts used Ketjen Black EC-300J Carbon as support. The onset of the anode oxygen chemisorption and oxide formation on platinum (Pt + $H_2O \rightarrow$ Pt-OH$^+$ +H$^+$ + 2e$^-$) for the PtCo/C(T) or PtCo/C(S) type catalysts is higher potential than that of Pt/C. For example, the onset of the anode oxygen chemisorption for PtCo/C(T) or PtCo/C(S) type catalysts takes place at around 0.85 V relative to 0.70 V of Pt/C catalyst. The difference of oxygen chemisorption and oxide formation of Pt between Pt/C and PtCo/C(T) or PtCo/C(S) type catalysts is attributed to transition metal, Co. The similar results were obtained for PtFe/C and PtCr/C type catalysts (not shown in Figure 6). The transition metals are believed to provide sites to bind and activate water[43,44]. This means that allying with transition metal effects some changes in the way Pt atoms of PtM/C catalysts interact with water. Thus, the shift in the onset of anode oxygen chemisorption and oxide formation on platinum on the cathodic sweep suggests that there was evidence of Pt/M alloy formation for PtM/C catalysts. Murthi et al.[42] observed a similar positive shift Pt/C in 6 M trifluoromethane sulfonic acid

54

(CH_3SO_3H) or PtCo/C in $1M$ CH_3SO_3H compared to Pt/C in 1 M CH_3SO_3H. They suggests the onset of oxide formation can be shifted by either alloying the Pt with second metal that increases the $5d$-band vacancies or by lowering the activity of water [42].

The charges of hydrogen adsorption at cathodic scan or oxidation of hydrogen at anodic scan were calculated from integration of the hydrogen adsorption or oxidation of hydrogen peaks. These charges can be used to calculated the actual area of the surface Pt in meters squared per gram if the platinum loading on GC RDE surface is known, assuming a correlation value of 210 $\mu C/cm^2$ [43]. For hydrogen adsorption (Pt + H^+ + $e^- \rightarrow$ Pt-H_{ads}) or oxidation of hydrogen (Pt-$H_{ads} \rightarrow$ Pt + H^+ + e^-), we assume that one electron is passed per platinum site, and therefore, the Pt electrochemical area (ECA) can be calculated by

ECA ($m^2 g^{-1}$ Pt) = hydrogen charge (μC)/ (210 ($\mu C/cm^2$)×Pt loading (g))×10^{-4}

The electrochemical surface area (ECA) of Pt/C, and all the PtM/C type catalysts are tabulated in Table 6. It can be seen that the PtM/C catalysts had a lower Pt surface area than the monometallic Pt/C catalyst in all cases. This was expected as some Pt surface atoms are covered by Fe, Co or Cr atoms. ECA of the PtM/C catalysts decreased in each type as the heat treatment temperature increased. These results suggest that Pt surface area was decreased under high temperature, due to some agglomeration. The results are agreement with that of XRD (in the fifth column of Table 5).

Evaluation of Catalytic activity using RDE Technique. Figure 7 shows a representative rotating disk electrode data, current density vs. potential curves for different rotation rate, obtained on PtCo/C(T, 500 °C) type catalyst preparing using reverse micelle method. This Figure shows a single steep oxygen reduction reaction (ORR) was observed over around 0.65 V, and mixed kinetic-diffusion control, diffusion-limited currents were recorded between 0.2 and around 0.6 V. Limiting current density, j_d, was obtained at each rotation rate. Similar results were also obtained for other PtM/C catalysts preparing using reverse micelle method (not shown here).

The electrode was prepared by mixing catalyst with Nafion (only as a binder). The electrode film deposited on the glassy carbon rotating disk electrode (GC RDE) such that the Pt or Pt/M exposed in the surface are sufficient for neglecting any important diffusion resistance contribution of the catalyst layer. As described in publications[45,46] the resistance of the Nafion film which covers the supported catalysts is sufficiently small. Therefore, the kinetic current densities can generally be adjusted to the simple Koutecky-Levich first order reaction equation, without further need of additional terms[47]:

$$\frac{1}{j} = \frac{1}{j_k} + \frac{1}{j_d} = \frac{1}{j_k} + \frac{1}{B\omega^{1/2}} \qquad (6)$$

where j_k is the kinetic current density, j_d is diffusion limited current density. ω is the angular frequency of rotation. $\omega = 2\pi f/60$. f is RDE rotation rate in rpm. The B parameter is defined as[47,48]:

$$B = 0.620nFD^{2/3}v^{-1/6}C_O \qquad (7)$$

Figure 8 shows j^{-1} versus $\omega^{-1/2}$ plots (Koutecky-Levich plots) for oxygen reduction at Pt/C and PtCo/C(T) type catalysts. Calculation was performed for n, number of exchanged electron, using the slope of the plot and the values[49,50]: F is the Faraday constant (96485 C mol^{-1}), D is the diffusion coefficient of the molecular O_2 in 1 M $HClO_4$ solution ($1.9×10^{-5}$ cm^2 s^{-1}), v is the kinematic viscosity ($9.87×10^{-3}$ cm^2 s^{-1}), C_O is the concentration of molecular oxygen ($1.6×10^{-6}$ mol cm^{-3}). Table 7 lists the number of exchanged electron for Pt/C and PtCo/C(T) type catalysts. In diffusion control range, straight lines are obtained. The number of exchanged electron, n, is 4.2 for Pt/C. The result with n ≈ 4 for Pt/C suggests that the oxygen reduction proceeds by an overall four electron transfer process on Pt/C catalyst. The value of n for PtCo/C(T) was smaller than that on Pt/C. Coutanceau et al.[51] reported oxygen reduction at Pt nano-particles in a polyaniline film supported on a GC RDE immersed in O_2-saturated 0.5 M

55

H_2SO_4. They observed that the value of n for low platinum loading and high platinum loading was three and four, respectively. In low platinum loading case as much as of hydrogen peroxide as water is formed by the oxygen reduction reaction. Considering the mechanism of O_2 reduction[52], the reduction of n from 4 can occur when part of H_2O_2 generated in the 2-electron reduction in the series pathway without further reduction to H_2O. Due to the fact that the transition metals are believed to provide sites to bind and activate water[43,44], Part of H_2O generated under oxygen reduction was not transferred to the outside of PtCo/C(T) catalyst. This would lead part of H_2O_2, intermediate product of oxygen reduction, not to further reduce to H_2O. Thus, the smaller n observed for oxygen reduction at PtCo/C(T) catalyst. After heat treatment of PtCo/C(T) at different temperature, PtCo/C(T, 200°C) and PtCo/C(T, 500°C) catalysts were obtained. The Co in PtCo/C(T, 200°C) and PtCo/C(T, 500°C) catalysts contacted Pt much closer than that in PtCo/C(T) catalyst or even entered in the structure of Pt, so the ability of adsorbing H_2O for the Co in PtCo/C(T, 200°C) and PtCo/C(T, 500°C) catalysts is very low. The larger n observed for oxygen reduction on PtCo/C(T, 200°C) and PtCo/C(T, 500°C) than on PtCo/C(T) was therefore caused by further reduction of H_2O_2 to H_2O. As the heat treatment temperature was increased, the number of exchanged electron, n, was found to increase.

Mass transport corrected Tafel plots of j_k for oxygen reduction are shown in Figure 9 for Pt/C, PtCo/C(S) type and PtCo/C(T) type catalysts at 1200 rpm. Tafel plots (E vs. $\log|j_k|$) can be directly extracted from experimental data and Equation (8):

$$j_k = \frac{j_d \times j}{j_d - j} \qquad (8)$$

Schmidt and Mailard recently used a thin-film RDE or porous RDE method to investigate the catalytic activity of carbon-supported Pt catalysts for oxygen reduction reaction towards fuel cell reactions[22,46,53]. In the thin-film RDE or porous method, a glassy carbon disk is successively covered by two layers, namely an inner layer of catalyst and an outer layer of Nafion. It means that O_2 coming from the solution first diffuse through a Nafion film and then reacts at the catalyst surface. This situation of the thin-film or porous RDE is very similar with that of the so called "thin-film model" of fuel cell electrodes. Thus, in my work, j_k can be considered as an indicator of catalytic activity. As heat treatment increased from Figure 9, the increase in - j_k for PtCo/C (T) type catalyst and decrease in $-j_k$ for PtCo/C(S) type was observed. Heat treatment is not useful for simultaneous reaction procedure of reverse micelle method, suggesting that Pt atom and Co atom have contacted closely for the as-synthesized PtCo/C(S) catalyst. It is important for sequential reaction procedure of reverse micelle method to heat as-synthesized PtCo/C(T) probably because Pt was coated on Co surface after the formation of Co nanoparticles. In order to form Pt/Co alloy or make Pt and Co contact closely, heat treatment is needed for the as-synthesized PtCo/C(T) type catalyst. The same result was also obtained for PtFe/C and PtCr/C catalysts (not shown in Figure 9). So, The order of catalytic activity for ORR was: PtM/C(T, 500°C) > PtM/C(T, 200°C) > PtM/C(T) using sequential reaction procedure of reverse micelle method; and PtM/C(S) > PtM/C(S, 200°C) > PtM/C(S, 500°C) using sequential reaction procedure of reverse micelle method.

To compare catalytic activity for oxygen reduction on different type catalysts, Figure 10 shows RDE results at 1200 rpm for the PtM/C(T, 500°C) and PtM/C(S) type catalysts and Figure 11 shows their mass transport corrected Tafel plots of j_k compared with Pt/C catalyst at 1200 rpm. Table 6 shows the kinetic data for all PtM/C catalysts. It is obvious that PtCo/C catalyst has best activity for oxygen reduction. From Figure 11, even though it is clear that the Tafel slope for the oxygen reduction reaction (ORR) is changing continuously in the potential range examined[54,55], two Tafel regions at low and high overpotential were found for Pt/C and PtM/C(S) catalysts. The Tafel slopes for Pt/C and PtM/C(S) catalysts were well defined around RT/F (~60 mV/decade) for the low overpotential range (E>0.85 V) and 2RT/F(~120

mV/decade) for the high overpotential range (E<0.80 V), although some are slightly different. They are in good agreement with Tafel slopes reported in the literature for single crystal Pt electrodes[56], polycrystalline Pt[57], carbon supported Pt catalysts[58]. The appearance of two linear segments in the Tafel plot has typically been reported for the O_2 reduction reaction on platinum electrode in acidic medium and at the platinum/Nafion interface. Variations in the Tafel slopes are attributed to the influence of different adsorption and different rate-determining steps over the potential ranges investigated[56-58]. However, a single Tafel slope of ~120 mV/decade was observed for PtM/C(T, 500°C) catalysts in the entire mixed activation-diffusion region which is indicative of total Pt/M alloy formation for PtM/C(T, 500°C) catalysts[42]. Comparing the seven catalysts in Figure 11, the trend of catalytic activity for oxygen reduction reaction is: PtCo/C(T, 500°C) ~ PtCo/C(S) > PtCr/C(S) > PtFe/C(S) ~ Pt/C > PtFe/C(T, 500°C) ~ PtCr/C(T, 500°C). The trend implies that catalytic activity of ORR is not only dependent on Pt alloying with transition metals. Many factors affect the catalytic activity of ORR. For example, catalyst preparation method, reaction conditions and choice of transition metal for certain preparation method, the size of metal particle, the relation between platinum and other metals.

Conclusions

We have reported that synthesis of PtM nanoparticles by reducing H_2PtCl_6 and M salts (M = Co, Cr or Fe) in reverse micelle system and preparation of PtM/C catalysts by depositing PtM nanoparticles on carbon (on Ketjen Black EC-300J). PtM/C catalysts were characterized by different surface techniques. The results showed that PtM particles on PtM/C catalysts prepared using reverse micelle method were nano-scale, more uniform and had a narrower particle size distribution than that prepared using impregnation method. Catalytic activities for oxygen reduction reaction on PtM/C catalysts were evaluated by RDE technique. The results indicated that PtCo/C(T, 500°C) and PtCo/C(S) catalysts possesses better catalytic activity for oxygen reduction reaction than Pt/C and other Pt bimetallic catalysts in our reverse micelle system. The result of the trend of catalytic activity for oxygen reduction reaction (PtCo/C(T, 500°C) ~ PtCo/C(S) > PtCr/C(S) > PtFe/C(S) ~ Pt/C > PtFe/C(T, 500°C) ~ PtCr/C(T, 500°C)) suggested that heat treatment was needed for catalyst preparation using sequential reduction procedure and high temperature was not good for catalyst preparation using simultaneous reduction in our reverse micelle method. All above mentioned results implied that many factors influenced catalytic activity of oxygen reduction reaction, including Pt alloying with transition metals, choice of transition metal for certain preparation method, and catalyst preparation conditions.

Catalyst		PtCo/C	PtCr/C	PtFe/C
Reverse micelle (I)	Aqueous phase	0.5M H_2PtCl_6(4.0ml) 1.0M $CoCl_2$ (2.0 ml)	0.5M H_2PtCl_6 (4.0ml) 1.0M $Cr(NO_3)_3$(2.0ml)	0.5M H_2PtCl_6 (4.0ml) 1.0M $Cr(NO_3)_3$(2.0ml)
	Surfactant	AOT, 9g	AOT, 9g	AOT, 9g
	Cosurfactant	1-Butanol, 9g	1-Butanol, 9g	1-Butanol, 9g
	Oil phase	Cyclohexane, 27g	Cyclohexane, 27g	Cyclohexane, 27g
Reverse micelle (II)	Aqueous phase	2.0 M $NaBH_4$ 10ml	2.0 M $NaBH_4$ 10ml	2.0 M $NaBH_4$ 10ml
	Surfactant	AOT, 9g	AOT, 9g	AOT, 9g
	Cosurfactant	1-Butanol, 9g	1-Butanol, 9g	1-Butanol, 9g
	Oil phase	Cyclohexane, 27g	Cyclohexane, 27g	Cyclohexane, 27g

Table 1. Components of reverse micelle systems in simultaneous reaction procedure

Catalyst		PtCo/C	PtCr/C	PtFe/C
Reverse micelle (I)	Aqueous phase	1.0M CoCl$_2$ (2.0 ml)	1.0M Cr(NO$_3$)$_3$ (2.0ml)	1.0 M (FeCl$_3$) (2.0ml)
	Surfactant	AOT, 5g	AOT, 5g	AOT, 5g
	Cosurfactant	1-Butanol, 5g	1-Butanol, 5g	1-Butanol, 5g
	Oil phase	Cyclohexane, 15g	Cyclohexane, 15g	Cyclohexane, 15g
Reverse micelle (II)	Aqueous phase	2.0 M NaBH$_4$ (3.0 ml)	2.0 M NaBH$_4$ (4.0 ml)	2.0 M NaBH$_4$ (4.0 ml)
	Surfactant	AOT, 5g	AOT, 5g	AOT, 5g
	Cosurfactant	1-Butanol, 5g	1-Butanol, 5g	1-Butanol, 5g
	Oil phase	Cyclohexane, 15g	Cyclohexane, 15g	Cyclohexane, 15g
Reverse micelle (III)	Aqueous phase	0.5M H$_2$PtCl$_6$ (4.0 ml)	0.5M H$_2$PtCl$_6$ (4.0 ml)	0.5M H$_2$PtCl$_6$ (4.0 ml)
	Surfactant	AOT, 5g	AOT, 5g	AOT, 5g
	Cosurfactant	1-Butanol, 5g	1-Butanol, 5g	1-Butanol, 5g
	Oil phase	Cyclohexane, 15g	Cyclohexane, 15g	Cyclohexane, 15g
Reverse micelle (IV)	Aqueous phase	2.0 M NaBH$_4$ (6.0 ml)	2.0 M NaBH$_4$ (6.0ml)	2.0 M NaBH$_4$ (6.0ml)
	Surfactant	AOT, 5g	AOT, 5g	AOT, 5g
	Cosurfactant	1-Butanol, 5g	1-Butanol, 5g	1-Butanol, 5g
	Oil phase	Cyclohexane, 15g	Cyclohexane, 15g	Cyclohexane, 15g

Table 2 Components of reverse micelle systems in sequential reaction procedure

Catalyst	Preparation Methods	Pt Wt%	Pt:M (atomic)
Pt/C	Simultaneous reaction procedure	44%	---
PtCo/C(S)	Simultaneous reaction procedure	37%	64:36
PtCo/C(T)	Sequential reaction procedure	40%	61:39
PtCr/C(S)	Simultaneous reaction procedure	42%	90:10
PtCr/C(T)	Sequential reaction procedure	38%	74: 26
PtFe/C(S)	Simultaneous reaction procedure	42%	85:15
PtFe/C(T)	Sequential reaction procedure	37%	24:76

Table 3 Catalysts prepared using reverse micelle

2θ	Intensity	Analysis	materials
25.0	100	Carbon	Carbon[32]
39.7	100	Pt(111)	Pt/C[37]
46.2	53	Pt(200)	Pt/C [37]
67.4	31	Pt(220)	Pt/C [37]
81.2	33	Pt(311)	Pt/C [37]

Table 4. XRD reference peaks from JCPDS files.

Catalyst	Lattice types	2θ	Crystallite Size (nm)*	Metal area /($m^2\,g^{-1}$)	Lattice parameter (Å)	Pt-Pt bond distance (Å)
Pt/C (JCPDS)		39.75			3.92	2.78
Pt/C	fcc	39.75	5.7	50	3.92	2.78
PtCo/C(S)	fcc	40.07	6.6	42	3.89	2.75
PtCo/C(S, 200 °C)	fcc	40.25	6.5	43	3.87	2.74
PtCo/C(S, 500 °C)	fcc	40.36	10.6	26	3.87	2.74
PtCo/C(T)	fcc	40.29	5.3	53	3.87	2.74
PtCo/C(T, 200 °C)	fcc	40.33	5.6	50	3.87	2.74
PtCo/C(T, 500 °C)	fcc	40.22	10.5	27	3.88	2.75
PtCr/C(S)	fcc	40.00	10.2	28	3.90	2.76
PtCr/C(S, 200 °C)	fcc	40.03	10.4	27	3.90	2.76
PtCr/C(S, 500 °C)	fcc	40.06	13.2	21	3.89	2.75
PtCr/C(T)	fcc	39.97	8.4	34	3.90	2.76
PtCr/C(T, 200 °C)	fcc	39.98	9.6	30	3.90	2.76
PtCr/C(T, 500 °C)	fcc	40.17	10.5	27	3.88	2.75
PtFe/C(S)	fcc	40.05	4.5	63	3.89	2.75
PtFe/C(S, 200 °C)	fcc	40.09	6.5	44	3.89	2.75
PtFe/C(S, 500 °C)	simple cubic or tetragonal	40.41	12.0	24	a=b=3.88; c=3.86	3.86
PtFe/C(T)	fcc	39.99	5.2	55	3.90	2.76
PtFe/C(T, 200 °C)	fcc	40.00	6.3	45	3.90	2.76
PtFe/C(T, 500 °C)	simple cubic or tetragonal	40.29	12.1	24	a=b=3.87; c=3.86	3.86

*: Estimated from the FWHM using the Debye-Scherrer equation.

Table 5. XRD data of Pt/C and PtM/C catalysts

Catalysts	ECA, m^2/g	j_k at 0.9V (mA/cm^2)	j_k at 0.85V (mA/cm^2)	j_k at 0.8V (mA/cm^2)	Tafel slope
Pt/C	62	0.019	0.062	0.227	143/77
PtCo/C(T)	52	0.029	0.138	0.536	139/72
PtCo/C(T,200 ^{o}C)	45	0.038	0.183	0.998	131/70
PtCo/C(T,500 ^{o}C)	25	0.116	0.319	0.986	119
PtCo/C(S)	56	0.067	0.376	1.442	147/78
PtCo/C(S,200 ^{o}C)	30	0.050	0.267	1.133	145/71
PtCo/C(S,500 ^{o}C)	30	0.024	0.100	0.471	129/68
PtCr/C(T,500 ^{o}C)	27	___	0.019	0.0622	117
PtCr/C(S)	47	0.036	0.146	0.615	129/67
PtFe/C(T,500 ^{o}C)	37	___	0.022	0.0567	116
PtFe/C(S)	55	0.023	0.0776	0.2545	147/77

Table 6. Electrode Kinetic Parameters for Different Catalysts in 1 M $HClO_4$ at room temperature. Scan rate: 25 mV s^{-1}, rotation rate: 1200 rpm

Catalyst	n
Pt/C	4.2
PtCo/C(T)	2.7
PtCo/C(T,200°C)	3.4
PtCo/C(T,500°C)	4.2

Table 7. The number of exchanged electron in oxygen reduction
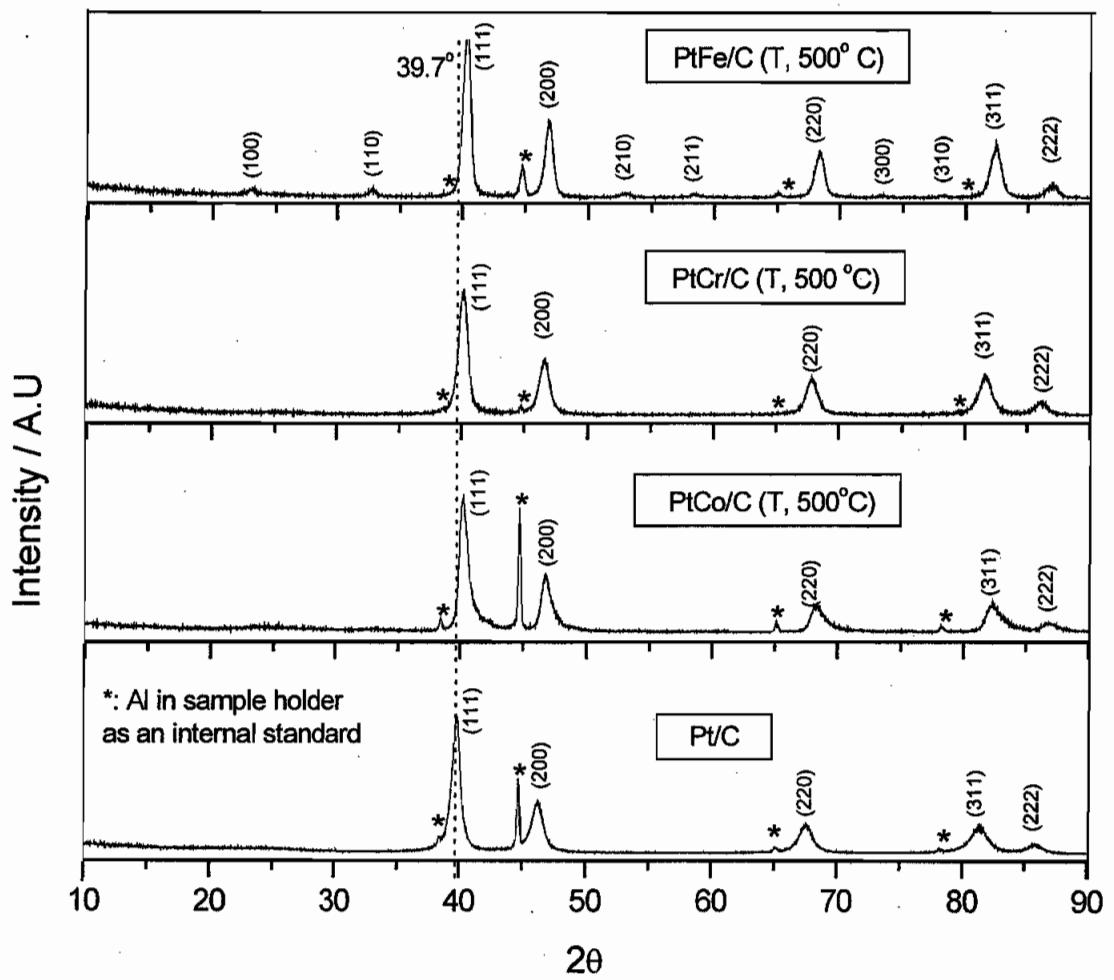
Figure 1. XRD pattern for Pt/C and PtM/C type catalysts

	(100)	(110)	(111)	(200)	(210)	(211)		(220)	(300) (221)	(310)	(311)	(222)
	1	2	3	4	5	6	7	8	9	10	11	12
a.												
b.												
c.												

Figure 2. Powder-pattern lines expected for the three types of cubic lattices (a) Simple cubic lattice, (b) Body-centered cubic lattice and (c) Face-centered cubic lattice
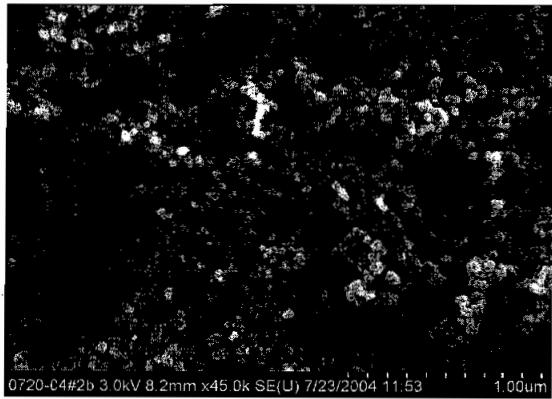
a   b

Figure 3. SEM microphotograph of (a) Ketjen Black Carbon and (b) PtCo/C(S) Catalyst

(a)   (b)
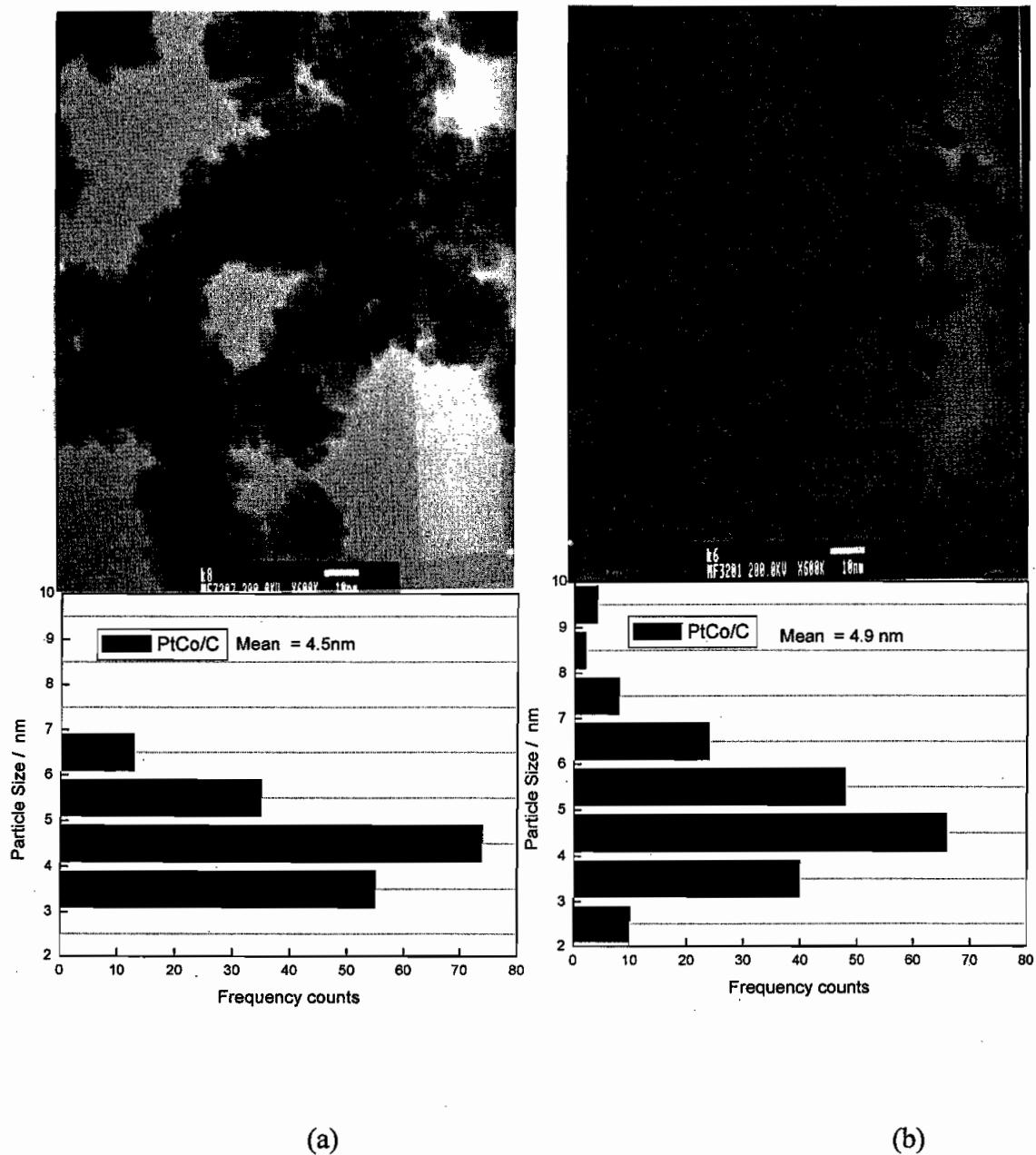
Figure 4.   Representative electron micrographs and particle size distribution of

PtCo/C catalysts (a) reverse micelle method, and (b) impregnation method (the bar is

10 nm).
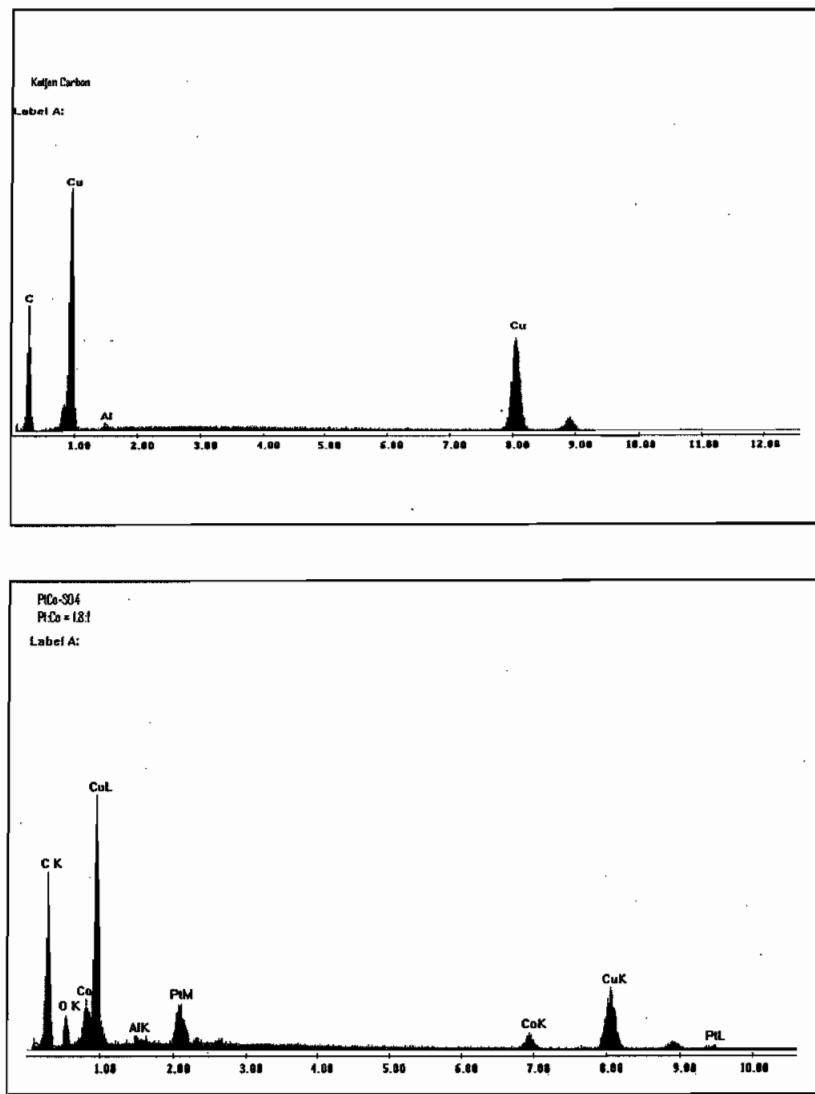
Figure 5 EDX results for Pt/C and PtCo/C Catalysts
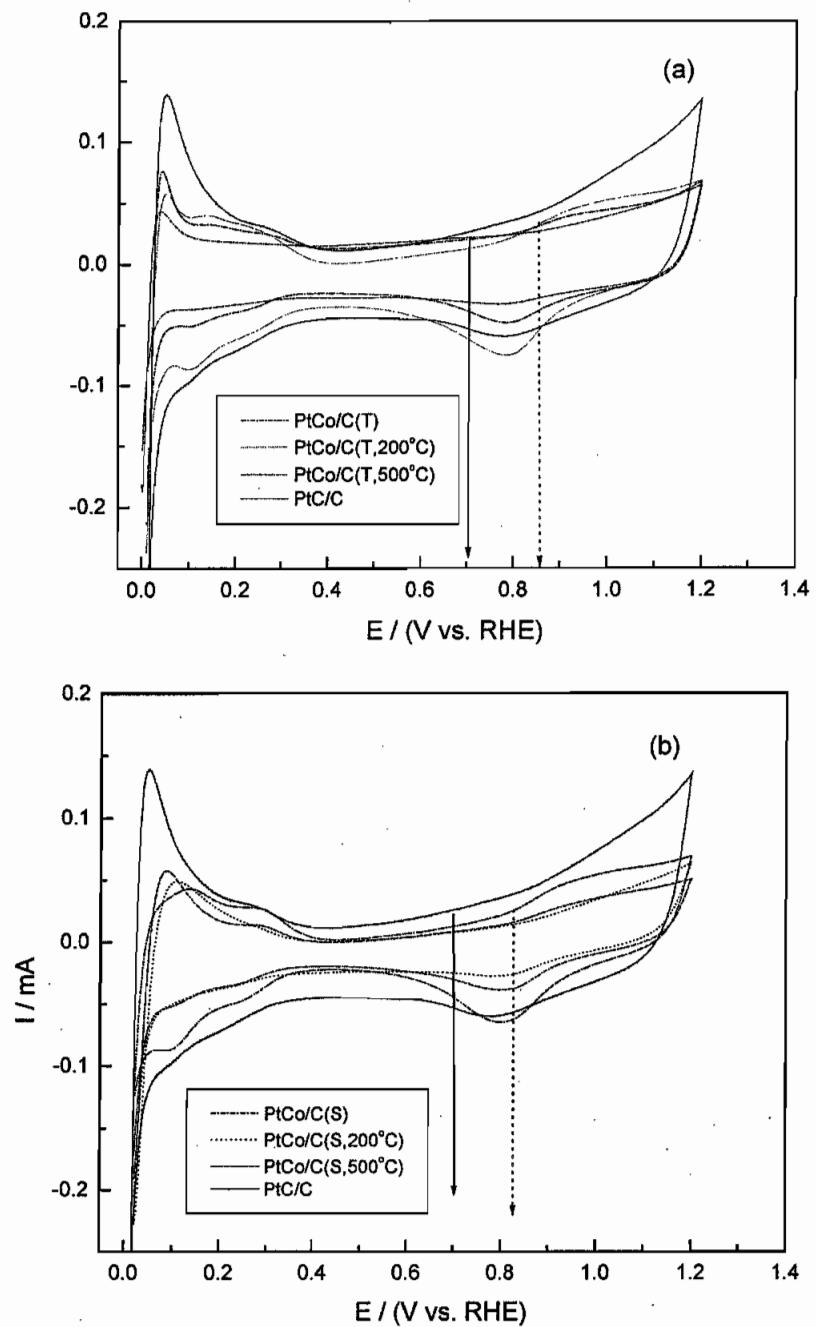
Figure 6. Cyclic voltammetry of (a) PtCo/C (T) and (b) PtCo/C(S) type catalysts at room temperature in Ar saturated 1 M HClO₄ at 50 mV/s
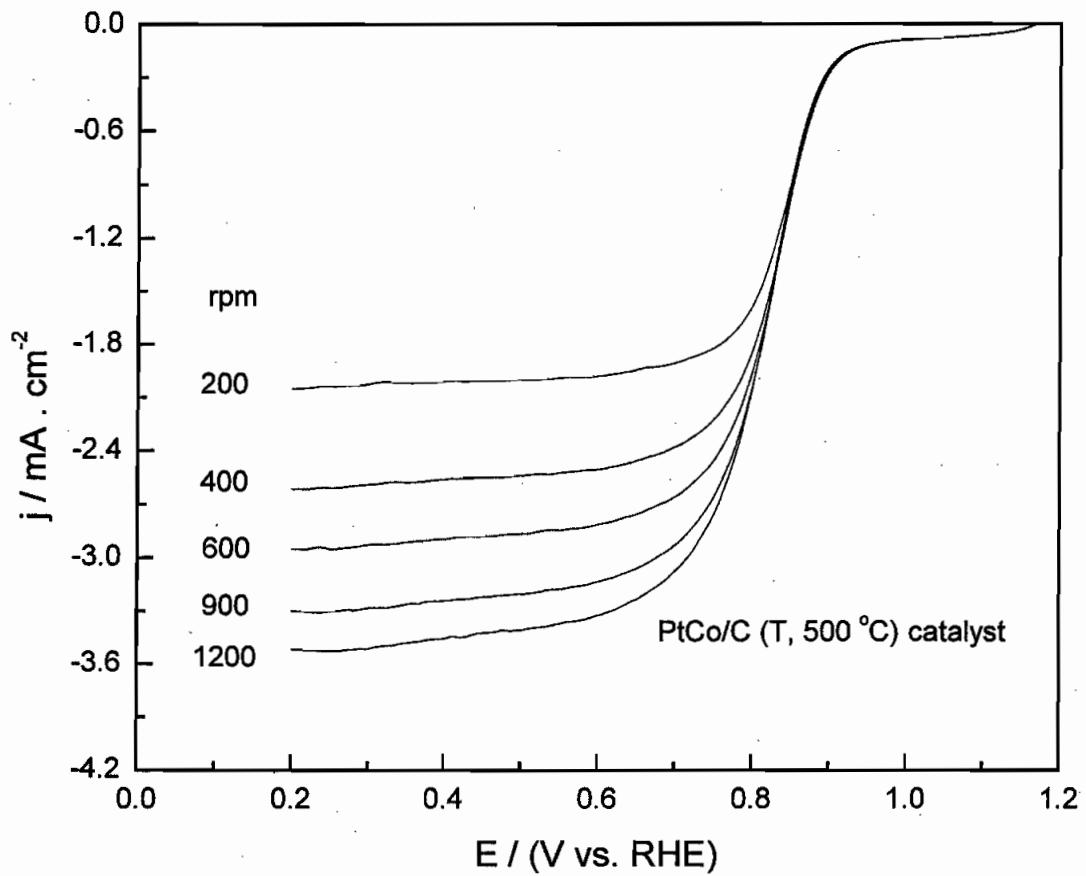
Figure7. Disk currents obtained during the ORR in the cathodic sweep on Pt/C and PtCo(T,500 °C) catalysts at O_2 saturated 1 M $HClO_4$ at room temperature. Scan rate: 25 mV s^{-1}
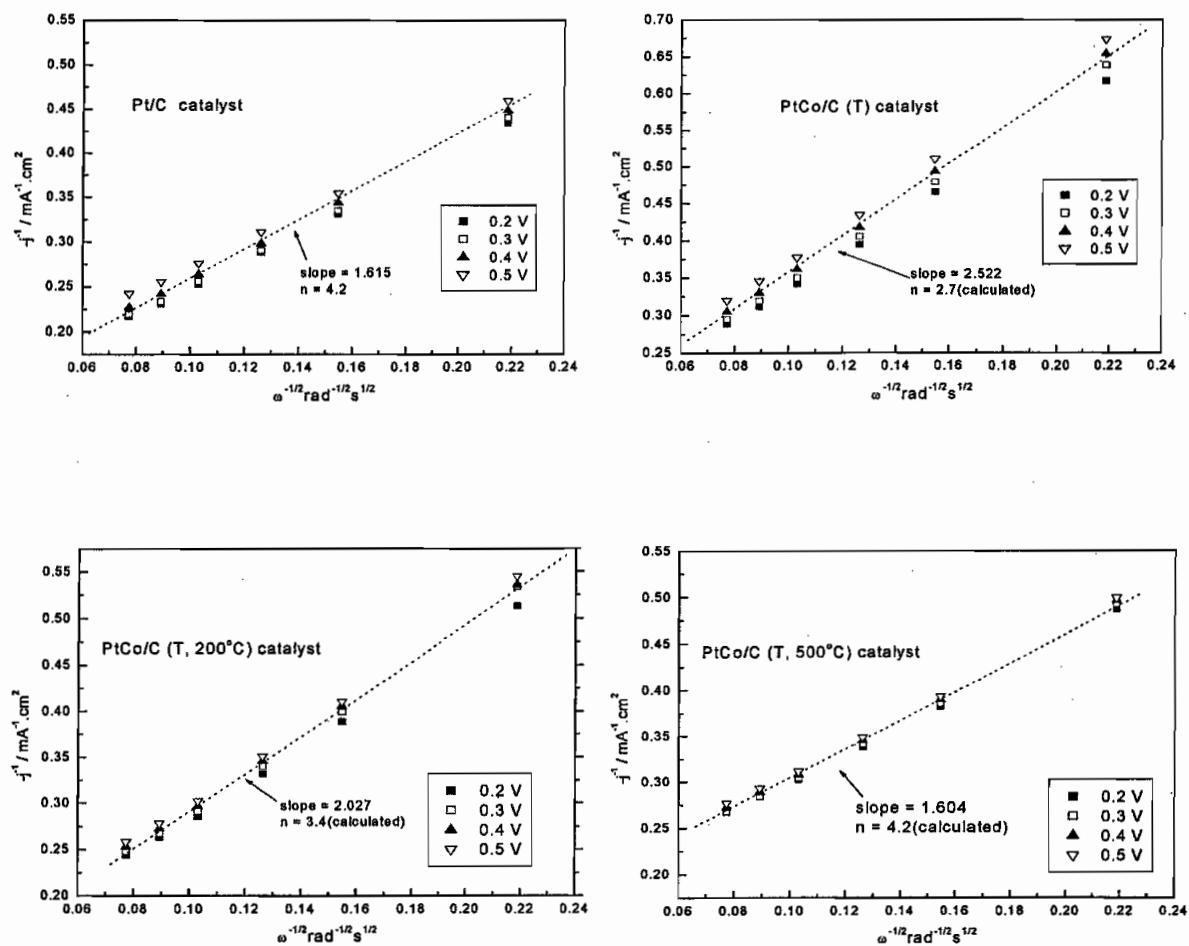
Figure 8. Koutecky-Levich plots at different potentials for orr in the cathodic sweep on Pt/C and PtCo/C type catalysts at O_2 saturated 1 M $HClO_4$ at room temperature. Scan rate: 25 mV s^{-1}.
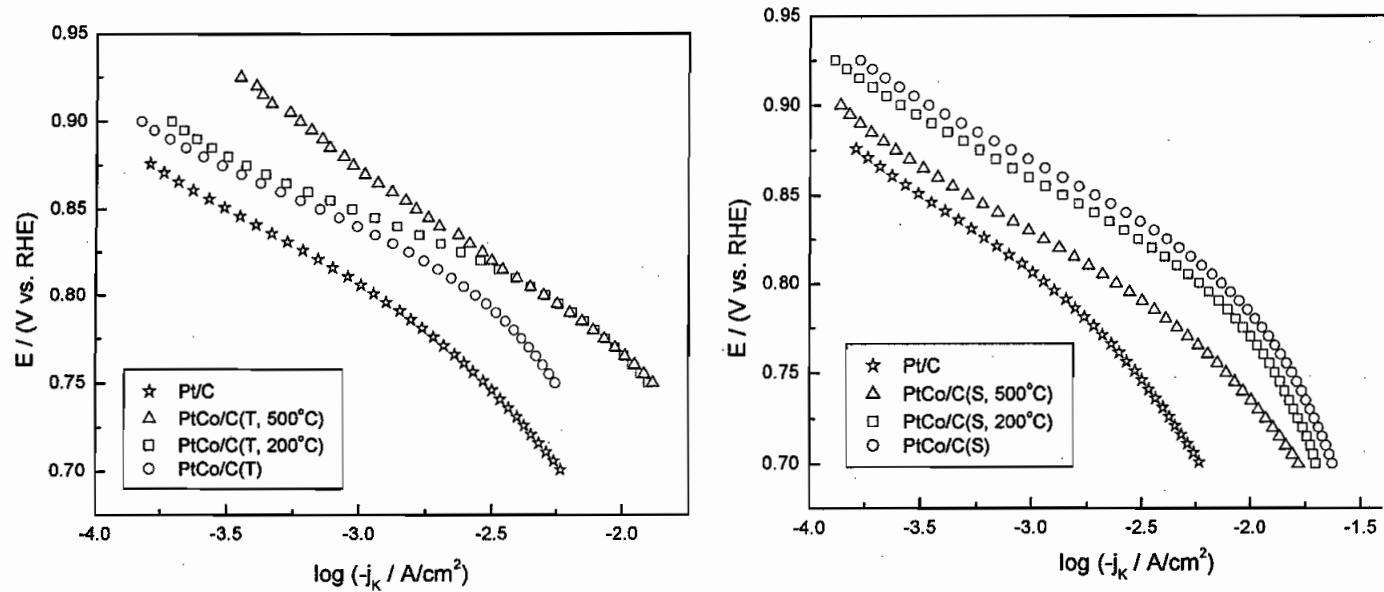
Figure 9. Tafel plots of j_k for orr obtained from disk current in the cathodic sweep at

1200 rpm on Pt/C and PtCo/C type catalysts.
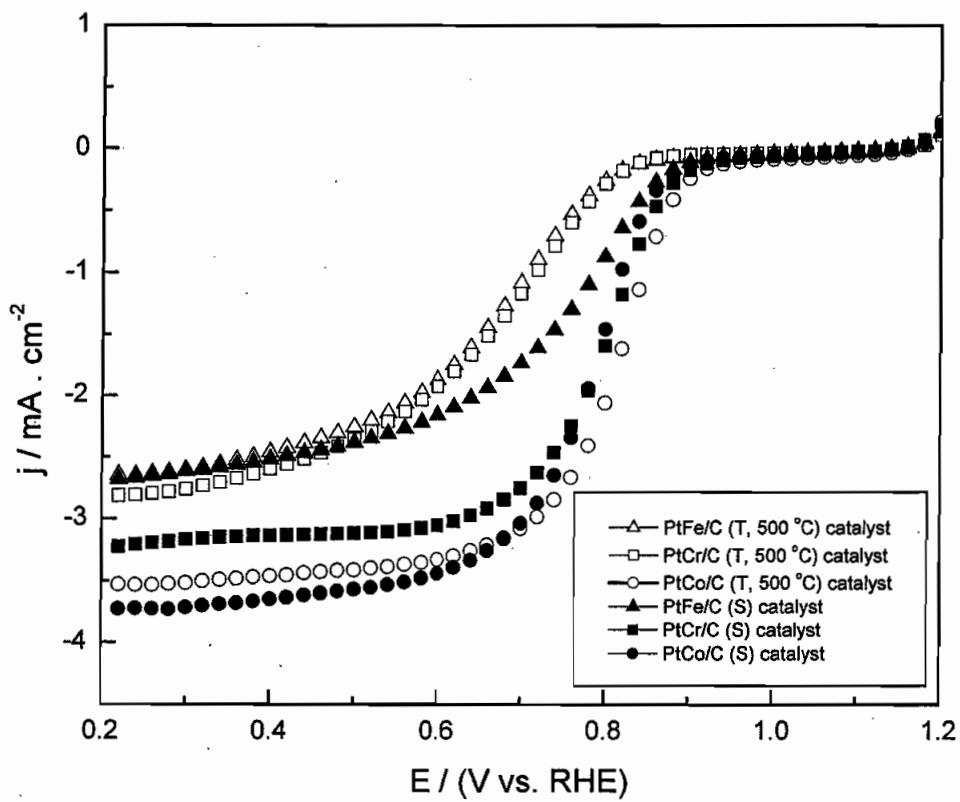
**Figure 10.** Disk currents obtained during the ORR in the cathodic sweep at O_2 saturated 1 M $HClO_4$ at room temperature. Scan rate: 25 mV s^{-1}, rotation rate: 1200 rpm
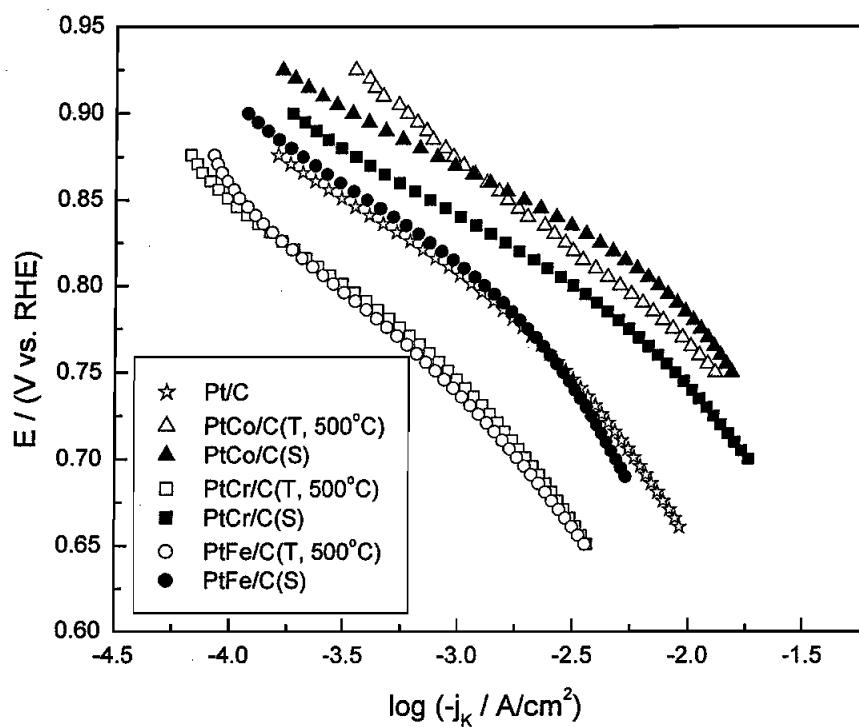
Figure 11. Tafel plots of j_k for orr obtained from disk current in the cathodic sweep at 1200 rpm on Pt/C, PtM/C(S) and PtM/C(T, 500°C) type catalysts

References

(1)   Hoogers, G. *Catalysts for the Proton Exchange Membrane Fuel Cell*; CRC Press, 2003.

(2)   Bregoli, L. J. *Electrochim. Acta* **1978**, *23*, 489.

(3)   Bett, J.; Lundquist, J.; Washington, E.; Stonehart, P. *Electrochim. Acta* **1973**, *18*, 343.

(4)   Landsman, D. A.; Luczak, F. J. US Patent 4,316,944, 1982.

(5)   Luczak, F. J.; Landsman, D. A. US Patent 4447506, 1984.

(6)   Mukerjee, S.; Srinivasan, S. *J. Electroanal. Chem.* **1993**, *357*, 201.

(7)   Jalan, V.; Taylor, E. J. *J. Electrochem. Soc.* **1983**, *130*, 2299.

(8)   Glass, J. T.; Cahen, G. L., Jr.; Stoner, G. E. *J. Electrochem. Soc.* **1987**, *134*, 58.

(9)   Paffett, M. T.; Beery, J. G.; Gottesfeld, S. *J. Electrochem. Soc.* **1988**, *135*, 1431.

(10)   Beard, B. C.; Ross, P. N., Jr. *J. Electrochem. Soc.* **1990**, *137*, 3368.

(11)   Appleby, A. J. *Energy* **1986**, *11*, 13.

(12)   Jalan, V. M. J. US Patent 4192907, 1980.

(13)   Itoh, T.; Katoh, K. US Patent 5024905, 1991.

(14)   Itoh, T.; Kato, K. US Patent 5096866, 1992.

(15)   Tsurumi, K.; Nakamura, T.; Sato, A. US Patent 4985386, 1991.

(16)   Stonehart, P. US Patent 5593934, 1997.

(17)   Hwang, J. T.; Chung, J. S. *Electrochim. Acta* **1993**, *38*, 2715.

(18)   Neergat, M.; Shukla, A. K.; Gandhi, K. S. *J. Appl. Electrochem.* **2001**, *31*, 373.

(19)   Sun, S.; Anders, S.; Thomson, T.; Baglin, J. E. E.; Toney, M. F.; Hamann, H. F.; Murray, C. B.; Terris, B. D. *J. Phys. Chem. B* **2003**, *107*, 5419.

(20)   Sun, S.; Murray, C. B.; Weller, D.; Folks, L.; Moser, A. *Science (Washington, D. C.)* **2000**, *287*, 1989.

(21)   Zhang, X.; Chan, K.-Y. *J. Mater. Chem.* **2002**, *12*, 1203.

(22)   Schmidt, T. J.; Gasteiger, H. A.; Stab, G. D.; Urban, P. M.; Kolb, D. M.; Behm, R. J. *J. Electrochem. Soc.* **1998**, *145*, 2354.

(23)   Paulus, U. A.; Endruschat, U.; Feldmeyer, G. J.; Schmidt, T. J.; Bonnemann, H.; Behm, R. J. *J. Catal.* **2000**, *195*, 383.

(24)   Carpenter, E. E. *J. Magn. Magn. Mater.* **2001**, *225*, 17.

(25)   Boennemann, H.; Brijoux, W.; Brinkmann, R.; Fretzen, R.; Joussen, T.; Koeppler, R.; Korall, B.; Neiteler, P.; Richter, J. *J. Mol. Catal.* **1994**, *86*, 129.

(26)   Lin, J.; Zhou, W.; Kumbhar, A.; Wiemann, J.; Fang, J.; Carpenter, E. E.; O'Connor, C. J. *J. Solid State Chem.* **2001**, *159*, 26.

(27)   Giannakas, A. E.; Ladavos, A. K.; Pomonis, P. J. *Appl. Catal., B* **2004**, *49*, 147.

(28)   Pileni, M. P. *Langmuir* **1997**, *13*, 3266.

(29)   Wu, M.-L.; Chen, D.-H.; Huang, T.-C. *Langmuir* **2001**, *17*, 3877.

(30)   Cullity, B. D. *Elements of X-ray diffraction*; Second Edition, Addision-Wesley Publishing Company, 1978.

(31)   Laidler, K. J.; Meiser, J. H.; Sanctuary, B. C. *Physical Chemistry (Fourth Edition)*; Houghton Mifflin Company: Boston, 2003.

(32)   Arico, A. S.; Antonucci, V.; Giordano, N.; Shukla, A. K.; Ravikumar, M. K.; Roy, A.; Barman, S. R.; Sarma, D. D. *J. Power Sources* **1994**, *50*, 295.

(33)   Powder Diffraction Files (Inorganic Volumes). *4-802, JCPDS International Center for Diffraction Data, USA.*

(34)   Arico, A. S.; Shukla, A. K.; El-Khatib, K. M.; Creti, P.; Antonucci, V. *J. Appl. Electrochem.* **1999,** *29,* 671.

(35)   Powder Diffraction Files (Inorganic Volumes). *29-1423, JCPDS International Center for Diffraction Data, USA.*

(36)   Powder Diffraction Files (Inorganic Volumes). *34-1080, JCPDS International Center for Diffraction Data, USA.*

(37)   Powder Diffraction Files (Inorganic Volumes). *29-499, JCPDS International Center for Diffraction Data, USA.*

(38)   Elkins, K. E.; Vedantam, T. S.; Liu, J. P.; Zeng, H.; Sun, S.; Ding, Y.; Wang, Z. L. *Nano Letters* **2003,** *3,* 1647.

(39)   Smart, L. E.; Moore, E. A. *Solid State Chemistry, Second Edition*; Stanley Thornes, 1998.

(40)   West, A. R. *Solid State Chemistry and its Applications,* 1990.

(41)   Stonehart, P. *J. Appl. Electrochem.* **1992,** *22,* 995.

(42)   Murthi, V. S.; Urian, R. C.; Mukerjee, S. *J. Phys. Chem. B* **2004,** *108,* 11011.

(43)   Crabb, E. M.; Marshall, R.; Thompsett, D. *J. Electrochem. Soc.* **2000,** *147,* 4440.

(44)   Markovic, N. M.; Widelov, A.; Ross, P. N.; Monteiro, O. R.; Brown, I. G. *Catal. Lett.* **1997,** *43,* 161.

(45)   Paulus, U. A.; Wokaun, A.; Scherer, G. G.; Schmidt, T. J.; Stamenkovic, V.; Markovic, N. M.; Ross, P. N. *Electrochim. Acta* **2002,** *47,* 3787.

(46)   Paulus, U. A.; Schmidt, T. J.; Gasteiger, H. A.; Behm, R. J. *J. Electroanal. Chem.* **2001,** *495,* 134.

(47)   Duron, S.; Rivera-Noriega, R.; Nkeng, P.; Poillerat, G.; Solorza-Feria, O. *J. Electroanal. Chem.* **2004,** *566,* 281.

(48)   Pleskov, Y. V.; Filinovskii, V. Y. *The Roatong Disk Electrode*; Plenum Press: New York, 1976.

(49)   Hsueh, K. L.; Gonzalez, E. R.; Srinivasan, S. *Electrochim. Acta* **1983,** *28,* 691.

(50)   Maruyama, J.; Abe, I. *Electrochim. Acta* **2003,** *48,* 1443.

(51)   Coutanceau, C.; Croissant, M. J.; Napporn, T.; Lamy, C. *Electrochim. Acta* **2000,** *46,* 579.

(52)   Maruyama, J.; Inaba, M.; Morita, T.; Ogumi, Z. *J. Electroanal. Chem.* **2001,** *504,* 208.

(53)   Maillard, F.; Martin, M.; Gloaguen, F.; Leger, J. M. *Electrochim. Acta* **2002,** *47,* 3431.

(54)   Grgur, B. N.; Markovic, N. M.; Ross, P. N. *Can. J. Chem.* **1997,** *75,* 1465.

(55)   Damjanovic, A.; Sepa, D. B. *Electrochim. Acta* **1990,** *35,* 1157.

(56)   Takasu, Y.; Fujii, Y.; Yasuda, K.; Iwanaga, Y.; Matsuda, Y. *Electrochim. Acta* **1989,** *34,* 453.

(57)   Gojkovic, S. L.; Zecevic, S. K.; Savinell, R. F. *J. Electrochem. Soc.* **1998,** *145,* 3713.

(58)   Jiang, J.; Kucernak, A. *Electrochem. Solid-State Lett.* **2000,** *3,* 559.

II.3   Determination of Site Selective Adsorption of Oxides on Pt and Pt Alloys: An In situ
   XANES Investigation

Abstract

An analysis of x-ray absorption spectroscopy data (XANES and EXAFS) at the Pt L_3 edge for Pt-M alloy materials (M=Co, Cr, Ni, Fe) and at the Co K edge for PtCo is reported for Pt-M/C electrodes in $HClO_4$ at different potentials. The XANES data are analyzed using the $\Delta\mu$ method, which utilizes the spectrum at some potential V minus that at 0.54 V (RHE) representing a reference spectrum. These data provide direct spectroscopic evidence for the inhibition of OH chemisorption on the cluster surface in the Pt-M alloys. This OH chemisorption, decreasing in the direction Pt > Pt-Ni > Pt-Co > Pt-Fe > Pt-Cr, is directly correlated with the previously reported fuel cell performance (electrocatalytic activity's) of these alloys, confirming the important role of OH poisoning of Pt sites in working fuel cells. EXAFS analysis shows that the alloys studied have different morphologies, the Pt-Ni and Pt-Co alloy clusters were more homogenous with M atoms on the surface, while the Pt-Fe and Pt-Cr alloys had a "Pt skin". The cluster morphology determines which previously proposed OH inhibition mechanism dominates; the electronic mechanism in the presence of the Pt skin, while the lateral interaction plays a more significant role when M-OH groups exist on the surface.

The salient aspects of this section are discussed in the context of the following:

OH Formation. - This work will examine the effect of alloying on OH adsorption on the Pt-M surface. It is well known that the kinetics of the ORR is dependent on the intermediate products produced, either OH^- or O_2H^- which may be adsorbed on the Pt surface.[1,2,3] It is believed that alloying may reduce the formation of "poisons" or OH formation on the Pt surface sites which frees up the Pt sites to participate in O_2 reduction.[Error! Bookmark not defined.,4] Figure 1 shows a typical cyclic voltammetry (CV) curve comparing a Pt/C electrode with an alloyed electrode, Pt-Co/C. Large differences in the onset and extent of oxygenated species on the electrode are evident after 0.8V RHE. Clearly the Pt-Co alloy CV suggests a reduced affinity for oxidation in water above 0.80 V RHE compared to Pt. Similar CV results have been reported for other Pt-M alloys showing indirect evidence for a reduced affinity for O(H)[Error! Bookmark not defined.,Error! Bookmark not defined.,5,8,6]; however, no direct spectroscopic evidence has been reported showing a reduced coverage by O(H) (O(H) here indicates OH or O) in the alloys.

The formation of adsorbed OH on Pt in water has been extensively studied. It is widely accepted that the oxidation of Pt surfaces in water occurs in distinct steps, with the first step, the formation of an adsorbed OH species above 0.80, V (RHE). The mechanism proposed nearly 40 years ago by Bockris *et al*,[7] proceeds according to the following steps:

$$Pt + H_2O \rightarrow PtOH + H^+ + e^- \quad \text{OH formation} \quad 0.85\text{-}1.10V \quad (1)$$
$$Pt\text{-}OH \rightarrow PtO + H^+ + e^- \quad \text{Place exchange} \quad 1.10\text{-}1.40V \quad (2)$$
$$PtO + H_2O \rightarrow PtO_2 + 2H^+ + 2e^- \quad \text{Pt oxide formation} \quad >1.40V \quad (3)$$
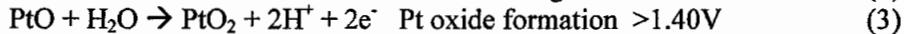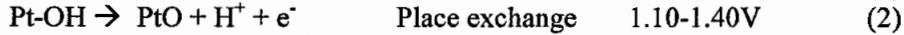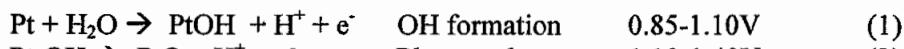
It is unclear why the alloys reduce O(H) formation. Studies have provided indirect evidence that Pt-OH formation in fuel cells results from the interaction of water with Pt as described above and not from the reaction of O_2, such as that in a fuel cell.[8,9,10] Several theoretical calculations have shown that OH co-adsorbs with water stabilizing the OH through hydrogen bonding with the water.[11,12,13] Experimental results using LEED and RAIRS confirmed that on a Pt(111) surface, adsorbed O reacts with water to form an OH/H_2O mixture which is stabilized by H bonding.[14] However, the exact role of water in such adsorption in a fuel cell is unknown, since every effort is made to reduce the amount of water present by using highly concentrated acid electrolyte or even an exchange membrane. Many have

suggested that the inhibition of OH on alloy surfaces arises from changes in the electronic structure of the cluster as a result of alloying or even changes in the physical structure of the cluster, such as the formation of a Pt skin.[Error! Bookmark not defined.] Others have suggested that the M metal is indeed at the surface, and that the repulsion between OH species on the M and on the Pt sites decreases the coverage of O(H) on the Pt.[Error! Bookmark not defined.] These widely different mechanisms clearly indicate that the effect of the alloying on the OH adsorption, the nature of the Pt-OH bonding, as well as the effect of the distribution or composition of the bimetallic alloy, is still not well understood.

Surface Segregation and Leaching. - Knowledge of the surface morphology and composition of Pt-M clusters is crucial to understanding the adsorbate interactions on the alloyed surfaces. There have been several studies reported over the years using a variety of techniques to characterize the Pt-M surface. These include Extended X-Ray Absorption Fine Structure (EXAFS), X-Ray Photoelectron Spectroscopy (XPS), Auger electron spectroscopy (AES), IR spectroscopy and various electrochemical techniques.[15,16,17,18] Using cyclic voltammetry, Schmidt *et al*[19] integrated base voltammograms and made an estimate of the fraction of active Pt surface atoms. A 1:1 Pt-Ni catalysts showed 70% Pt atoms at the surface compared to only 58% Pt atoms in a 1:1 Pt-Co alloy. This indicated that the Pt-Ni particle surface was closer to that of pure Pt than in the Pt-Co case. The more Pt-like behavior for the Pt-Ni catalyst suggested that the Ni may have "leached" out from the surface. In another study, XPS results on some Pt-Fe, Pt-Ni and Pt-Co thin film electrodes showed an almost total absence of M atoms at the surface, which was also attributed to a "leaching" out process of the M atoms, occurring either as a result of an acid wash used during the electrode preparation or exposing the electrode to potentials greater than 1.10 V (vs. RHE)[Error! Bookmark not defined.]. These results are consistent with studies by Mizukami *et al* on similar alloys but on alloy clusters.[20] Murthi et al[21] recently prepared two sets of PtM/C alloy catalysts, acid-washed in 1 M HClO4 for 48 ours at RT, and unwashed. The acid wash apparently removes the M metal from the surface, and XANES data supported this. After 9h with the electrodes polarized at 0.9 V, the two electrodes (washed and unwashed) showed similar XANES results suggesting leaching of the reactive M also occurs under polarization. However both Stamenkovic *et al*[Error! Bookmark not defined.] and Paulus *et al*[22] found that the Co in a Pt-Co alloy did not leach out, and the cluster remained homogenous. Studies done by Obradovic[23] and Bardi[24] on Pt-Co alloys showed similar results. This non-leaching character in Pt-Co was attributed to an electronic stabilization of the cobalt in the alloy. In still other work, low energy electron diffraction (LEED) studies showed that Pt-Co and Pt-Ni alloys in a Pt_xM_{x-1} composition resulted in M rich cluster surfaces.[25] In contrast Stamenkovic et al[Error! Bookmark not defined.] found that for Pt3Ni alloys, the as prepared sputtered surface contained 75% Pt atoms, and after annealing at 950K ,contained 100% Pt (a Pt skin). These electrodes showed different reactivity in rotating disk studies suggesting that the Ni at the surface did not leach out.

Unfortunately, the method of alloy preparation and electrochemical treatment is different in many of these cases, so one cannot conclude anything fundamental yet about when M surface segregation or leaching will occur. Although DFT calculations by Norskov's group[26] do suggest a strong antisegregation effect in the case of PtCo and PtFe alloys, where the Fe and Co atoms prefer to remain in the interior of the alloy allowing for a Pt skin, the effects of leaching in acid or at raised potentials in electrolytes are not entirely known. Nevertheless, this summary should make it clear that knowledge of the surface composition of the alloy cluster is critical, and it must be determined *in situ* in order to understand the catalytic activity differences found.

Not only is a determination of the surface composition of an alloy cluster important, along with a determination of the true particle size, the extent of initial alloy formation must also be determined. A review by Antolini[27] examined the Pt-Pt bond distance or lattice

constant for several Pt-M alloy clusters determined previously using either XRD or EXAFS. The lattice constant is a measure of alloy formation, since it is found that in true bulk alloys the Pt-Pt distance decreases with the amount of M as well as in direct relation to its electronegativity. Antolini's analysis reveals that the extent of alloy formation depends critically on the preparation procedure, such as the temperature or acid solution utilized in the preparation as well as the choice of the alloying element. Using the lattice constant, the fraction of M alloyed could be determined, and a plot of the logarithm of this fraction verses 1/T enabled the activation energy to be obtained for that particular alloy formation. Not surprising, this energy of activation varied nearly linearly with the atomic radius of M, suggesting that bigger M atoms have a more difficult time diffusing into or mixing with the Pt. Further, the particle diameter was also determined, and from a similar plot of ln(diameter) vs. 1/T an activation energy for particle growth was obtained. This activation energy depended strongly on the acidity of the support, and was relatively independent of M. It is clear from Antolini's review that the alloys considered show a variety of compositions (different from the starting mixture), morphologies and particle sizes. Further most were not "true alloys" in the sense that they did not have a homogenous composition even after initial preparation. In summary, the preparation procedure for metal alloys strongly affects the particle composition, morphology, and size, and this obviously affects the composition of the particle surface. It is obvious these factors must be taken into consideration when comparing the catalytic activity of certain alloy materials. To date this has not always been the case.

X-ray Absorption Spectroscopy. - The primary reason for the lack of detailed information on OH inhibition or extent of OH coverage on an electrode in an electrochemical cell, as well as some information on particle size and composition, is the absence of a general *in situ* spectroscopic technique that can provide such information. Until recently, XAS analysis has been limited to providing geometric information on systems with short-range order, i.e. the normal EXAFS technique. However, recent advances in the interpretation of XAS (in both EXAFS and X-ray Absorption Near Edge Structure (XANES)) now enable XANES to provide direct adsorbate binding site information along with the usual particle size and composition from EXAFS.[28] It has been recently reported that the electron scattering producing the Pt L_3 XANES is very sensitive to the adsorption of both O and H. Using a novel analysis technique that allows isolation of this Pt-adsorbate scattering, combined with theoretical calculations, allows for the *in situ* determination of adsorption sites (i.e. atop, bridged, three fold) on platinum electrodes utilizing Pt $L_{2,3}$ XANES.[32] This XANES data can be interpreted with full multiple scattering theoretical results from the FEFF 8.0 code[29] and local density functional (LDF) results using the Amsterdam Density Functional (ADF) code.[30] Comparison of theory with experimental data allows unique spectral signatures to be determined for H, OH, and O in atop, bridged, and 3-fold fcc absorption sites respectively. Using this technique, Teliska *et al*,[31,32] have previously determined the adsorption sites and changes with coverage, of atomic H, OH, and O on a Pt/C electrode in an aqueous $HClO_4$ or H_2SO_4 electrolyte.

In this part of the report we present Pt L_3 XAS studies on Pt based alloys to determine the cluster morphology, particle size and the effects of alloying on the extent of OH formation *in situ* in an electrochemical cell at various potentials. This information then allows the catalytic activity of the alloy to be related to the surface composition and OH coverage.

Experimental and Analysis Details

Since this investigation constitutes further work on the same series of samples consider previously[Error! Bookmark not defined.,5], the details of the preparation procedure and structure characterization will be given only briefly here. In these prior studies structure property relationships were determined using a combination of *ex situ* XRD (powder diffractometer) and *in situ* XAS and correlated with their activity for oxygen reduction in a

PEMFC environment. The following section gives details of the XANES and EXAFS analysis procedures, which were conducted following this prior published work on the same electrocatalysts.

XAS data from five carbon supported binary Pt alloy electrocatalysts (PtCr, PtMn, PtFe, PtCo and PtNi) procured from ETEK Inc (A Div., of De Nora, North America, Somerset, NJ) and supported on high surface area carbon (Vulcan XC-72, Cabot Corp.) were considered. All electrocatalysts had a metal loading on carbon (Vulcan XC-72, Cabot Corp., USA) of 20 (w/o) similar to that used in previous investigations of PEMFCs.[33,34]. A non-alloyed Pt/C sample with the same metal loading on carbon was used as a control (also obtained from ETEK Inc.,). The preparation methodology used was the well known colloidal 'sol' and carbothermic reduction methods[35,36,37,38]. In these methods, an oxide of the second alloying element is incorporated on the supported Pt/C electrocatalyst. When this is subjected to carbothermic reduction under inert conditions at 900°C for 9 h, the crystallites undergo reduction and alloying on the carbon support, thus providing for supported alloy nanoparticles. The nominal atomic ratios in the binary alloys were 3:1 (Pt:M); these were verified using in situ XANES measurements (see Table 1).

Previously reported[39] XRD analysis of these electrocatalysts showed a very high degree of crystallinity for these samples. Fits of the XRD data to an indexing routine showed that all the patterns (Pt and Pt alloys) corresponded to an fcc lattice. The lattice parameters obtained are summarized in Table 1. In addition, the Pt-Pt bond distances (Table 1) assuming an fcc lattice were calculated based on X-ray line broadening analysis using the Scherrer equation. Alloying of Pt with the first row transition elements (Cr to Ni) results in a lowering of the lattice parameters and hence the Pt-Pt bond distances confirming formation of an alloy. Further there is a smooth inverse relationship between the measured lattice parameters and the electronegativity of the alloying element. From a comparison of the XRD pattern with a standard JCPDS database, the binary Pt alloys were found to form an intermetallic crystalline structure with a primary Pt_3M type superlattice phase having an fcc structure and potential for a secondary PtM type lattice with a tetragonal structure. The extent of contribution from the secondary phase was estimated by the intensity of the diffraction lines due to the PtM phase (such as (001) and (220) diffraction lines in the PtM/C powder pattern). Contribution from these secondary phases was found to be negligible. The particle size obtained using the Pt (111) diffraction line broadening showed that the alloy catalysts have a particle size somewhat larger than for Pt/C; however there does not appear to be any trend with M in the particle size.

The in situ XAS measurements, carried out at the National Synchrotron Light Source (NSLS), Brookhaven National Laboratory (BNL) using beam line X-23 A-2, were conducted in transmission mode using an electrochemical cell and data acquisition setup described in detail elsewhere.[40] To ensure a uniform electrochemical environment for the catalyst, XAS measurements were done in 1M $HClO_4$ with the electrodes in flooded mode. The XANES data were recorded at both the Pt L_3 edge and at the alloying metal K edge for Pt-M alloys and all of the data are reported relative to the reversible hydrogen electrode (RHE). The measurements were made at the open circuit potential and at potentials of 0.00V; 0.24V; 0.54V; 0.84V and 1.14V vs RHE. Results of the detailed XANES analyses are reported here only for potentials at 0.84 and 1.14V vs. RHE.

The analysis of these data proceeded exactly similar to the techniques we have published previously[31,32]. To highlight the effects of adsorption on the surface, the experimental $\Delta\mu = \mu(ads/Pt-M)-\mu(Pt-M)$ for the Pt L_3 edge is obtained by subtracting the L_3 edges from one another where the μ obtained at 0.54 V RHE in $HClO_4$ is used as the reference (i.e. $\mu(Pt-M)$) in this work. At 0.54V, no H or O is expected on the surface, and in $HClO_4$ no directly absorbed ions are expected either (although some O(H) is known to exist on the Co at this potential – see below). The Co K edge data were treated similarly to the Pt L_3 edge data

by subtracting the Co K edges from one another, where the μ obtained at 0.54 RHE in $HClO_4$ is also used as the reference.

As summarized previously, before taking the differences, $\Delta\mu$, the edges may have to be properly aligned in order to remove any initial-state core-level shifts or final-state screening effects due to the chemisorption of hydrogen or oxygen[31,32]. Although the clusters in this work are relatively large (3-6 nm) compared to those used in our earlier work (2-3 nm), we have shown previously that such shifts are negligibly small due to the metallic character of the larger clusters.[32] Therefore in this work the L_3 spectra for the PtM electrodes were subtracted directly without any shift in energy, but only after careful energy calibration. Energy calibration was performed using the Pt L_3 spectra for bulk Pt measured at the same time as that for the sample. Although no other energy shifts were allowed in this work, it must be pointed out that a very careful energy calibration of each spectrum with the bulk Pt is essential to obtain reliable $\Delta\mu$ difference spectra.

The EXAFS analysis was performed using the WINXAS code.[41] The pre-edge background was removed using a linear polynomial and the many-body S_0^2 factor fixed at 0.934, the value obtained using the FEFF8 code. The post-edge background was removed using the normal spline techniques and smoothing criteria that leaves the atomic XAFS scattering in the χ function as described previously.[42,43,44,45] Reference phase and amplitude functions for the Pt-Pt scattering were obtained from FEFF8 calculations on the Pt_6 cluster discussed below.

Theoretical Calculations. - Two different yet complimentary theoretical calculations were performed in order to fully characterize the bonding site information. XANES data can now be interpreted utilizing full multiple-scattering theoretical results from the FEFF 8.0 code.[46] Further density functional theory (DFT) results using the Amsterdam Density Functional (ADF) code can provide bonding site preferences and bond energies.[47]

FEFF8 calculations were performed to interpret the $\Delta\mu$ spectra using a series of Pt_6O_x and $Pt_4M_2O_2$ clusters with geometric configuration shown in Figure 2. In all of the calculations, unless otherwise noted, the theoretical $\Delta\mu$ is calculated as $\Delta\mu = \mu(ads/Pt-M) - \mu(Pt-M)$, where the $\mu(Pt-M)$ is obtained from the clean cluster $Pt_4M_2O_2$ with Pt-Pt bond distances of 2.67 A° and Pt-M distances of 2.55 A°. Throughout this work the indicated Pt_6 cluster (i.e. not alloyed) is utilized, with the Pt-Pt distance at 2.77 Å.

The FEFF8 code performs ab-initio self-consistent field, real-space, full multiple scattering calculations.[29] It is known that in the FEFF8 code, the results are quite dependent on the potentials used in the code. Previously it was found that the Dirac-Hara potential with an imaginary part of 5 eV was optimal for describing the Pt-Pt and Pt-O scattering,[42,43] however, the emphasis in that optimization procedure was placed on the 25-150 eV region. Here we are interested in the region below 40eV. Although a more complete analysis in this energy region is required, the Hedin-Lundquist potential is preferred and used in this work to describe the Pt-O scattering following the work of Ankudinov *et al*[29] and our previous work on Pt-H[28,31] and Pt-O[32] scattering.

The Amsterdam Density Functional Package (ADF)[30] was used to perform DFT calculations. Relativistic effects were accounted for and details of the calculations are reported elsewhere.[48] To enhance computational efficiency, several atomic core shells of the Pt atoms were frozen up to and including the Pt 4d level. The geometry optimizations that were performed were carried out in the spin-restricted mode including scalar relativistic effects, thereby excluding spin-orbit effects. The numerical integration precision applied was set to 5.5 significant digits. The applied criterions for the geometry optimization were 1×10^{-3} Hartree for the changes in energy, 1×10^{-4} Hartree/Å for changes in the energy gradients and 1×10^{-2} Å for changes in the Cartesian coordinates.

The ATOMS code developed by Bruce Ravel[49] was used to generate a Pt cluster of approximately 200 atoms with the f m 3 m space group, fcc, a=3.92 of 8 shells. These clusters were used to model the Pt-Pt and Pt-M coordination numbers with different homogenities for comparison with experiment. The average first shell Pt-Pt and Pt-M coordination numbers were calculated for a pure Pt cluster, a true alloy with the metal atoms distributed evenly in a 3:1 Pt:M ratio, and with a "Pt skin". In the latter case the Pt skin consisted of two outer shells of Pt and the inner core in a Pt:M 2:1 ratio.

Results

Figure 3 shows the L_3 absorption spectrum, μ, for a Pt/C electrode at several potentials. Similar data were obtained for the Pt-M alloys (M = Fe, Cr, Co, and Ni). Clear differences in μ, well above the noise level, are seen as a function of potential.

Figure 4 shows the experimental difference spectra, obtained from the data in Fig. 3. Data for both the hydrogen (0.00 and 0.24 V) and oxygen (0.84 and 1.14 V) adsorption regions are shown. It is evident that the lineshapes for both hydrogen and oxygen are different and can be easily distinguished and assigned with theoretical references. Comparisons with theoretical FEFF8 calculations clearly verify that the signatures at 0.0 and 0.24 primarily arise from H in the 3-fold fcc sites, and the data at 0.84 and 1.14 from O in the 3-fold fcc sites as reported previously[31,32].

Figure 5 shows experimental EXAFS data and theoretical fits in R space for the PtCo metal alloy at 0.54 V. Also shown are the Pt-Pt and Pt-M contributions, which are sufficiently different to allow for both coordination numbers and bond distances to be determined. Similar fits were obtained with the other alloys, with the results given in Tables 2-6. [We may be asked for a representative raw EXAFS spectrum, since you have the data I would leave the choice to you, this figure could be put as a inset in the figure 5.]

Determination of OH Coverage. - The theoretical $\Delta\mu$ fingerprints for O/Pt from FEFF8 calculations are shown in Figure 6 for a one-fold atop and n-fold, fcc O adsorption site, comparison with the experimental $\Delta\mu$ at 0.84 V is also included for comparison. These theoretical signatures have been verified by comparison with experimental data as reported previously.[32] The signature for atop adsorption is the most different from the rest, with that for the n-fold (n>1) being indistinguishable from each other. Thus it is possible to distinguish only atop from n-fold O(H) adsorption. As the coordination of O increases, the positive going feature in $\Delta\mu$ for atop O(H) maximizes around 1 eV and moves to higher energy (about 5 eV) subsequently a negative going feature appears at the onset of subsurface O[32]. This change in $\Delta\mu$ with bonding site has been studied previously, and is attributed to a combination of changes in the Pt-Pt bond strength and charge transfer depending on the binding site.[32] In this work, the experimental $\Delta\mu$ will be used primarily to distinguish one-fold atop adsorption from other n-fold O(H) adsorption as suggested in Fig. 6.

Figure 7 shows the experimental $\Delta\mu$ spectra for the Pt-M/C alloys and the pure Pt/C at 0.84 V. The regions where the $\Delta\mu$ maxima in the theoretical signatures fall for one-fold and n-fold are indicated. At the onset of adsorption of oxygenated species, as water dissociates to form OH on the Pt surface around 0.80 V, a one-fold coordinated species is indicated. Thus we attribute the entire magnitude of $\Delta\mu$ over the range indicated to primarily atop adsorption. The decrease in magnitude of the spectral line-shapes on these alloy materials confirms that alloying reduces atop O(H) adsorption when compared with pure Pt/C. The spectral magnitudes also indicate that there is a clear trend in the amount of atop adsorption at 0.84 V, decreasing as the alloying material is changed from Ni to Cr.

In order to determine the more complete nature of the oxygenated species at 0.84 V, local density functional calculations using the ADF code were performed on Pt clusters for

both a single O and an OH group. Final geometry optimizations shows that the single O atom prefers to be at least doubly coordinated in n-fold coordinated positions, i.e. bridge or fcc sites, which completes the octet in the outer valence shell consistent with simple chemical VSEPR (valence shell electron-pair repulsion) theory.[50] Calculations done for the OH species on a Pt cluster show that the OH prefers to be one-fold coordinated.

It is therefore indicated from Fig. 7 that at 0.84 V (RHE) the $\Delta\mu$ signature is primarily that of a one-fold atop coordinated hydroxyl, or OH. Further, the amount of OH adsorption decreases as the alloy materials changes from M = Ni to Cr.

Determination of Cluster Morphology. - In order to gain information regarding the cluster morphology and metal distribution, EXAFS analyses on the data were performed. The Pt-Pt and Pt-M coordination numbers and bond distances obtained from a two shell EXAFS fit (one in the case of pure Pt) are presented in Tables 2-6. These results reveal that the particles have a total coordination number (Pt-Pt + Pt-M) around 9.0-10.5, and therefore have an average particle size of around 3.5-5 nm (containing about 200-800 atoms) based on model cluster calculations assuming spherical clusters.[51] Previous XRD analysis on these same ETEK catalysts (Table 1) suggests particle sizes even larger, roughly 5-6 nm.[Error! Bookmark not defined.,Error! Bookmark not defined.,4] Further these particles show a Pt-Pt bond distance generally smaller (2.71 Å) compared to that in bulk Pt (2.77 Å), consistent with Table 1 and that found previously even for pure small Pt clusters.[52,53,54,55,56,57] The coordination numbers for both Pt-Pt and Pt-M show no systematic variation with potential (except for pure Pt), indicating that significant Pt oxide formation has not set in up to 1.14 V, since after oxide formation the Pt-Pt coordination number is known to decrease rather sharply.[32] Perhaps the most interesting aspect of these results is a comparison of the Pt-M/Pt-Pt coordination number ratio which varies from 0.27 to 0.47. This ratio is plotted in Fig. 8 vs. the number of M 3d electrons, and strongly suggests that the homogeneity of these clusters is varying significantly depending on the metal M.

In order to gain an understanding of how the Pt-M/Pt-Pt ratio can vary depending on the particle homogeneity, spherical model clusters containing around 200 atoms were built up using the ATOMS code. The average coordination numbers were then calculated for a pure Pt cluster (with a Pt-Pt N of 9.9), a homogenous cluster with a Pt:M ratio of 3:1, and for a cluster with a "Pt skin" about two layers thick and an inner core with a Pt:M ratio of roughly 2:1. For a homogenous model cluster the Pt-M/Pt-Pt ratio is found to be around 0.25, which is expected with a 3:1 Pt-M ratio. The only way to increase this ratio is to move more M atoms to higher coordination; that is into the interior of the cluster. The model cluster with two outer layers of Pt mimicking a "Pt skin" gives a Pt-M/Pt-Pt ratio of around 0.5. Figure 8 shows the experimental results and the theoretical results for the model clusters. It is clear that there are primarily two different cluster morphologies among these four alloys, the Pt-Fe and Pt-Cr alloy clusters with a "Pt skin" of at least two Pt outer layers, and the Pt-Co and Pt-Ni alloy clusters having a more homogenous or true alloy composition with metal atoms at the surface. A schematic representation of this "skin effect" vs. a homogeneous alloy is presented in Figure 9 for a Pt$_3$M cluster, here the "Pt skin" represents two atomic layers of Pt and an inner core of Pt$_2$M.

Oxygen Chemisorption. - Based on the *in*-situ electrochemical and XAS data above, it is understood that OH binds in the atop position around 0.80-0.85 V. As the potential is increased and the O coverage increases, O adsorbed in bridged and 3-fold fcc sites dominates.[32] Figure 10 shows experimental □□ data for the Pt-Co and Pt-Cr alloys at 1.14V RHE. The Pt-Co alloy data now clearly show two components with the feature at low energy attributed to atop OH and the higher energy feature to n-fold bridged/fcc coordinated O. Thus at higher potentials (adsorbate coverage), both chemisorbed OH and O can be seen

spectroscopically in the same spectrum. The Pt-Cr alloy on the other hand shows primarily one peak at higher energy attributed to bridged/fcc bonded O. The intensity of the chemisorbed O is significantly lower for the Pt-Co alloy compared with the Pt-Cr alloy. We conclude that although OH adsorption is strongly inhibited on the Pt-Cr alloy cluster as indicated by Fig. 7 and having a Pt skin as indicated by Fig. 8, O adsorption is more strongly inhibited on the more homogenous Pt-Co cluster.

Co K Edge XAS. - Co K edge XAS data were analyzed to determine the range of potentials where the Co is oxidized at the surface of the Pt-Co clusters. It is assumed, based on EXAFS analysis to be discussed below, that the Co atoms at the surface are oxidized above 0.54 V (covered with O(H)). Intuition would suggest this, since Co is much more reactive than Pt toward oxidation and therefore the onset of Co oxidation should be much lower than the onset for OH/Pt around 0.80 V. Finally, theoretical results reported by Anderson *et al*[60] suggest that the Co has OH on it all the way down to 0.00 V. Therefore, we performed XANES analysis at potentials 0.54, 0.24 and 0.0 V to determine if in fact Co is covered with O(H) throughout this potential range, or where the onset of OH occurs.

The experimental $\Delta\mu = \mu(V) - \mu(0.54\ V)$ as obtained from Co K-edge XANES data at 0.24 and 0.00 V are plotted in Fig. 11. The overall intensities are quite small, so therefore the noise level is significant, but the data clearly show that the $\Delta\mu$ signatures are similar at 0.0 and 0.24 V, but that this signature is much larger at 0.00 V. This strongly suggests that the O(H) coverage must be decreasing as we approach 0.00 V and this decrease already begins at 0.24 V. [This statement contradicts itself, either the signature at 0.0 V is lower so we change the word highlighted in the above scentence or the latter statement needs to be modified. Looking at the figure it is hard to distinguish between 0.0 and 0.24 as both are solid lines, only you know the difference. Also please make the change in the figure 11]

We attempt to confirm this decreasing OH coverage using FEFF8 calculations. To calculate the appropriate $\Delta\mu$ signature with FEFF8, O atoms are placed on Co atoms in the atop position at 2.0 A° above each Co atom as shown in Fig. 11. This represents our model for the reference at 0.54 V. We replace the OH with H atoms at 2.0 Å above the Co, and also place H_2O molecules at 2.0 Å above the H atoms to represent water in the double layer. This represents our model of the Pt-Co electrode at 0.00 V. As can be seen in Figure 11, the theoretical $\Delta\mu$ spectrum reasonably reproduces the two low energy features in the experimental data and also reproduces the higher energy oscillations. The theoretical $\Delta\mu$ was scaled to fit the experimental data and shifted by 5 eV (FEFF8 always requires some shift for best alignment with experiment). This reasonable agreement between the theoretical and experimental $\Delta\mu$ confirms that H replaces the OH on the Co; this process beginning (albeit small) already around 0.24 V.

Co K edge data (i.e. Fourier Transform (FT) of χ) also taken at 0.00, 0.24, and 0.54 V are shown in Figure 12. Note the remarkable similarity between the data at 0.24 and 0.54, and the significant change in the Fourier transform occurring at 0.00 V. Thus even without any EXAFS analysis, the data indicates that something significant has changed with respect to the Co upon going from 0.24 to 0.00 V. A complete EXAFS analysis requires fitting 5 different shells to this data (Pt-Pt, Pt-Co, Pt-H, Pt-O_{short} and Pt-O_{long}) over the range $1\text{Å} < R < 2.5\text{Å}$. This leads to significant linear dependencies and statistical inaccuracies, nevertheless, such an analysis is in progress and is not the focus of this work. Preliminary results suggest that dominant contributions to the various peaks are as those indicated in Fig. 12.

The FT at 0.00V shows a loss of the Co-O peak at 1.5 Å and a new intensity at 1.2A° and at 1.8-2.0Å which is not seen in the 0.24V spectra. The 1.2 Å peak is attributed to the adsorption of H, and the additional intensity at 1.8 Å to water in the double layer H-bonded to the H atoms on the surface, as illustrated by the cluster in Fig. 11. This scattering from water

85

in the double layer which falls right at the principle Pt-Pt peak is consistent with previous EXAFS data taken in an electrochemical cell.[58] Thus these EXAFS results, although qualitative, are consistent with our interpretation of the XANES data and prior theoretical results[60] showing that the Co has chemisorbed O(H) on it all the way down to 0.24 V and beyond, but clearly at 0.00 V, this O(H) is partially or totally replaced by H.

Discussion

As mentioned in the Introduction, the importance of OH poisoning and its effects on a Pt electrode in a fuel cell has been controversial. Our XAS data clearly show OH species adsorbed in an atop site on Pt at 0.84 V vs. RHE. It is clear from our results that alloying does significantly decreases the amount of OH adsorption in all cases. However, there is also a strong dependence on the metal M; the amount of OH on the Pt-Ni and Pt-Co alloys is much higher compared to that for Pt-Fe and Pt-Cr at 0.80 V. At 1.10 V however, more O is adsorbed in the bridge/fcc sites on the Pt-Cr compared to the Pt-Co. These results are summarized Fig's 7,10 and 13.

The EXAFS results show that the morphology of the Pt-Ni and Pt-Co alloy clusters are very different than the Pt-Fe and Pt-Cr clusters, the former homogenous, the latter with a Pt skin. This difference provides some information as to the dominant mechanism for OH inhibition with the alloys. Two mechanisms, proposed previously, are considered below: Electronic effects induced by the M metal in the alloy, and lateral interactions between OH on the M and on the Pt.

Electronic Effects. - One of the previously proposed mechanisms for OH inhibition is an electronic change in the Pt as a result of alloying.[Error! Bookmark not defined.,Error! Bookmark not defined.] These electronic changes include changes in the d-band orbital vacancies, or changes in the physical structure (bond distance and coordination numbers) relative to pure Pt as a result of alloying. It has been suggested previously that the alloying metal M may lie below the surface with a "Pt skin".[4,59] If the surface of the catalyst is mainly Pt, this rules out the lateral interaction mechanism to be described below, but may result in a decreased affinity for the formation of Pt-OH via an electronic effect.[60] Such an electronic effect would be expected to shift the onset for adsorption of OH, and hence provide the most dramatic effect at low potential, e.g. 0.84 V, but not be as significant at higher potentials because the entire particle surface is still Pt. This is exactly what the XANES data show, a dramatic decrease in OH coverage compared to pure Pt at 0.84 V on the Pt-Fe and Pt-Cr alloy clusters, but a smaller decrease in O coverage at 1.14 V at least compared to the decrease with Pt-Co and Pt-Ni.

Lateral Interactions. - Another possible mechanism for OH inhibition, suggested by Paulus *et al.*,[22] is adsorbate-adsorbate lateral interactions which arises when surface segregation has not taken place and the cluster is more homogeneous with metal M atoms present at the surface. Since the more reactive M atoms at the surface exists as M-OH above 0.24 V (at least for Pt-Co as shown above), these OH groups can repel other O(H) groups that want to come down on the surface Pt atoms at 0.84 V and above. Figure 14 shows a pictorial view of the electronic and lateral interactions.

The EXAFS results indicate that the Co and Ni alloys are more homogenous alloys with M atoms at the surface. The effectiveness of the lateral interactions should increase with coverage, since the first atoms to adsorb on the Pt can "steer clear" of the M atoms, but at higher coverage these preferred sites become occupied, leaving only the sites near the M atoms where the lateral interactions are the largest. Thus the O(H) inhibition on Pt-Co and Pt-Ni should be most effective at higher coverage as verified by the XANES data in Fig. 10 taken at 1.14 V. At 1.14 V the O coverage is much lower on the Pt-Co alloy compared to the Pt-Cr alloy.

Correlation of XANES results with fuel cell data and CV plots. - We suggest above that the electronic mechanism is more effective at inhibiting OH adsorption around 0.70-0.90 V, while the lateral interaction mechanism is more effective at inhibiting O(H) at higher coverage and hence higher potential (0.90-1.20 V). Figure 15 shows the $\Delta\mu$ amplitude reflecting the OH coverage at 0.80 V vs. the current, I_{900}, at 900 mV vs. RHE reported previously by Mukerjee et al [Error! Bookmark not defined.,4] on these same samples. The relative OH coverage at 0.80 V is indicated by Area$_{\Delta\mu}$, determined by integrating the $\Delta\mu$ curves in Fig. 7 from –5 to 10 eV (i.e. obtaining the area under the curve). Mukerjee et al[Error! Bookmark not defined.] normalized the I_{900} currents relative to the electroactive surface area as determined by integrating the Faradaic H current from 0.10 to 0.30 V to account for particle size and for surface Pt composition (i.e. possible M atoms at the surface). Thus the reported currents, I_{900} (mA/cm^2 Pt), and Area$_{\Delta\mu}$ plotted in Fig. 15 have taken into account all of the effects of particle size and surface composition.

A clear linear correlation is found in Fig. 15 showing the direct effect of the OH poisoning, this alone can account for the activity enhancement seen in Pt based alloy catalysts in a fuel cell. Thus no significant change in the initial rds involving the O$_2$ adsorption is needed to explain the enhancement. The plot suggests that "full" OH coverage is obtained when Area$_{\Delta\mu}$ equals 5.5 at I_{900} equal to zero. It must be recognized however that the Area$_{\Delta\mu}$ values here were obtained in an electrochemical cell containing 1M HClO$_4$, not in an actual fuel cell, and thus the magnitudes of Area$_{\Delta\mu}$ do not necessarily reflect the OH coverage in the fuel cells. Nevertheless the estimated value of Area$_{\Delta\mu}$ = 5.5 at full coverage is perfectly reasonable, since the theoretical atop signature in Fig. 6 was obtained from FEFF8 assuming a Pt-OH coordination of 1, and its Area$_{\Delta\mu}$ in Fig. 6 is just slightly larger than that for Pt/C at 0.84 V. Thus the OH coverage found at 0.84 V in the electrochemical cell appears to nicely model that in the PEM fuel cell at 0.90 V. Fig. 15 also suggests that I_{900} could be as high as 3.3 times that for pure Pt (1.3 at zero OH coverage/0.36 for pure Pt) assuming zero OH poisoning.

Figure 16 compares the positive going scan of the cyclic voltammograms for the Pt and the Pt alloys studied in this work in 1M TFMSA. These CV curves show an upward shift in the onset for O(H) adsorption in the order Pt < PtCo < PtCr < PtFe; in approximately the same order as the increase in fuel cell reactivity as indicated in Fig. 15. The current well above 0.90 V does not appear to reflect the effects of the lateral interactions in the PtCo alloy, which should reduce the O coverage in this range as found from the XANES data. We suspect that the dominant components of the currents in Fig. 16 are reflecting OH adsorption, not O adsorption. This is a major benefit of the XANES analysis; it can distinguish between OH and O on the surface.

The H region from 0.00 – 0.30 V in Fig. 16 appears to reflect the morphology as found from the EXAFS data in this work as well as the effects of cluster size. These CV curves are similar in the H region to those reported by Mukerjee and Srinivasan[4] on the same samples in PEM fuel cells. The PtCo alloy shows a sharp peak around 0.10 V, right where the oxidation of the surface Co from CoH to CoOH occurs as discussed above. The oxidation of the H on the Pt at the surface of the PtCo alloy is also seen. In contrast, the PtCr alloy, which EXAFS analysis indicates has a Pt skin, shows only the oxidation of the adsorbed H, although its intensity is reduced for the Pt/C because of the significantly larger cluster size for the PtCr alloy. The PtFe alloy shows the most dramatic change from that for Pt, with a very intense peak in the H region; i.e., an enhancement rather than a reduction as seen for PtCr. Although it spans the entire H adsorption region, its extremely large intensity may mean it has another source. However, if it reflects H adsorption, the PtFe alloy shows a dramatic reduction in O(H) adsorption and dramatic enhancement of H adsorption, a very strong electronic effect

87

indeed. [Can we get rid of the PtFe data as this may be very distracting from a reviewers perpective and not helpful in an overall context]

The cyclic voltammograms, interpreted in the new light of the detailed information gained from the EXAFS and XANES analysis in this work, appear to be generally consistent with the findings in this work.

Pt enrichment at the surface. - We can only conjecture here on how or why Pt enrichment at the surface might occur to form a Pt skin. Previous studies by Toda *et al*[Error! Bookmark not defined.] directly observed a Pt skin using XPS; others have suggested that a Pt skin exists (Mukerjee[Error! Bookmark not defined.,Error! Bookmark not defined.,4], early papers in Paulus *et al*[22]) based on EXAFS or H chemisorption. In general, these authors conclude that the Pt skin forms by leaching of the more reactive M metals. However, it is unclear whether this forms as a result of the preparation, which sometimes includes an acid wash step when the M atoms may leach out, or if it occurs after electrochemical processing. The latter has been directly confirmed by the XPS results of Toda *et al*[Error! Bookmark not defined.] which showed M atoms at the surface in the as prepared condition, and the absence of M atoms in at least the first 2-3 atom layers below the surface after the electrochemical experiments. However, these samples were prepared by co-sputtering, so the alloys as deposited were perhaps not in the most stable state. Our alloy clusters, prepared by high temperature anneal, might behave very differently and have the Pt surface enrichment already in the as prepared state. Nevertheless, M atom leaching might be thought of as consistent with our finding above, since the Pt-Cr and Pt-Fe alloy clusters had Pt skins (i.e., the reactive Cr and Fe atoms possibly leached out) while the Pt-Co and Pt-Ni alloys (Co and Ni less reactive) were more homogenous.

However, the Pt-M/Pt-Pt coordination ratios found from the EXAFS for the Pt-Cr and Pt-Fe alloys suggest otherwise. A totally homogenous cluster should give a Pt-M/Pt-Pt coordination ratio of 3 in a Pt_3M alloy, as found for Pt-Co and Pt-Ni. The higher Pt-M/Pt-Pt ratio of 0.4-0.5 found in Pt-Cr and Pt-Fe, cannot arise from M leaching out, but only from M atoms moving into the interior of the cluster during the alloying anneal process.

The details of metal segregation in alloys are not completely understood.[61] Most studies to date have been performed on the Pt-Ni and Pt-Co alloys and most agree that the segregation depends on the surface energy and the size of the alloying metal.[62] Theoretical and experimental results[63,64,65] for surface energies indicate that surface segregation should not occur in Pt-Ni (75:25) consistent with our EXAFS results for Pt-Ni. This is consistent with the recent results of Stamenkovic et al,[Error! Bookmark not defined.] which found 75% surface atoms in the as prepared state, and 100% surface Pt atoms after annealing at high temperature for Pt_3Ni clusters. It is also consistent with the recent DFT calculations of Norskov's group[26] which indicate a positive segregation energy of 0.37 and 0.46 eV for Fe and Co, respectively, for M atoms in a Pt host indicating that indeed single Fe and Co atoms prefer to remain in the interior of the alloy at thermodynamic equilibrium. But note the large difference between the segregation energies here for Fe and Co. Perhaps the larger the segregation energy the more the alloy prefers to remain in the homogenous Pt_3M structure (i.e like the Co case), and the smaller segregation energy alloys Pt_nM alloys with lower values of n to form, i.e. Fe enriched in the interior leaving a Pt skin, such as found in this work.

LEED results along with calculated surface concentration profiles done on Pt-Co (75:25) did show that the surface is slightly enriched in Pt on the (111) faces,[66] which although not in agreement with results presented here, however is in the right direction. Perhaps Pt enrichment at the surface begins in PtCo (undetectable in our EXAFS), and then increases still more in the Cr and Fe alloys as we find. However several other studies found no difference between the composition of the Ni and Co alloy clusters.[67,68,22-25] It is clear that much more work must be carried out on the formation or lack of a Pt skin before one can generally predict when this will occur.

Conclusions

X-Ray Absorption studies of Pt/C and Pt-M/C alloys combined with theoretical calculations provide direct spectroscopic evidence for OH inhibition on the electro-catalyst surface in the Pt-M alloys. This OH inhibition going in the direction Pt < Pt-Ni<Pt-Co <Pt-Fe < Pt-Cr is directly correlated with the previously reported kinetic reactivities for a fuel cell with these alloys. The EXAFS analysis shows that the alloys have different morphologies, the Pt-Ni and Pt-Co alloy clusters are more homogenous with M atoms on the surface, while the Pt-Fe and Pt-Cr alloys have a "Pt skin". The alloy composition in these samples determines which inhibition mechanism dominates. The electronic mechanism apparently dominates in the presence of the Pt skin, which is the most effective at inhibiting OH at low coverage, while the lateral interaction plays a more significant role on the O(H) species coming down when the Pt must reside at sites close to the M-OH groups existing at the surface. The mechanism for the Pt skin formation and the regularity for its existence are not clear.

Table 1. Structural Characteristics of the Pt and Pt Alloy electrocatalyst using powder XRD data at 1.54 Å and XANES data.

Electrocatalyst	Lattice parameter	Pt-Pt Bond Distance (Å)	Average Particle Size (Å)	Atomic Ratio (Pt:M) (from in situ XANES)
Pt/C	3.927	2.777	31	76/24
PtMn/C	3.897	2.756	55	69/31
PtCr/C	3.874	2.740	56	73/27
PtFe/C	3.861	2.730	55	72/28
PtCo/C	3.852	2.724	59	74/26
PtNi/C	3.822	2.703	56	71/29

Table 2 Summary of EXAFS first shell results for Pt/C [a]

V (RHE)	N $[\Delta N=0.3^b]$	R(Å) $[\Delta R=0.02^b]$	E_o(eV)
0.00	9.97	2.74	1.64
0.24	9.19	2.73	1.46
0.54	9.04	2.73	1.58
0.84	8.58	2.74	0.817
1.14	6.65	2.73	0.769
Ave.	8.78	2.73	

[a] S_o^2 fixed at 0.934 as calculated by FEFF8 for all data in Tables 2-6

[b] Although the absolute values of ΔN and ΔR are certainly larger than that indicated, the variation in the values of N and R with potential are believed to be meaningful down to the values indicated in Tables 2-6.

Table 3 Summary of EXAFS first shell results for Pt-Co alloy [a]

V		Pt-Pt				Pt-Co		
		N	R(Å)	E_o(eV)		N	R(Å)	E_o(eV)
(RHE)		[ΔN=0.3[b]]	[ΔR=0.02[b]]			[ΔN=0.3[b]]	[ΔR=0.02[b]]	
0.00		7.51	2.71	0.772		1.88	2.67	2.49
0.24		7.42	2.71	2.08		1.96	2.65	-1.42
0.54		7.16	2.71	1.10		1.90	2.66	2.06
0.84		7.01	2.70	0.362		2.28	2.67	2.44
1.14		7.26	2.71	0.431		1.84	2.67	2.24
Ave.		7.27	2.71			1.97	2.67	

Table 4 Summary of EXAFS first shell results for Pt-Ni alloy [a]

V (RHE)	Pt-Pt			Pt-Ni		
	N [$\Delta N=0.3^b$]	R(Å) [$\Delta R=0.02^b$]	E_o(eV)	N [$\Delta N=0.3^b$]	R(Å) [$\Delta R=0.02^b$]	E_o(eV)
0.24	7.60	2.71	0.147	1.89	2.67	1.94
0.54	7.63	2.71	0.639	1.89	2.67	2.40
0.84	7.58	2.71	0.675	1.84	2.67	2.45
Ave.	7.67	2.71		1.89	2.67	2.40

Table 5 Summary of EXAFS first shell results for Pt-Cr alloy [a]

V	Pt-Pt			Pt-Cr		
(RHE)	N $[\Delta N=0.3^b]$	R(Å) $[\Delta R=0.02^b]$	E_o(eV)	N $[\Delta N=0.3^b]$	R(Å) $[\Delta R=0.02^b]$	E_o(eV)
0.00	7.97	2.71	1.87	2.82	2.68	-0.432
0.24	7.83	2.71	0.329	2.91	2.70	2.23
0.54	7.47	2.71	2.10	2.93	2.67	-0.452
0.84	7.54	2.71	1.17	2.72	2.67	-0.948
Ave.	7.70	2.71		2.84	2.68	

Table 6 Summary of EXAFS first shell results for Pt-Fe alloy [a]

	Pt-Pt			Pt-Fe		
V (RHE)	N [$\Delta N=0.3^b$]	R(Å) [$\Delta R=0.02^b$]	E_o(eV)	N [$\Delta N=0.3^b$]	R(Å) [$\Delta R=0.02^b$]	E_o(eV)
0.24	5.54	2.74	3.29	4.48	2.70	4.40
0.54	6.28	2.71	-3.13	4.01	2.72	4.76
0.84	5.31	2.74	-3.40	4.46	2.69	3.84
Ave.	5.71	2.73		4.32	2.70	

χ
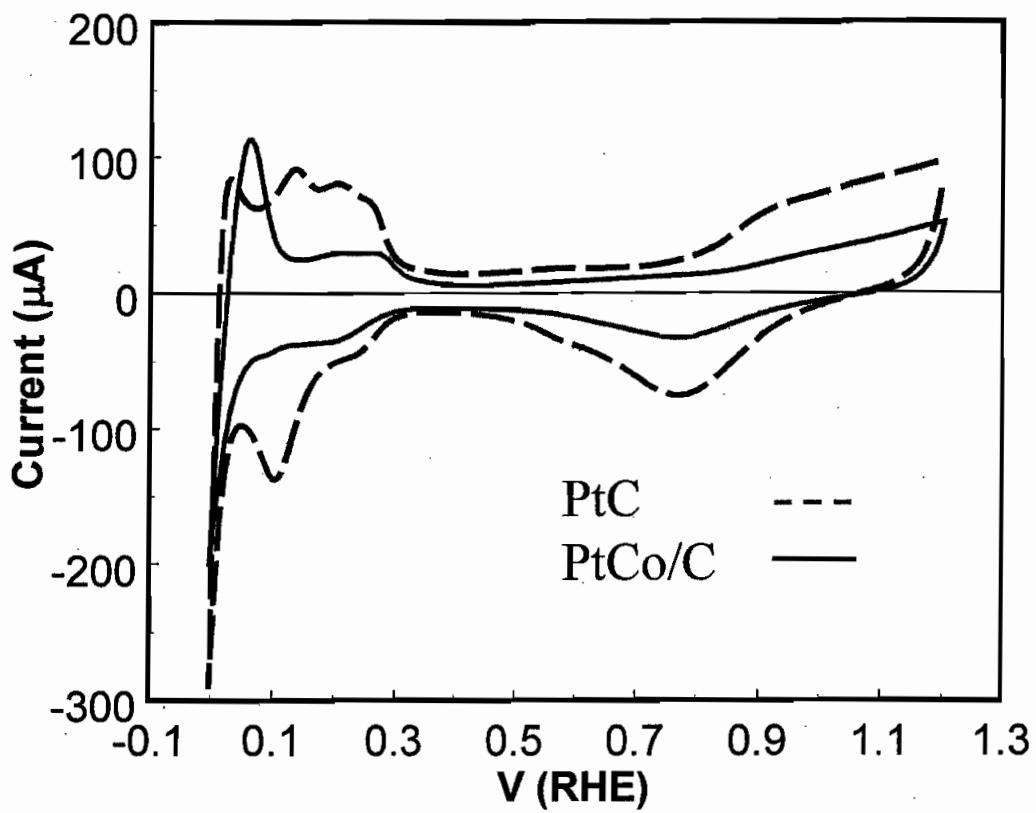
Figure 1 Cyclic voltammogram at scan rate of 50mV/sec comparing Pt/C and Pt-Co/C alloy electrodes in an electrochemical cell.

Clean　　　　**Atop**　　　　**Bridged**

- ⬤ Platinum
- ⬤ Metal
- ⬤ Oxygen
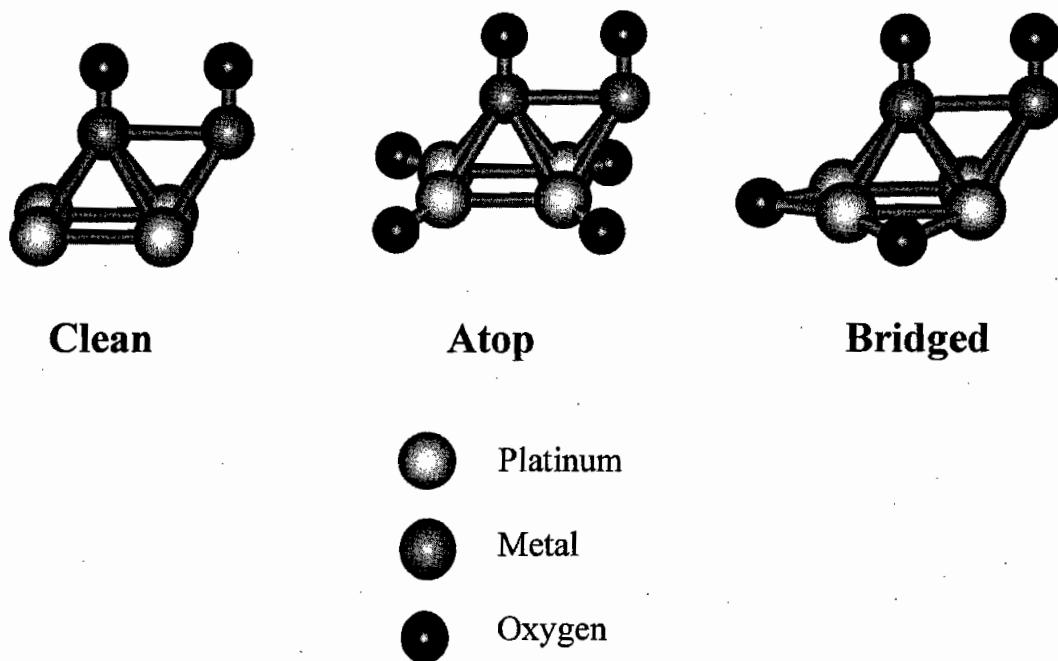
Figure 2 $Pt_4M_2O_2$ cluster models used for FEFF calculations showing the positions of the Pt and M atoms (M=Cr ,Fe, Co, Ni) and oxygen in the atop and bridged positions
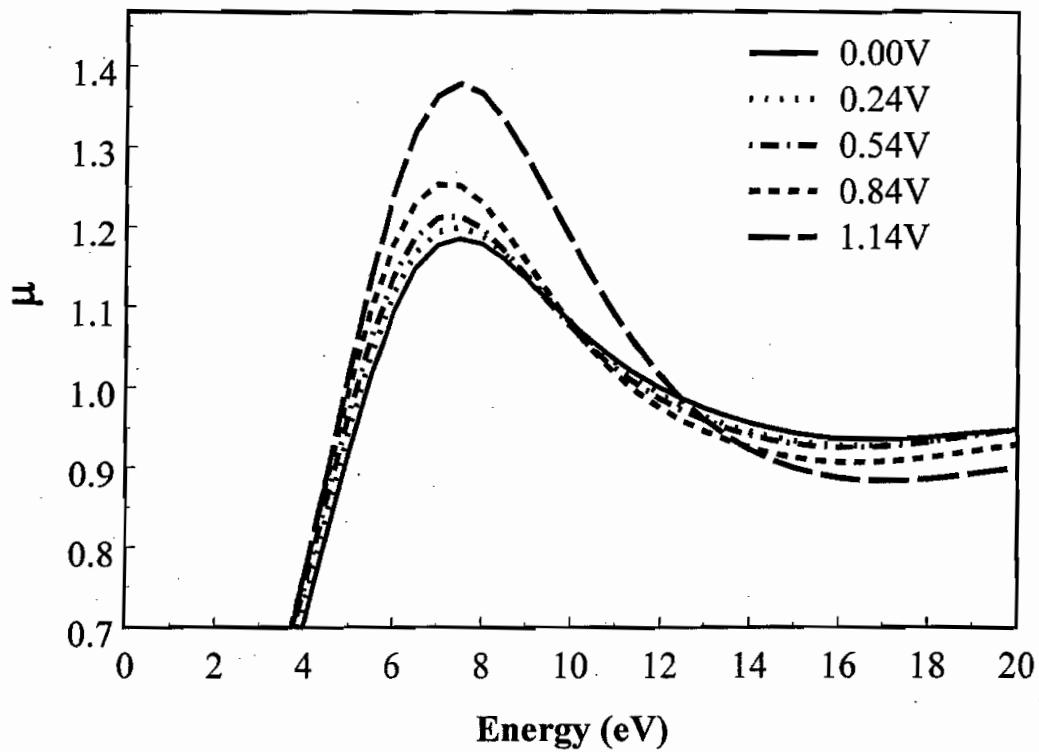
Figure 3 Experimental L$_3$ absorption spectra, μ, for the Pt/C electrode at the indicted

potentials in HClO$_4$.
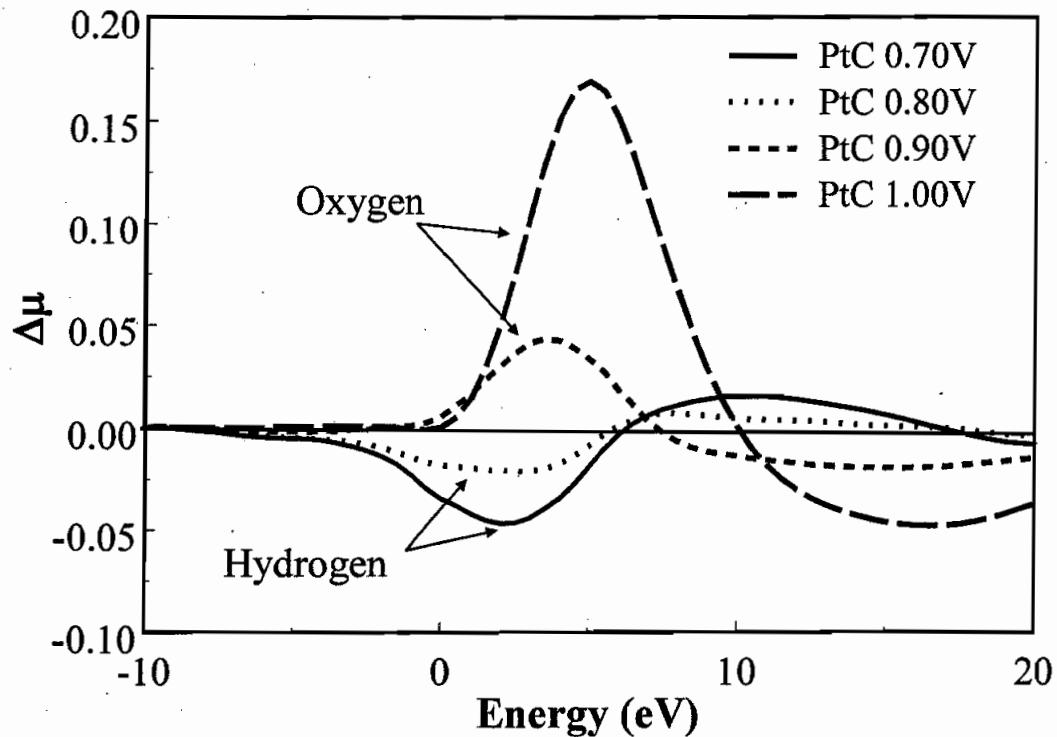
Figure 4 Experimental difference spectra $\Delta\mu = \mu(V) - \mu(0.54\ V)$ obtained from the data in

Figure 3. [The labels for the spectra taken at 0.0 and 0.24 V are not included in the figure, I

think they should be for consistency sake]

99
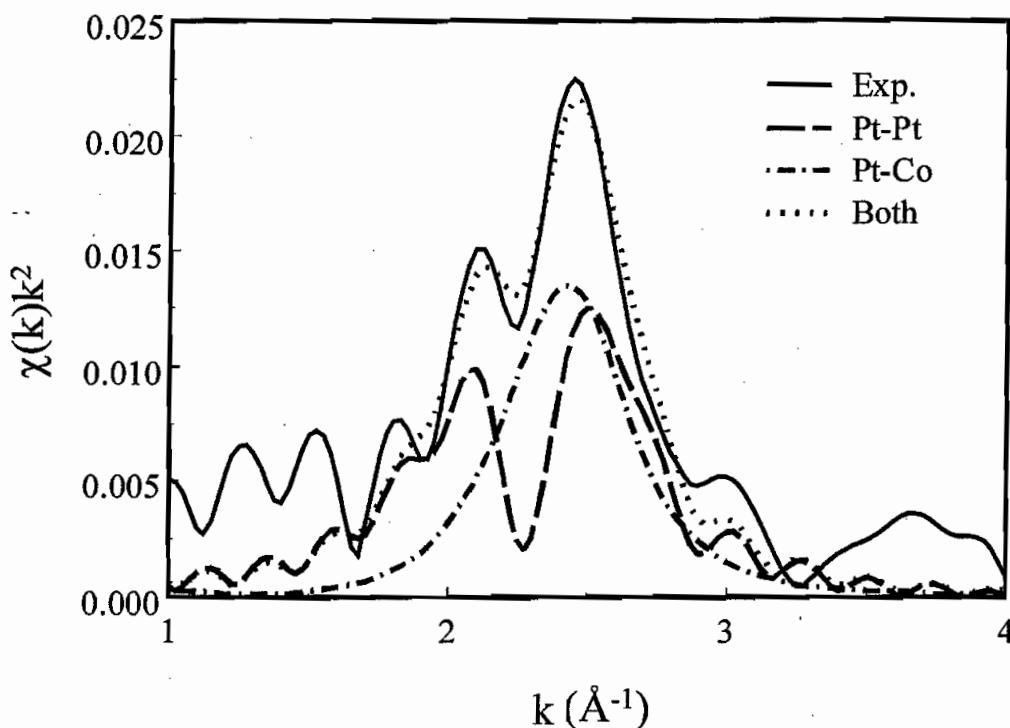
Figure.5 Magnitude of the Fourier Transform (FT) of the experimental EXAFS at the Pt L₃ edge, FT(χ), (k², Δk = 1.5Å⁻¹<k<17Å⁻¹) taken at 0.54 (RHE) for the Pt-Co alloy. The fit (ΔR = 1.34-3 Å) for a two shell analysis (Pt-Pt and Pt-Co) is shown along with the individual Pt-Pt + Pt-Co components using theoretical references obtained from FEFF8 calculations on a Pt₆ cluster (dotted lines).
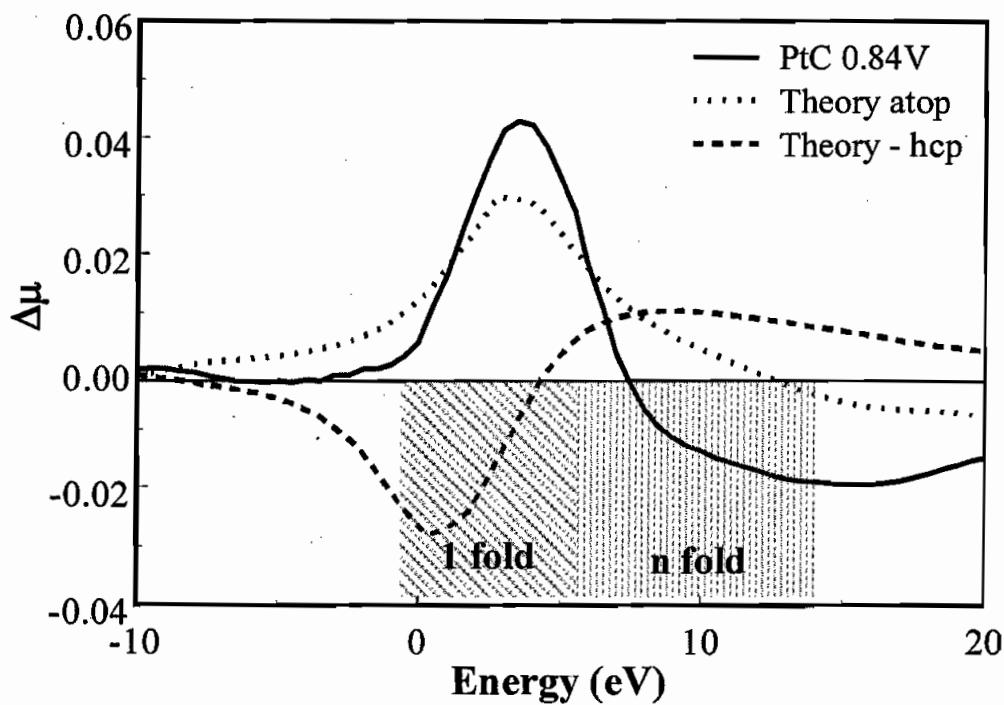
Figure 6 Theoretical signatures obtained from the FEFF8 code for a one-fold oxygen

species, atop and an n-fold, hcp site. The experimental $\Delta\mu$ lineshape obtained from a Pt/C

electrode is also seen at 0.84 V.
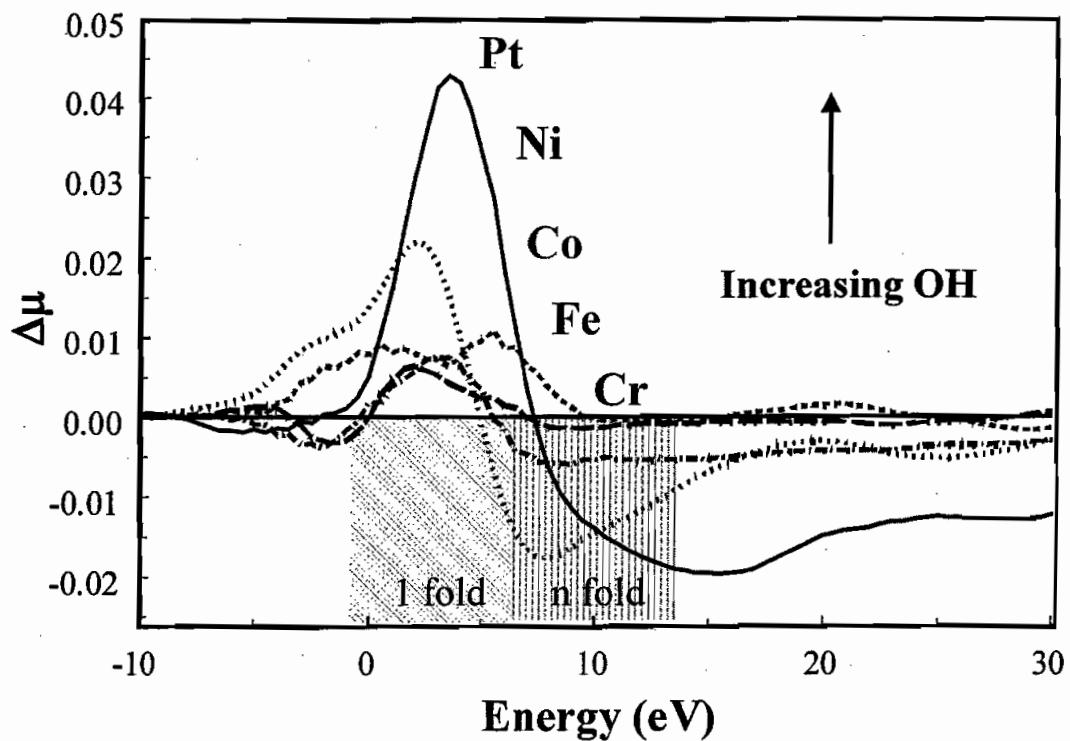
Figure 7 Experimental $\Delta\mu$ for Pt-M/C alloys and Pt/C at 0.84 V in 0.1 M HClO$_4$. The one-fold and n-fold theoretical ranges are indicated. The amount of atop OH on the alloys increases as the alloying metal is changed from Cr to Ni.
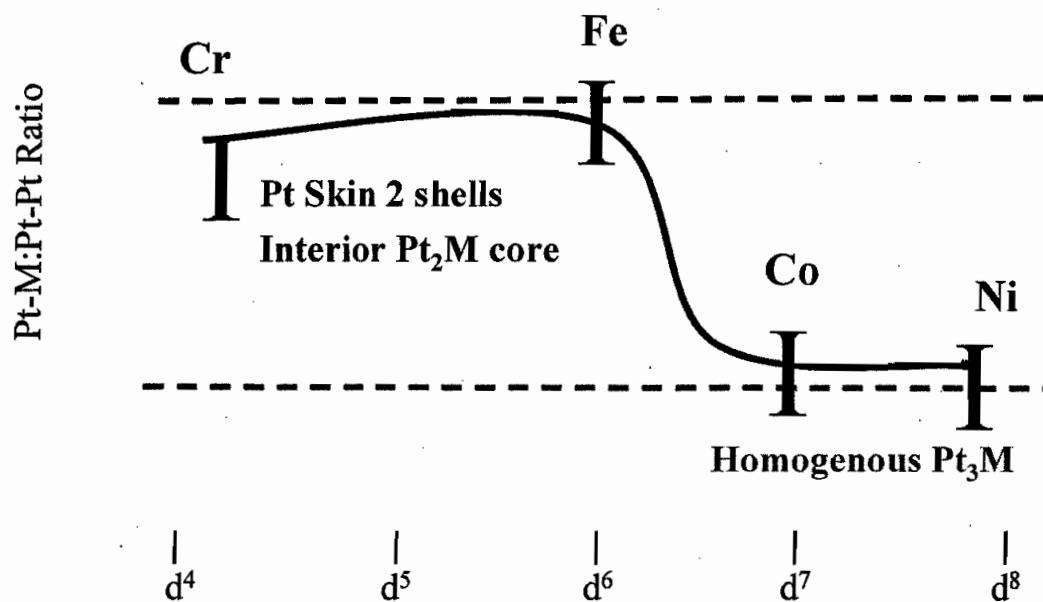
Figure 8 Results obtained from EXAFS analysis of the Pt-M alloys and from theoretical model clusters.

Homogenous

Outer Pt Shell

● Pt   ● M
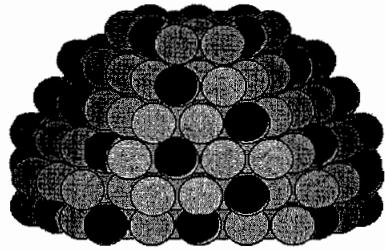
Figure 9 Illustration of the two types of Pt-M alloy clusters indicated. Top: Representative homogenous cluster, Pt_3M cluster with M atoms distributed evenly throughout the cluster. Bottom: A "Pt skin" of two layers of Pt and an inner M distribution of Pt_2M.
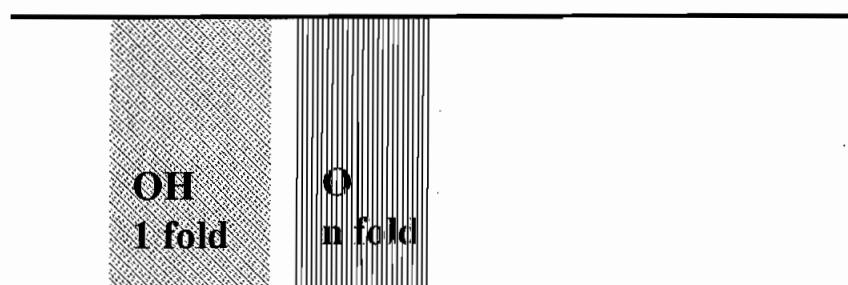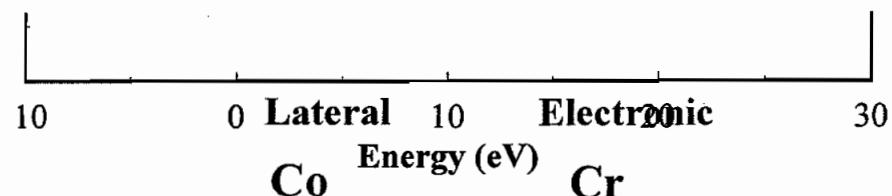
Figure 10 Oxygen adsorption at higher coverage (1.14 V) for the Pt-Co and Pr-Cr alloys. The regions for 1 fold atop and n-fold O are also indicated and were obtained from FEFF8 calculations.
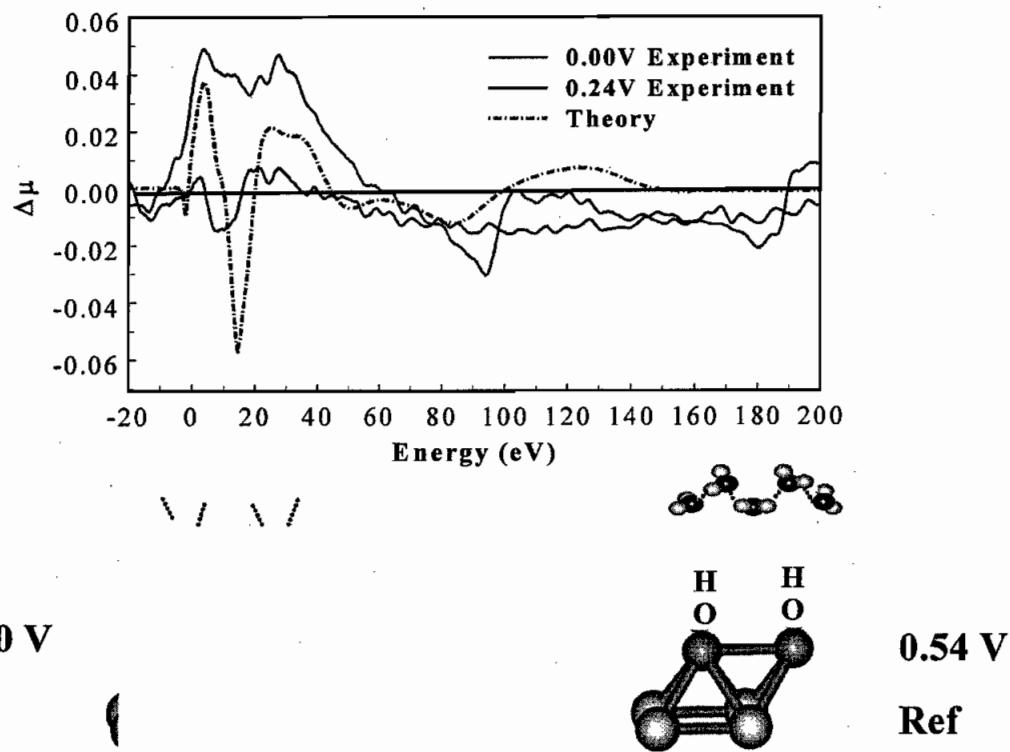
Figure 11 Co K-edge XANES difference spectrum, $\Delta\mu = \mu(V)-\mu(0.54\ V)$, at 0.00 and 0.24V

vs. RHE. A FEFF8 theoretical calculation utilizing the clusters illustrated models H replacing

OH on the Co atoms at 0.00 V. [It is hard to distinguish between data at 0.0 and 0.24 V]

106
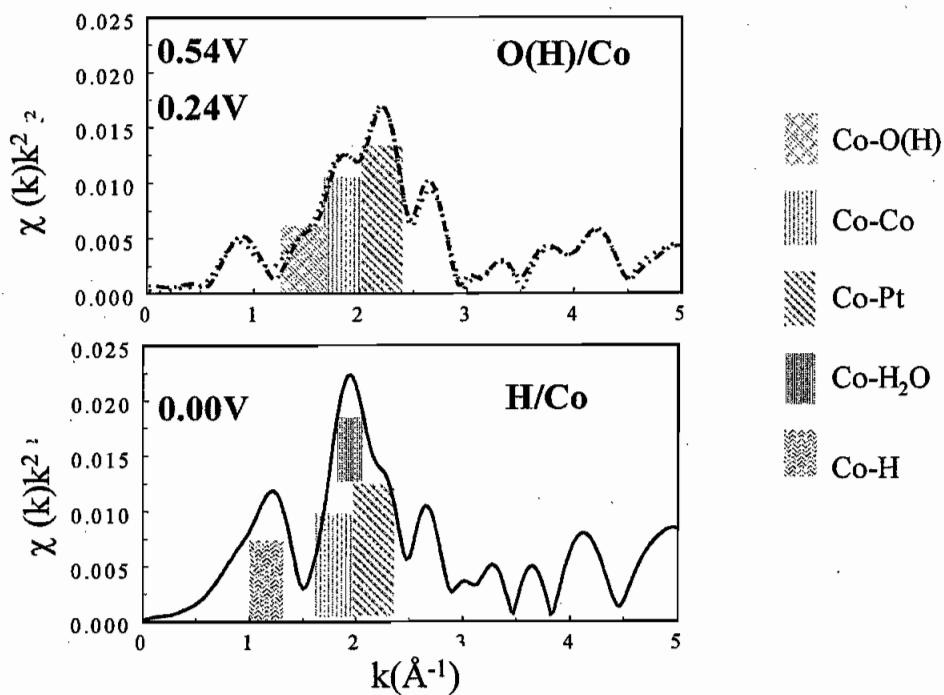
Co K edge EXAFS

Figure 12 Co K edge EXAFS data taken at the indicated potentials. The primary contributions to each feature in the Fourier transform are also indicated.
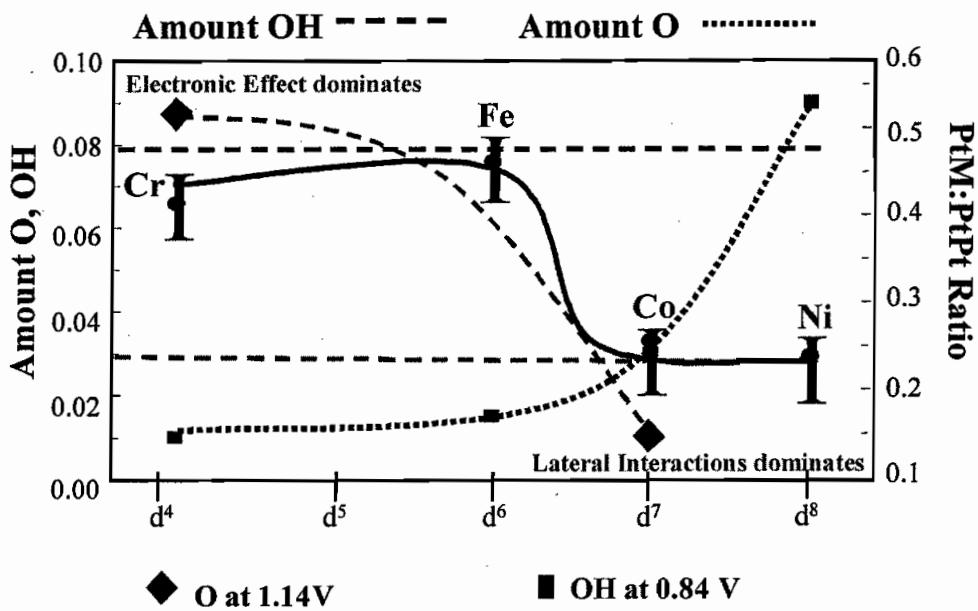
Figure 13 Summary of $\Delta\mu$ amplitudes at 0.84 V (representing atop OH) and the "O peak" in the $\Delta\mu$ spectrum taken at 1.14 V. Also indicated are the $N_{Pt-M}:N_{Pt-Pt}$ ratios from Figure 5.12.
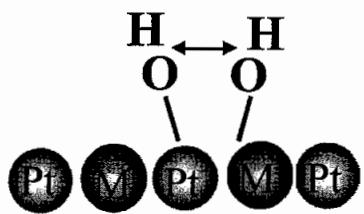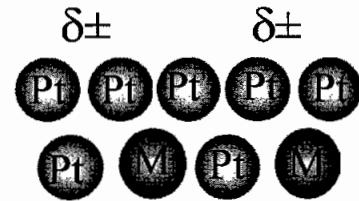
Figure 14 Illustration of the lateral interactions and the electronic effects
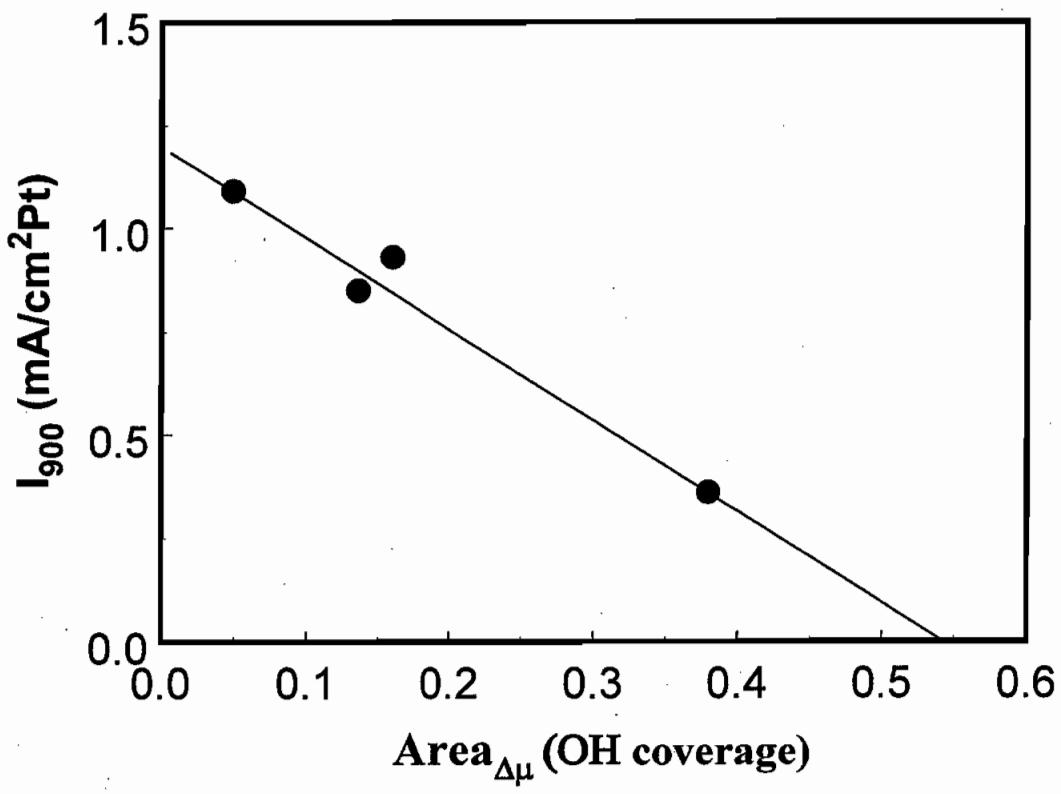
Figure 15 Plot of Area$_{\Delta\mu}$ amplitude reflecting OH adsorption versus the normalized fuel

cell current I$_{900}$ (mA/cm^2 Pt) at 0.90 V.[46]
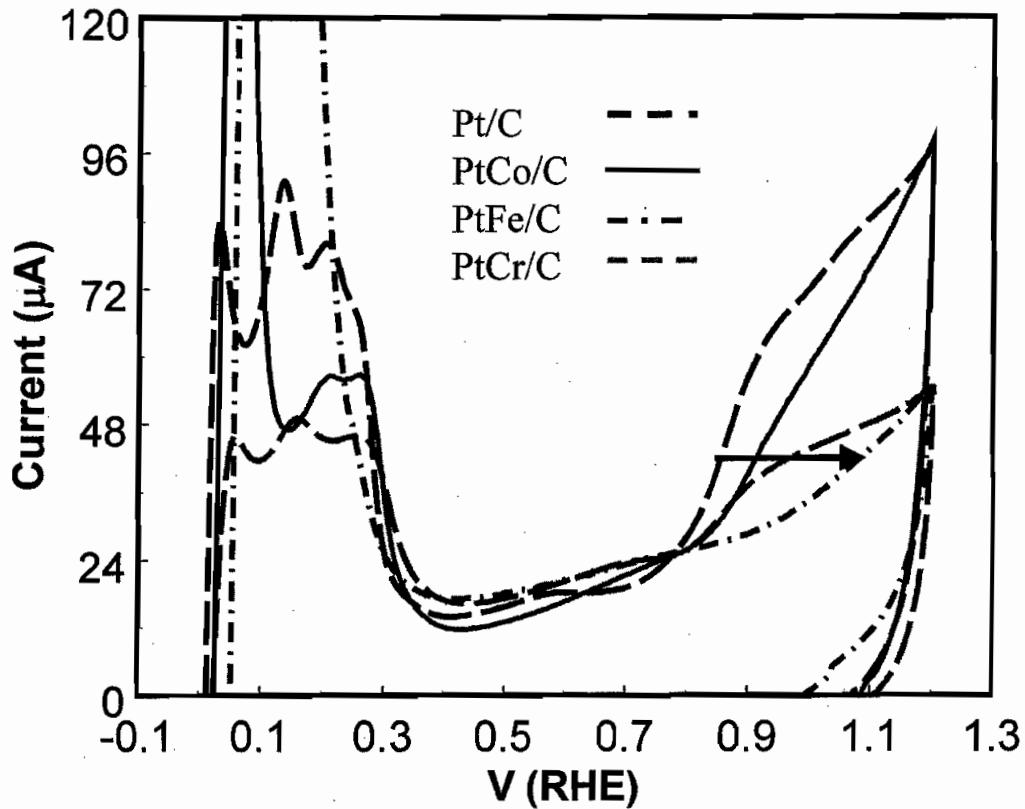
Figure 16 Cyclic voltammograms (scan rate of 50 mV/sec) for the indicated electrodes of Pt/C and the PtM alloys in 1 M TFMSA, where the PtM CV curves have been normalized to have the same nonfaradaic or capacitance currents as that for the Pt/C electrode. The horizontal arrow shows the shift to higher potentials for the onset of OH adsorption. [The colored lines in this figure needs to be changed to b&w]

References

[1] E. Yeager, *Electrochim Acta* **29**, 1527 (1984).

[2] A. Damjanovic, M. Genshaw, J.O'M., Bockris, *J. Electrochem. Soc.* **114**, 466 (1967).

[3] D.B. Sepa, M.V. Vojnovic, L.M. Vracar, A. Damjanovic, *Electrochim. Acta* **32**, 129 (1987).

[4] S. Mukerjee, S. Srinivasan, *J. Electroanal. Chem.*, **357**, 201 (1993).

[5] S. Mukerjee, S. Srinivasan, and M.P. Soriaga, *J. Electrochem. Soc.*, **142**, 1409 (1995).

[6] B.E. Conway, D.M. Novak, *J. Electrochem. Soc.* **128**, 956 (1981).

[7] J.O'M. Bockris, H. Wroblowa, *J. Electroanal. Chem.* **7**, 428 (1964).

[8] P.N. Ross, N.M. Markovic, *J. Electrochem. Soc,* **137**, 3368 (1990).

[9] M.R. Tarasevich, V.S Vilinskaya, *Electrokhimiya* **9**, 96 (1973).

[10] F.A. Uribe, T.E. Springer, M.S. Wilson, T.A. Zawodzinski, S. Gottesfeld, *Proc. Electrochem. Soc.*, **95**, 50 (1996).

[11] A. Michaelides, P. Hu, P., *J. Chem. Phys.* **114**, 513 (2001).

[12] A. Michaelides, P. Hu, P., *J. Am. Chem. Soc.* **123**, 4235 (2001).

[13] K. Karlberg, F.E. Olson, M. Persson, G. Wahnstrom, *J. Chem. Phys.* **1919**, 4685 (2001).

[14] C. Clay, S. Haq, A. Hodgson, *Phys. Rev. Lett.*, **92**, 46102 (2004).

[15] R.D. Gonzalez, *Appl. Surf. Sci.*, **19**, 181 (1984).

[16] J.H. Sinflet, *Acc. Chem. Res.*, **20**, 134 (1987).

[17] A.K. Santara, G.N. Subbanna, C.N.R. Rao, *Surf. Sci.*, **317**, 259 (1994).

[18] T. Rades, C. Pak, M. Polisset-Thfoin, R. Ryoo, J. Fraissard, *Catal. Lett.*, **29**, 91 (1994).

[19] T.J. Schmidt, H.A. Gasteiger, G.D. Stab, P.M. Urban, D.M. Kolb, R.J. Behm, *J. Electrochem. Soc.*, **145**, 2354 (1998).

[20] T. Mizukami, T. Nakamera, P. Stonehart, *J. Electrochem. Soc.*, **141**, 2659 (1994).

[21] V.S. Murthi, C.C. Urian, S. Mukerjee, *J. Phys. Chem. B* **108**, 11011 (2004).

[22] U.A. Paulus, A. Wokaun, G.G. Scherer, T.J. Schmidt, V. Stamenkovic, V. Radmilovic, N.M. Markovic, P.N. Ross, *J. Phys. Chem. B,* **106**, 4181 (2002).

[23] M.D. Obradovic, B.N. Grgur, L.M. Vracar, *J. Electroanal. Chem.,* **548**, 69 (2003).

[24] U. Bardi, B. Beard, P.N. Ross, *J. Catal.*, **22** xxx (1990).

[25] J.M. Bugnard, Y. Gautheir, R. Baudoing-Savois, *Surf. Sci.*, **344**, 42 (1995).

[26] A.V. Ruban, H.L. Skriver, J.K. Norskov, *Phys. Rev. B*, **59**, 15990 (1999).

[27] E. Antolini, *Mat. Chem. and Phys.*, **78**, 563 (2003).

[28] D.E. Ramaker, D.C. Koningsberger, *Phys. Rev. Lett.*, **89**, 139701 (2002).

[29] A.L. Ankudinov, B. Ravel, J.J. Rehr, *Phys. Rev. B.*, **58**, 7565 (1998).

[30] Amsterdam Density Functional Package ADF 2000.02, Department of Theoretical Chemistry, Vrije Universiteit, Amsterdam. http://www.scm.com.

[31] M. Teliska, W.E. O'Grady, D.E. Ramaker, *J. Phys. Chem.*, **108**, 2333 (2004).

[32] M. Teliska, W.E. O'Grady, D.E. Ramaker, *J. Phys. Chem. B.*, in press (2004).

[33] E.A. Ticianelli, C.R. Derouin, S. Srinivasan, *J. Electroanal. Chem.*, **23**, 275 (1998).

[34] S. Srinivisan, E.A. Ticianelli, C.R. Derouin, A.J. Redondo, *Power Sources*, **22**, 359 (1988).

[35] V.M. Jalan, C.L. Bushnell, in U.S., (United Technologies Corp., USA). 4 pp. (1979).

[36] V.M. Jalan, in Eur. Patent Appl., (Giner, Inc., USA). 10pp. (1985).

[37] D.A. Landsman, F.J. Luczak, in Belg. (United Technologies Corp., USA). 16pp. (1981).

[38] P. Stonehart, M. Watanabe, N. Yamamoto, T. Nakamura, N. Hara, K. Tsurumi, in Jpn. Kokai Tokkyo Koho, (Stonehart Associates Inc., USA). 5pp. (1992).

[39] S. Mukerjee, S. Srinivasan, M. Soraiga, J. McBreen, *J. Phys. Chem.*, **99**, 4577 (1995).

[40] J. McBreen, W.E. O'Grady, K.I. Pandya, R.W. Hoffman, D.E. Sawyers, *Langmuir*, **3**, 428 (1987).

[41] WinXAS 97 © copyright Thorsten Ressler 1992-1997.

[42] D.E. Ramaker, B.L. Mojet, D.C. Koningsberger, W.E. O'Grady, *J.Phys. Cond. Matt.*, **10**, 8753 (1998).

[66] G.E. van Dorssen, D.C. Koningsberger, D.E. Ramaker, *J. Phys. Cond. Matt.*, **14**, 13529 (2003).

[44] D.E. Ramaker, B.L. Mojet, J.T. Miller, D.C. Koningsberer, *Top. Catal.*, **10**, 157 (2000).

[45] D.C. Koningsberger, B.L. Mojet, J.T. Miller, D.E. Ramaker, *J. Synch. Rad.*, **6**, 135 (1999).

[46] A.L. Ankudinov, B. Ravel, J.J. Rehr, *Phys. Rev. B.*, **58**, 7565 (1998).

[47] Amsterdam Density Functional Package ADF 2000.02, Department of Theoretical Chemistry, Vrije Universiteit, Amsterdam. http://www.scm.com.

[48] A.D. Becke *J. Chem. Phys.*, **85**, 7184 (1986); J.P. Perdew, *Phys Rev B.*, **33**, 8822 (1986).

[49] B. Ravel, *J. Synchrotron Rad.*, **8**, 314 (2001).

[50] For example, see D.A. McQuarrie and P.A. Rock, *General Chemistry*, p. 290, W.H. Freeman, NY (1987).

[51] J. de Graaf, A.J. van Dillen, K.P. de Jong, D.C. Koningsberger, *J. Catal.*, **203**, 307 (2001); J. de Graaf, Ph.D. Dissertation, Utrecht University, Ridderkerk (2001).

[52] D.C. Koningsberger, J. de Graaf, B.L. Mojet, D.E. Ramaker, J.T. Miller, *Appl. Catal.*, **191**, 205 (2000).

[53] B.L. Mojet, J.T. Miller, D.E. Ramaker, D.C. Koningsberger, *J. of Catal.* **186**, 373 (1999).

[54] D.E. Ramaker, B.L. Mojet, M.T. Garriga Oostenbrink, J.T. Miller, D.C. Koningsberger, *Phys. Chem. Chem. Phys.*, **1**, 2293 (1999).

[55] D.C. Koningsberger, M.K. Oudenhuijzen, J.H. Bitter, D.E. Ramaker, *Topics in Catal.* **10**, 167 (2000).

[56] B.L. Mojet, D.E. Ramaker, J.T. Miller, D.C. Koningsberger, *Catal. Lett.* **62**, 15 (1999).

[57] A.K. Shukla, R.K. Raman, N.A. Choudhury, K.R. Priolkar, P.R. Sarode, S. Emura, R. Kumashiro, *J. Electroanal. Chem.*, **563**, 181 (2004).

[58] Private communication, W.E. O'Grady (2005).

[59] Y. Xu, A.V. Ruban, M. Mavrilkakis, *J. Am. Chem. Soc.*, **126**, 4717 (2004).

[60] A.B. Anderson, E. Grantscharova, S. Seong, *J. Electrochem. Soc.*, **143**, 2075 (1996).

[61] M. Polak, L. Rubinovich, *Surf. Sci. Rep.*, **262**, 1 (1999).

[62] C. Gallis, Thesis Universite Paris VI (1997).

[63] G. Bozzolo, J. Ferrante, R.D. Noebe, B. Good, F.S. Honecy, P. Abel, *Comp. Mater. Sci.* **15**, 169 (1999).

[64] Y. Gauthier, R. Baudoing, M. Lundberg, J. Rundgren, *Phys. Rev. B*, **35**, 7867 (1987).

[65] P. Weignard, B. Jelinek, W. Hofer, P. Varga, *Surf. Sci.*, **301**, 306 (1994).

[66] L.Z. Mezey, W. Hofer, *Surf. Sci.*, **352-354**, 15 (1996).

[67] A.V. Ruban, H.L. Skriver, *Comp. Mater. Sci.*, **15**, 119 (1999).

[68] J.M. Bugnard, Y. Gauthier, R. Baudoin-Savois, *Surf. Sci.*, **344**, 42 (1995).